ALMA MATER STUDIORUM
UNIVERSITÀ DI BOLOGNA

DOTTORATO DI RICERCA IN ASTROFISICA

CICLO 38

Settore Concorsuale: 02/C1 - ASTRONOMIA, ASTROFISICA, FISICA DELLA TERRA E DEI PIANETI

Settore Scientifico Disciplinare: FIS/05 - ASTRONOMIA E ASTROFISICA

Probing the exotic populations in Globular Clusters: the rotational velocity of Blue Stragglers

Presentata da:

Alex Billi

Coordinatore Dottorato

Prof. Andrea Miglio

Supervisore

Prof. Francesco Rosario Ferraro

Co-supervisore

Prof. Barbara Lanzoni

Esame Finale Anno 2026

This thesis is the final publication of a PhD program co-funded by the European Union under the NextGeneration/PNRR initiative.

Founded by the European Union - NextGeneration EU, Mission 4, Component 1, Investment 4.1 (D.M. 351/2022), CUP J33C22001300002.

Finanziato dall'Unione europea NextGenerationEU

Ministero dell'Università e della Ricerca

Italiadomani PIANO NAZIONALE DI RIPRESA E RESILIENZA

ALMA MATER STUDIORUM UNIVERSITÀ DI BOLOGNA

In memoria di Giannino e Luciana

Abstract

Blue Straggler Stars (BSSs) are an "exotic" stellar population observed in Globular Clusters (GCs) and in other stellar environments. BSSs are bluer and brighter than the main sequence turn-off stars, which implies that they are also more massive. Their formation is currently explained by distinct scenarios, e.g. mass transfer activity in binary systems, direct stellar collisions and merging. The fact that their mass is larger than the average ($\sim 1.2\ M_\odot$ against $\sim 0.3\ M_\odot$ in Galactic GCs) makes BSSs fundamental tracers of internal cluster dynamics, but their physical characteristics are still poorly known and, in particular, their rotational properties are largely unconstrained. From a theoretical point of view, high rotational velocities are expected at birth due to angular momentum transfer or conservation, but braking mechanisms should intervene and slow down these stars with timescales and efficiencies that are not fully understood yet. This highlights the need for new observational results able to constrain the BSS formation and evolutionary models. With the aim of investigating the BSS chemical and rotational properties and their possible connection with the host cluster environment, a dedicated spectroscopic survey has been started a few years ago in a sample of Galactic GCs spanning a large range of structural parameters (such as King concentration and central luminosity density).

In this PhD Thesis I analyzed high-resolution spectra of a sample of 114 BSSs belonging to three low- to intermediate-concentration GCs included in the survey (namely, NGC 3201, M55, and NGC 1851) with the aim to characterize their rotational properties. These data complemented earlier results obtained in other systems, extending the investigation to the smallest concentrations and densities (thanks to the study of NGC 3201 and M55) and bridging the previous gap between low- and high-concentration systems (thanks to the analysis of NGC 1851). The BSS rotational measurements collected to date revealed the presence of specific trends between the fraction of fast rotating (FR) BSSs (i.e., stars with *v sin(i)* ≥ 40 km s^{-1}) and some structural parameters of the host clusters. In particular, low-concentrated and low-density systems exhibit a higher fraction of FR-BSSs, reaching $\sim 50\%$ in M55, and showing *v sin(i)* as large as 220 km s^{-1} in some cases, whereas high-concentrated and high-density clusters host significantly smaller percentages of these stars (below $\sim 10\%$), with only a few BSSs rotating faster than 40 km s^{-1}.

The percentage of FR-BSSs has also been found to correlate with the fraction of binary systems and to anti-correlate with the collisional parameter. The pieces of evidence collected so far suggest a scenario where recent BSS formation is occurring in low-density environments, likely due to the evolution of primordial binary systems, while it is significantly suppressed

in high-density clusters maybe because of a destructive action of stellar collisions on binaries, or a higher efficiency of the intervening braking mechanisms. The results presented in this PhD Thesis can be considered as the starting point for future observational campaigns in other stellar environments and larger samples of stellar clusters, and they call for renewed theoretical effort to produce models able to accurately describe the physical properties of these "exotic" stars and the role that the host environment plays in setting them.

Contents

List of Abbreviations

AGB	Asymptotic Giant Branch
BSS	Blue Straggler Star
CC	Core Collapse
CMD	Color-Magnitude Diagram
COL	Collisional
DR	Data Release
ESO	European Southern Observatory
FR	Fast Rotating
GC	Globular Cluster
GGC	Galactic Globular Cluster
HB	Horizontal Branch
HR	High Resolution
HST	Hubble Space Telescope
KS	Kolmogorov-Smirnov
M2FS	Michigan/Magellan Fiber System
MS	Main Sequence
MT	Mass Transfer
MW	Milky Way
OC	Open Cluster
PCC	Post Core Collapse
RGB	Red Giant Branch
SED	Spectral Energy Distribution
SGB	Sub-Giant Branch
SNR	Signal-to-Noise Ratio
TO	Turn-Off
UT	Unit Telescope
UV	Ultraviolet
VLT	Very Large Telescope
WFC3	Wide Field Camera 3
W UMa	W Ursae Majoris

CHAPTER 1

Introduction

1.1 Globular clusters

Globular clusters (GCs) are stellar systems of $\sim 10^5$-10^6 gravitationally bound stars in a nearly spherical configuration. The Milky Way (MW) contains approximately 150 GCs (Harris, 1996; Baumgardt & Hilker, 2018) distributed among the halo, the bulge and the thick disk, which are referred to as Galactic GCs (GGCs). Due to their high number of stars, these systems are very bright, with absolute magnitudes $M_V < -7.0$ (Harris, 1996). They are also the densest stellar systems present in galaxies, with luminosity densities up to $10^6\ L_\odot\ pc^{-3}$ (Harris, 1996). GGCs are considered among the oldest stellar systems of our Galaxy, with ages ranging from 10 to 13 Gyrs (Gratton et al., 1997; Chaboyer et al., 1998; Marín-Franch et al., 2009). This implies that the stars populating these systems are low-mass stars. The typical Turn-Off (TO) mass is about 0.8 $M_\odot$. In other galaxies, such as the two Magellanic Clouds, the age distribution is broader, with stellar ages ranging from a few million years up to 13 Gyrs (Mackey & Gilmore, 2003). From a chemical point of view, GGCs are metal-poor stellar systems, with mean metallicity of [Fe/H][1] < -1.0. Halo GGCs tend to exhibit the lowest metallicities, with [Fe/H] values ranging from -2.5 to -0.5 dex (Harris, 1996), whereas bulge GCs are generally more metal-rich, with [Fe/H] ~ -0.5 dex (Massari et al., 2014; Crociati et al., 2023; Ferraro et al., 2025).

For decades, GCs have been generally considered the result of a single burst of star formation.

[1]Note that the iron abundance is generally used as an indicator of a stellar system metallicity. In particular this definition compares the metallicity of a system to that of the Sun.

$$[Fe/H] = log\left(\frac{Fe}{H}\right)_* - log\left(\frac{Fe}{H}\right)_\odot \tag{1.1}$$

Their gravitational potential is not deep enough to retain high-velocity gas ejected by supernova explosions. Consequently, no gas remains to fuel additional bursts of star formation, and the stars present in GCs are therefore coeval and homogeneous in iron. In particular, GCs have been thought to be the closest example in nature of the concept of simple stellar population, i.e., a stellar system made of coeval stars, also homogeneous in chemical composition. Over the past decades, however, numerous spectroscopic studies have investigated the chemical composition of GC stars, revealing the presence of multiple populations showing variations in light elements abundances, such as He, C, N, O, Na, Mg, Al, and K (Kraft, 1994; Gratton et al., 2004; Carretta et al., 2009a,b; Gratton et al., 2012; Mészáros et al., 2015).
The most widely accepted scenario suggests the existence of a first generation of stars with a field-like chemical composition, and a second generation formed from material processed by massive first-generation stars, with enhanced abundances of some light elements (e.g. N, Na, Al) and depleted abundances of others (e.g. C, O, Mg). Although the nature of multiple populations is primarily determined by chemical abundance differences, photometric studies in specific filters sensitive to C, N, and O abundance variations boosted the detection of multiple populations in GCs (see, e.g., Lardo et al., 2011; Monelli et al., 2013; Piotto et al., 2015). Most of the results have been obtained thanks to Hubble Space Telescope (HST) ultraviolet (UV) data, and recent James Webb Space Telescope observations are now extending the investigation to the faintest end of the main sequence. These studies revealed the presence of multiple sequences in the color-magnitude diagram (CMD) along all evolutionary stages, including the Main Sequence (MS; Piotto et al., 2007; Milone et al., 2019, 2023; Cadelano et al., 2024), Sub-Giant Branch (SGB; Piotto, 2009; Lardo et al., 2012; Piotto et al., 2012; Milone et al., 2018), Red Giant Branch (RGB; Yong et al., 2008; Milone et al., 2015, 2017), Horizontal Branch (HB; Piotto et al., 2007; Marino et al., 2011, 2014) and Asymptotic Giant Branch (AGB; Monelli et al., 2013; Milone et al., 2015; Nardiello et al., 2015).

1.1.1 Structure of GCs

GCs are the densest environments present in our galaxy. Due to the high stellar density, collisions between stars become significant, at odds with essentially any other environment, where they are totally negligible. The comparison between the two-body relaxation time and the system age determines the importance of collisions in a stellar system. The two-body relaxation time, i.e., the timescale needed for a system to reach relaxation by two-body encounters, can be estimated as follows:

$$t_{2b} \simeq \frac{0.1N}{lnN} t_{cross} \tag{1.2}$$

Taking as typical values $N \sim 10^5 - 10^6$ and $t_{cross} \sim 1\ Myr$, the two-body relaxation time in GCs is typically of 1 Gyr, that is definitely much smaller than GC ages. Therefore, GCs are considered collisional systems. This confirms that stellar encounters play a crucial role in such dense environments, making them powerful laboratories for studying stellar dynamics. Because of their collisionality, physical quantities of GCs such as the stellar density, surface brightness and velocity dispersion profiles, should be described by a Maxwellian distribution with a tidal truncation due to the influence of the host galaxy. In fact, GCs are well described by the so-called King models (King, 1966) that, in spherical symmetry and under the assumption of orbital isotropy, are characterized by the following distribution function:

$$f(E) = \begin{cases} C\left(e^{-\frac{E}{\sigma^2}} - 1\right) & \text{if E} < 0 \\ 0 \quad \text{if E} \geq 0 \end{cases} \tag{1.3}$$

where C is a constant related to the density, σ is the dispersion velocity, and E is the total energy defined as $E = v^2/2 + \Psi(r)$. In turn, $\Psi(r)$ is the gravitational potential defined in a way that $\Psi(r_t) = 0$, with r_t being the truncation radius. The projected density or surface brightness distribution shows a flat profile in the central regions of the cluster, followed by a monotonic decrease at larger radii. King models can be parametrized by a single parameter, that is the concentration c defined as:

$$c = log\left(\frac{r_t}{r_0}\right) \tag{1.4}$$

where r_0 is the King radius defined as follows:

$$r_0 = \sqrt{\frac{9\sigma^2}{4\pi G\rho_0}} \tag{1.5}$$

Here G is the gravitational constant and ρ_0 is the central density. In the original formulation of King models (King, 1966), r_0 is indeed the core radius r_c that is the distance from the cluster center at which the cluster surface stellar density drops to half of its central value. These two scale distances are almost coincident in models with large concentration parameter c, while r_c becomes $\sim 20\%$ smaller than r_0 for the least concentrated models. Figure 1.1 shows the surface brightness profile of King models for different values of concentration parameter: as c increases, the radial decline of the profile becomes smoother.

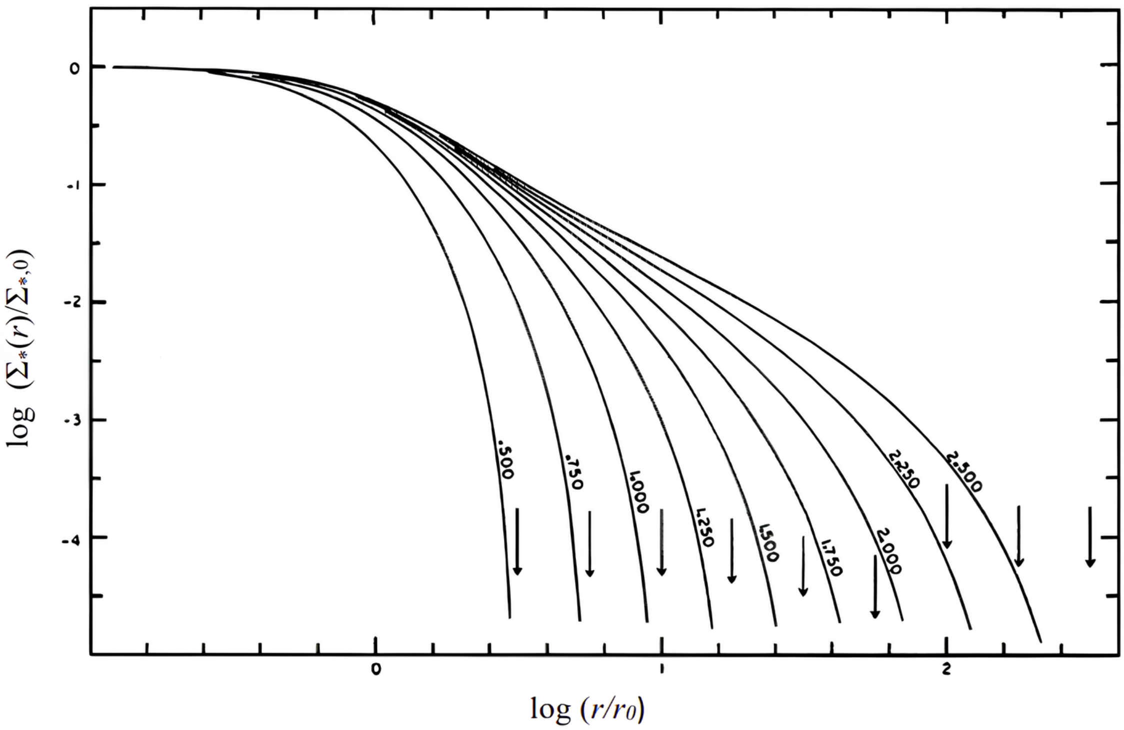

FIGURE 1.1: Surface brightness profiles of the King model family for different values of the concentration parameter c (see the labels marking the plotted curves). The x-axis shows the logarithm of the distance from the center normalized by the King radius. The y-axis shows the logarithm of the surface brightness normalized to its central value. The arrows mark the position of the tidal radius r_t for each value of c. Figure taken from King (1966).

1.1.2 Internal dynamics

Dynamical friction is a physical process that affects the most massive stars in a cluster, making them decelerate and migrate towards the central regions of the system. The dynamical friction timescale depends on the distance from the cluster center (r) through the cluster velocity dispersion and density, as well as on the mass of the "test-particle" star, according to the following relation:

$$t_{DF}(r) \propto \frac{\sigma^3(r)}{M\ \rho(r)} \tag{1.6}$$

Clearly, the dynamical friction timescale is inversely proportional to the stellar mass: the larger the stellar mass, the shorter the timescale. It is also inversely proportional to the density of the system, implying that dynamical friction is much more effective in the cluster central regions than in the outskirts. While the density varies by several (up to six) orders of magnitude between the center and the outskirts of a GC, the velocity dispersion decreases by at most a factor of ten. Hence, the dependence on the cluster density is much more important than that on the velocity dispersion.

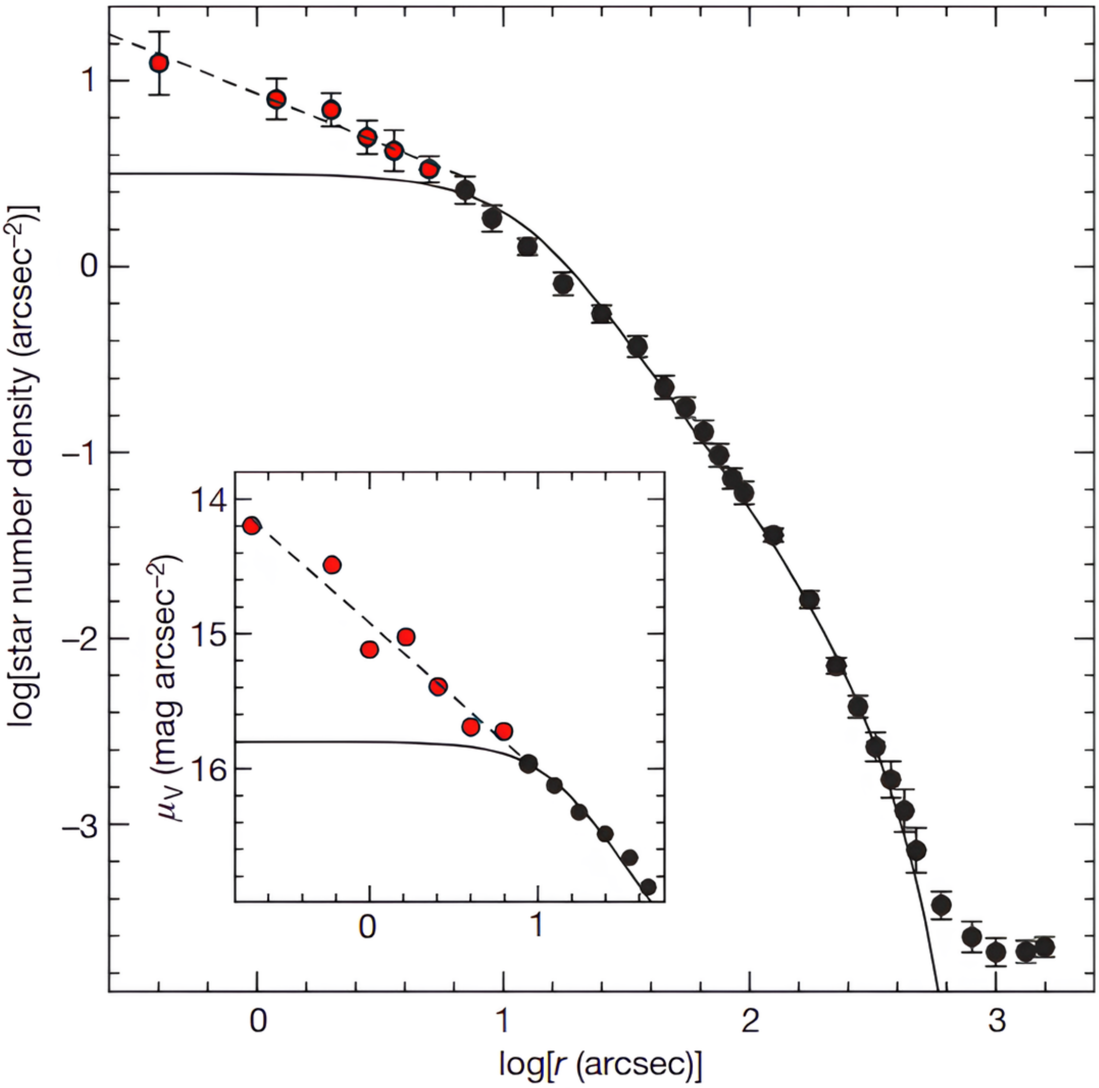

FIGURE 1.2: Number density profile (main panel) and surface brightness profile (inset) of the PCC globular cluster M30. In both panels, the black circles represent the observed distribution at $r > 5''$, which is well reproduced by the King model shown as a solid line. The red circles mark the values observed in the innermost region ($r < 5''$), which significantly deviate from a King model behavior and are well fitted by a power law with slope ~ -0.5 (dashed line). Figure taken from Ferraro et al. (2009).

Dynamical friction generates the so-called "mass segregation" phenomenon, meaning that, as time passes, the most massive stars sink toward the central regions faster than lower mass objects. In turn, the migration of massive stars toward the central regions causes a loss of kinetic energy from the core. Therefore, the core heats up and shrinks. The hotter the core becomes, the more kinetic energy is subtracted. Consequently, the core keeps contracting, sustaining and reinforcing the process. This is a runaway effect that ultimately leads to "core collapse"

(CC; Hénon, 1961; Spitzer, 1987; Meylan & Heggie, 1997). This is thought to be halted by hard binaries, that act as an energy source. GCs that experienced core collapse are called post core collapse (PCC) GCs. These systems can be identified photometrically by studying their density or surface brightness profiles. Indeed, the central portion of the density profile in a PCC cluster is not flat but follows a power law distribution (see an example in Figure 1.2). Therefore a way to identify these systems is by examining their distribution profiles. Given that PCC clusters exhibit a power-law density cusp rather than the flat isothermal core required by King models, and that in these systems the physical assumptions of thermal equilibrium underlying King models do not apply, most catalogs arbitrarily assume a concentration parameter of $c = 2.5$ for all PCC clusters (Harris, 1996; Baumgardt et al., 2003). This is because the best (although poor) description of the observed density profiles in these cases is obtained for values of $c > 2$. This aspect is further discussed in Chapter 6. In the MW, it is estimated that 15–20% of GCs are CC or PCC systems (Djorgovski & King, 1984; Lugger et al., 1995).

1.2 Blue Straggler Stars

1.2.1 Introduction and general properties

Blue Straggler Stars (BSSs) have been observed for the first time in the GGC M3 (Sandage, 1953). Their name was coined by Burbidge & Sandage (1958) in a study of the GC NGC 7789. In the following decades, thanks to the advent of more powerful telescopes and instruments, extensive studies of BSSs in GCs were carried out (Ferraro et al., 1997, 1999, 2003, 2006a; Piotto et al., 2004; Lanzoni et al., 2007b; Leigh et al., 2007; Dalessandro et al., 2008; Moretti et al., 2008). It has also been discovered that other stellar environments can host BSSs, such as open clusters (OCs) (Carraro et al., 2008; Mathieu & Geller, 2009; Geller & Mathieu, 2011; Gosnell et al., 2014; Rain et al., 2020, 2021a), halo and bulge (Preston & Sneden, 2000; Clarkson et al., 2011) and dwarf spheroidal galaxies (Momany et al., 2007; Mapelli et al., 2009). Concerning GCs, Piotto et al. (2004) identified 3000 BSSs in 56 GGCs. They found that the BSS frequency, relative to the number of the HB stars, correlates with the integrated absolute magnitude M_V and with the central density, although the latter is less significant. Regarding OCs, Rain et al. (2021b) identified 897 BSSs in 111 clusters out of a total of 408 OCs. They found an absence of BSSs in young OCs and a steep increase in the number of these stars in clusters with $t_{age} > 500\ Myr$.

BSSs are an "exotic" population of core hydrogen-burning stars that, in the CMD, lie in a sequence brighter and bluer than the MS-TO. Since the magnitude traces the luminosity of

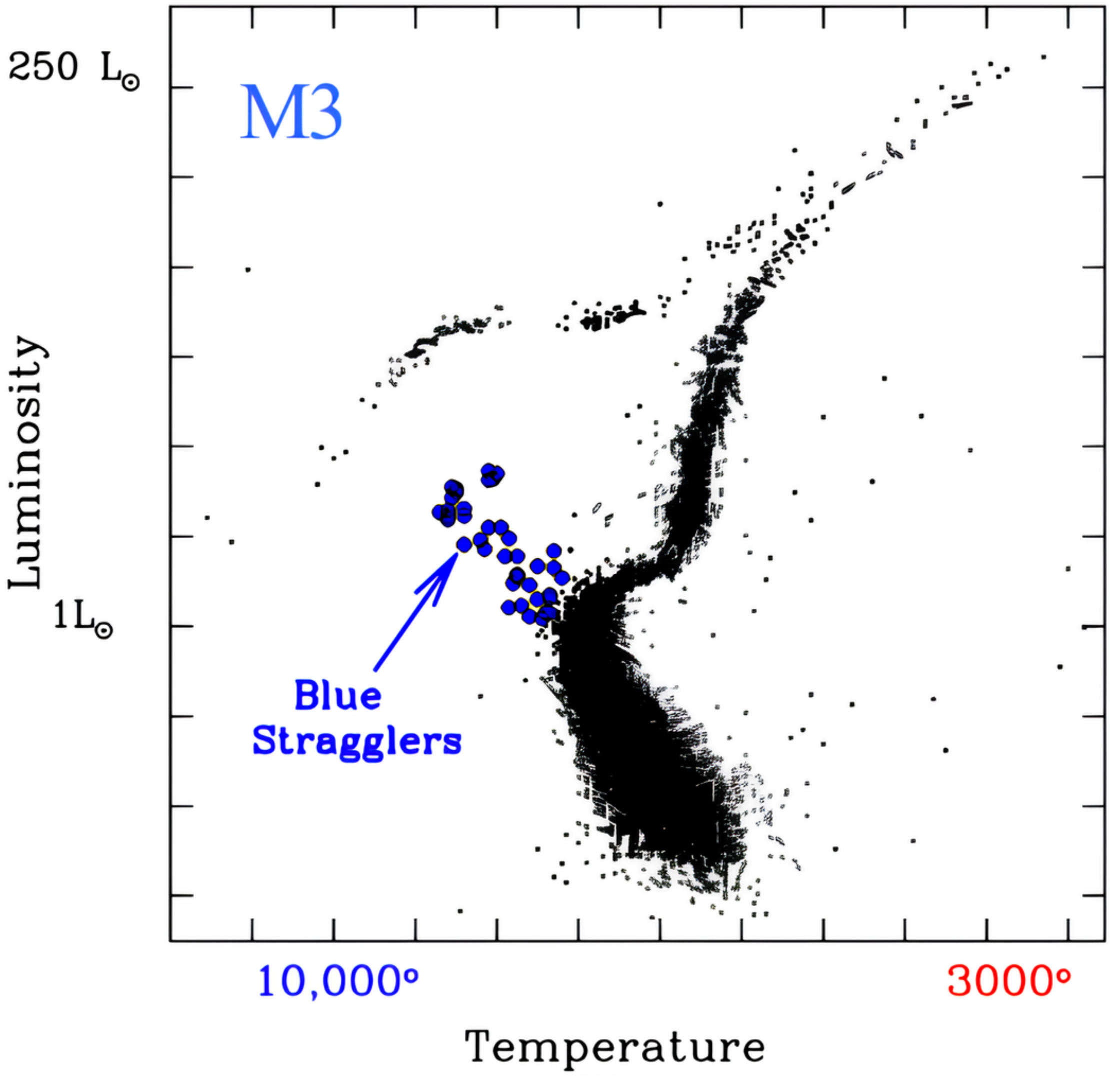

FIGURE 1.3: Illustration of the position of BSSs (blue dots) in a Temperature-Luminosity diagram of the GC M3. Luminosity and temperature are expressed in unit of solar luminosity and Kelvin, respectively. Figure taken from Ferraro et al. (2020).

a star and the color traces its temperature, BSSs are both more luminous and hotter than MS-TO stars (see Figure 1.3). Hence, BSSs appear to be a younger population made of more massive stars compared to all the other stars of the cluster.

1.2.2 Mass determination

The accurate determination of stellar masses remains a challenging task. The estimation of BSS masses has been performed using different methods. Shara et al. (1997) directly measured the mass of a BSS in the GGC 47 Tucanae through spectroscopic observations. Firstly, they derived the stellar parameters, such as effective temperature (T_{eff}) and surface gravity (g). Subsequently, they calculated the stellar radius using the following relation:

$$\left(\frac{R}{d}\right)^2 = \frac{1}{4\pi}\frac{f_\lambda}{H_\lambda} \tag{1.7}$$

where f_λ and H_λ are the observed and the theoretical stellar fluxes, respectively, R is the stellar radius, and d is the distance of the cluster from the Earth. Finally, combining the stellar parameters and the radius, they obtained the stellar mass M_* as:

$$M_* = \frac{gR^2}{G} \tag{1.8}$$

where G is the gravitational constant. With this method the authors estimated a mass of $1.7\ M_\odot$, which is, as expected, significantly higher than that of MS-TO stars.
Another way to estimate the mass is through the analysis of the pulsation frequency of BSSs classified as variable SX Phoenicis stars. Fiorentino et al. (2014) obtained the mass of some BSSs in the cluster NGC 6541 using the pulsation equations P(M, L, T_{eff}) derived from the linear and non adiabatic pulsation models. In this case they obtained a mass of $1.0 - 1.1\ M_\odot$ which is, as in the previous case, larger than the masses of MS-TO stars ($\sim$ 0.75 $M_\odot$).
Additionally, BSS masses can be inferred also by comparing their position in the CMD with evolutionary tracks. For example, Geller & Mathieu (2012), analyzing BSSs in the OC NGC 188, derived mass values of $1.2 - 1.6\ M_\odot$, confirming their larger values than those of MS-TO stars ($\sim 1.0\ M_\odot$).
Moreover, Raso et al. (2019) calculated the masses of 22 BSSs in the GC 47 Tucanae through Spectral Energy Distribution (SED) fitting. Comparing the SED-fit based mass measurements with the mass estimates derived from the CMD position, they found consistent results, confirming that both methods can be used to obtain at least first-estimates of BSS masses.

1.2.3 Formation scenarios

The evidence that BSSs look younger than the other cluster stars is inconsistent with the fact that, as mentioned in Section 1.1, no recent star formation has occurred in GCs. This implies that their larger masses are not due to younger ages, but must be explained by some mass enhancement processes involving the other cluster stars. The formation and evolutionary processes of BSSs are still not completely understood although much progress in the observational characterization and theoretical modeling of these stars has been made in recent years, especially in OCs (see, e.g., Mathieu & Geller, 2009; Perets & Fabrycky, 2009; Chatterjee et al., 2013; Leiner & Geller, 2021; Jiang, 2022; Reinoso et al., 2022; Cordoni et al., 2023 and references therein). Three main formation scenarios have been suggested so far: (i) mass-transfer (MT) activity in binary systems (McCrea, 1964), where a companion star transfers mass and angular momentum to the accreting proto-BSS, (ii) direct collisions (COL) between two or more stars (Hills & Day, 1976; Sills et al., 2005), and (iii) mergers/collisions induced by dynamical/stellar evolution in triple systems (see Andronov et al., 2006; Perets & Fabrycky, 2009).

The MT channel involves two stars in a binary system, called primary and secondary, respectively. When the primary star fills its Roche lobe, the transfer of mass and angular momentum from the primary to the secondary begins, leading to the formation of the future BSS. As a consequence, the primary star loses its outer layers and becomes a white dwarf. This formation channel is dominant in low-density environments, because binary systems are more likely to survive. This is confirmed by photometric observations. In this respect, Sollima et al. (2008), see Figure 1.4, found a clear correlation between the BSS specific frequency and the binary fraction in the core of thirteen low-density GGCs. Different studies have also been carried out in OCs. Mathieu & Geller (2009) and Geller et al. (2015), studying the OCs NGC 188 and M67 (where densities are much lower than in GCs), found high binary fractions of 76 ± 19% and 79 ± 24%, respectively. Moreover, Carney et al. (2001), from observations of metal-poor field BSSs, found a binary fraction of 47 ± 10%. All these findings are consistent with BSSs formed through the MT formation mechanism.

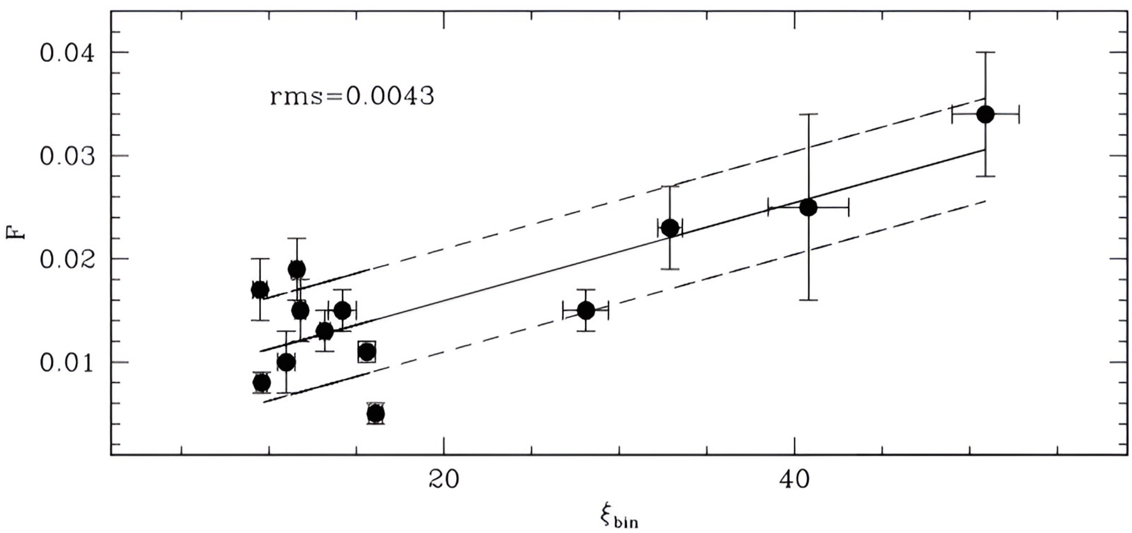

FIGURE 1.4: BSS specific frequency as a function of the core binary fraction in thirteen low-density GGCs. Figure taken from Sollima et al. (2008).

In the COL scenario, BSSs form through collisions between two or more stars. COL-BSSs are

more likely to form in high-density systems, where densities are higher and collisions occur more frequently.
Finally, in the third scenario, BSS form through mergers induced by dynamical and stellar evolution in triple systems. In this scenario, stars are generally arranged in a hierarchical configuration. Two of these stars are bound together in an inner binary system. This forms an outer binary system with the third, more distant star. This farther star can induce the merger of the inner binary system through the so-called Kozai-Lidov mechanism (Kozai, 1962; Lidov, 1962; Perets & Fabrycky, 2009).

1.2.4 Distinguishing the formation mechanisms

Photometric and spectroscopic observations can provide key constraints about BSS formation mechanisms. Over the past few decades, several studies have investigated features that can help distinguishing between these formation channels. Indeed, a few promising features have been identified.

1.2.4.1 Chemical composition

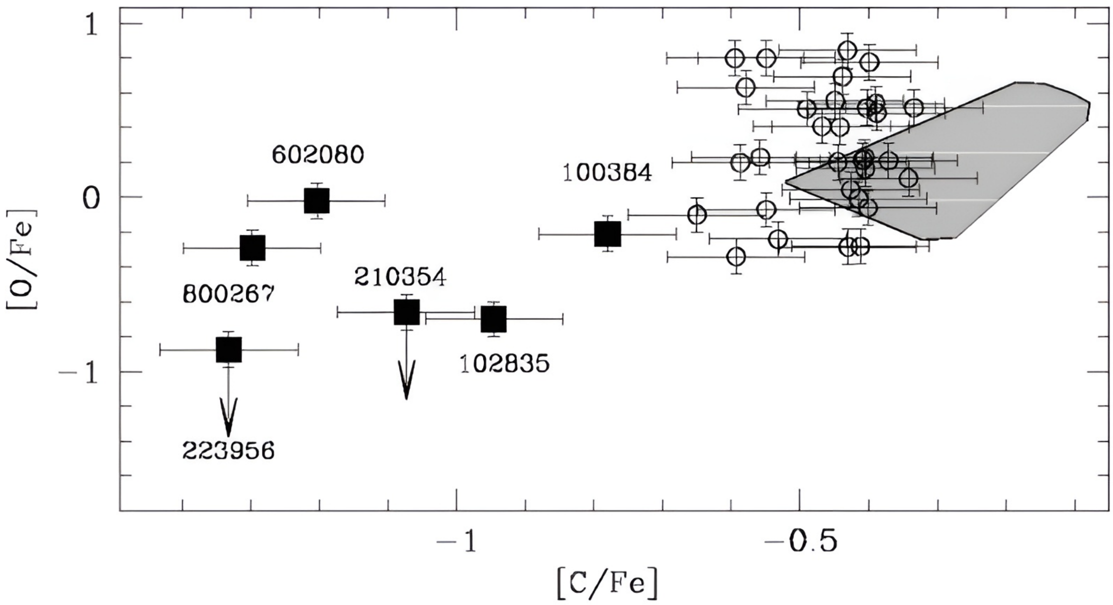

FIGURE 1.5: Carbon and oxygen abundances of the 47 BSSs observed in 47 Tucanae. The empty circles represent BSSs with normal abundances, whereas filled squares represent CO-depleted BSSs. The gray region indicates the abundances of TO stars previously studied. Figure taken from Ferraro et al. (2006b).

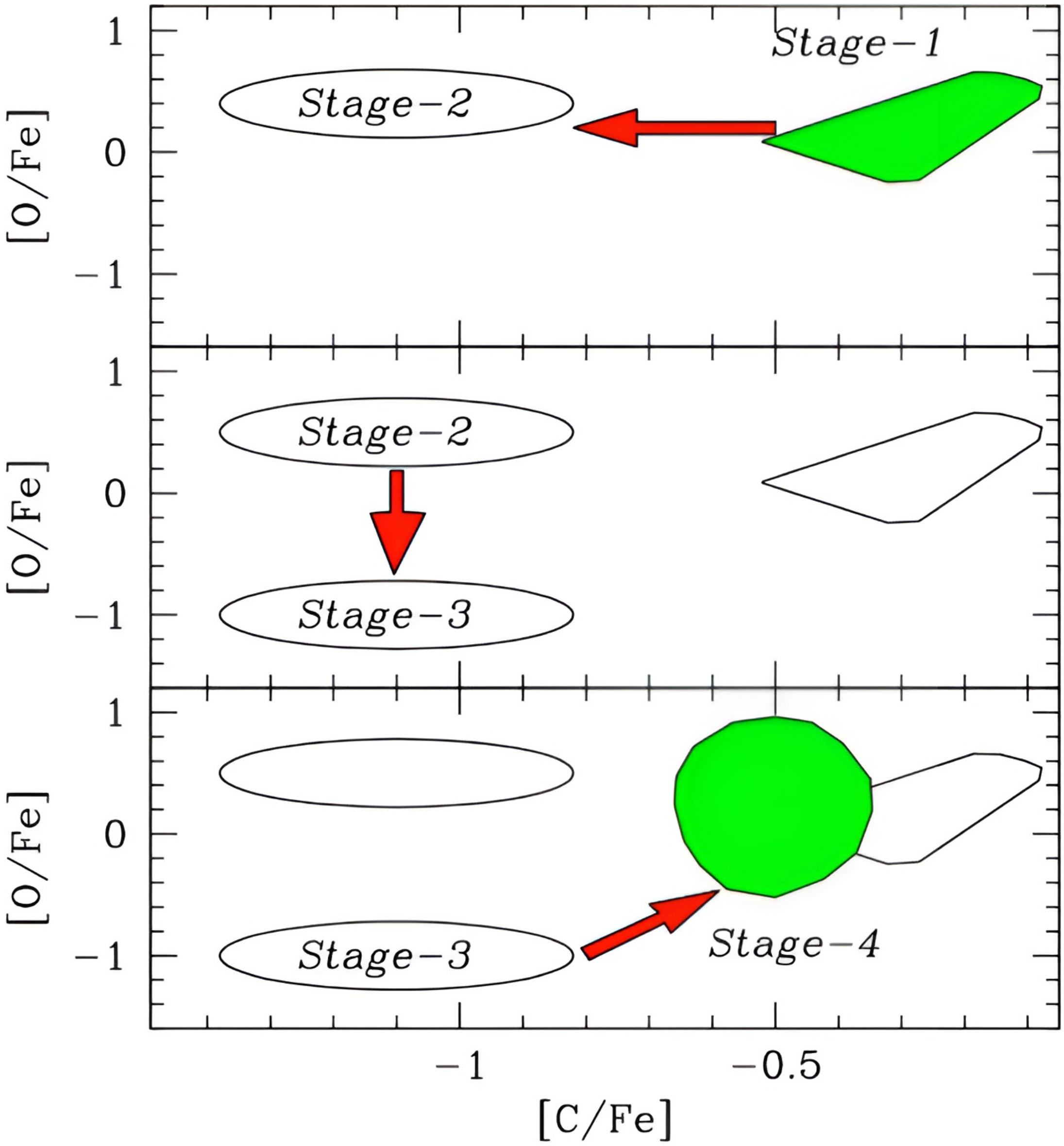

FIGURE 1.6: Suggested evolution of BSSs in the [O/Fe]-[C/Fe] diagram. Figure taken from Ferraro et al. (2015).

From a theoretical point of view, MT-BSSs are predicted to show carbon and oxygen depletion on their surface (Sarna & De Greve, 1996). In fact, during mass transfer, the material that has been partially processed by the CNO burning cycle in the innermost layers of the donor star accumulates on the surface of the BSS. Hence, this material, which is depleted in carbon and oxygen, is observable through spectroscopic measurements. On the contrary, simulations of colliding stars show that very little mixing is expected between the cores and the envelopes. Therefore, COL-BSSs are expected to show chemical abundances consistent with those of the other cluster stars (Lombardi et al., 1995). From the observational point of view, Ferraro et al. (2006b) and Lovisi et al. (2013a) found sub-samples of BSSs depleted in C and O in the GCs 47 Tucanae and M30, respectively (see Figure 1.5).

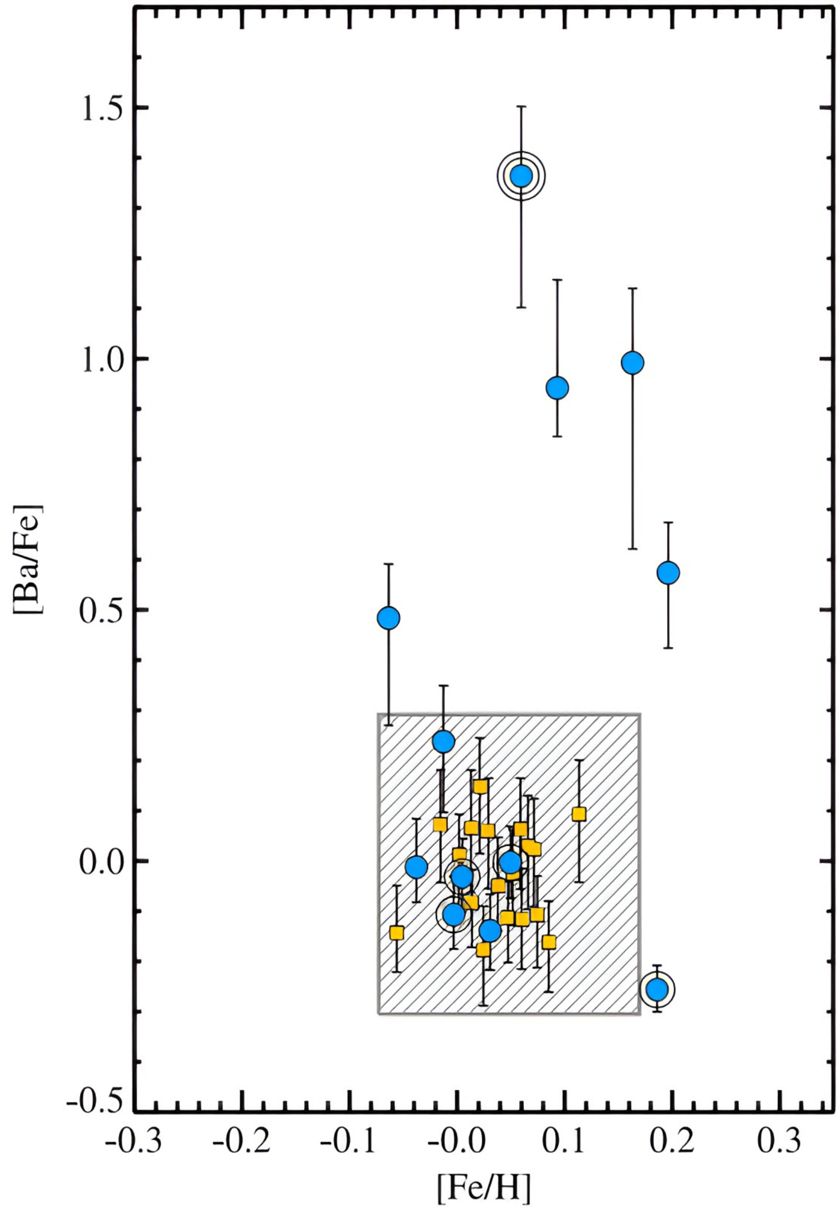

FIGURE 1.7: [Ba/Fe] as a function of [Fe/H] for the sampled BSSs (blue circles) and MS stars (orange squares). The gray hatched box marks the 3σ variation region of the MS values. Figure taken from Milliman et al. (2015).

The fact that only a fraction of BSSs shows CO depletion, could be partially explained by the fact that the remaining fraction is made of COL-BSSs. However, this would imply an unreasonably high probability of direct collisions in the investigated clusters. Hence, it has been speculated that the MT process might be divided in four different phases (see Figure 1.6). Stage 1 represents the beginning of mass transfer. In this phase the material comes exclusively

from the envelope of the donor star. Hence, no abundance variations are expected to be observed. Subsequently, the material is transferred from an inner region where C is depleted and O has a normal abundance (Stage 2). Afterwards, also material completely processed by the CNO cycle, that is depleted both in C and O, is transferred to the outer regions of the BSS (Stage 3). Finally, some mixing phenomena can happen and elemental abundances return to normal values (Stage 4). Hence, if this scenario is correct, only a fraction of MT-BSSs can be identified through chemistry.
Recent studies in OCs found another interesting chemical signature of the MT channel. Milliman et al. (2015) and Nine et al. (2024) found barium enhancement in the spectra of a subpopulation of BSSs (see Figure 1.7) in the OCs NGC 6819, NGC 7789, and M67. This has been interpreted as the signature of MT from an AGB companion to the proto-accreting BSS. In fact, barium is an s-process element produced during the AGB thermal pulses phase (Iben & Renzini, 1983; Busso et al., 1999).

1.2.4.2 Identification of the donor star

An obvious (but not easy) way to find MT-BSSs is to search for their donor stars, which lost their outer layers and should therefore be observable as hot white dwarfs. If still hot enough, a white dwarf preferentially emits at the far-UV wavelengths. Hence, photometric observations of a far-UV excess from a BSS is interpreted as the presence of a hot, peeled donor star. Over the past few years, a few companion stars to BSSs have been identified in OCs. Gosnell et al. (2014, 2015) observed an UV excess in a few BSSs in the OC NGC 188. As mentioned in Section 1.2.1, this cluster hosts a remarkably high fraction of binary systems. Hence, these observations confirm that those BSSs are likely formed through the MT mechanism. Other studies (Pandey et al., 2021; Vaidya et al., 2022), conducted with the UV Imaging Telescope on board of AstroSat, found UV excesses in the OCs M67 and NGC 7789, respectively. As mentioned in Section 1.2.4.1, an enhancement in Ba abundance has been detected in both clusters. Hence, these findings again indicate recent MT activity in these OCs.
Regarding GCs, a detection of a far-UV excess in a GGC recently emerged. Reggiani et al. (2025), using a sample of CO depleted BSSs in the GC 47 Tucanae (see Ferraro et al., 2006b), found that one BSS shows an UV excess. This represents the first time that both features have been observed simultaneously in GGCs. The absence of UV excess in the other stars of the sample does not rule out the MT formation scenario. In fact, as time passes, the white dwarf cools down and its UV emission decreases. Therefore, this feature is a transient phenomenon.

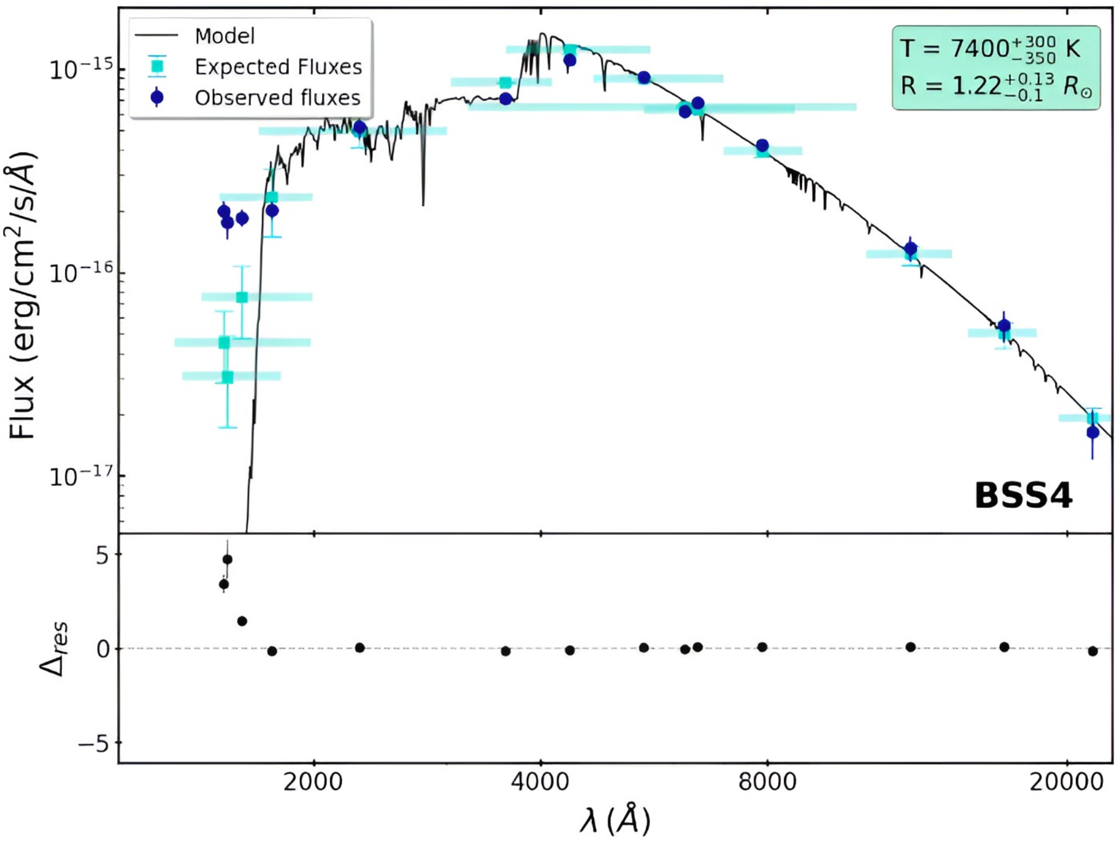

FIGURE 1.8: Observed SED (blue circles) of the BSS that shows UV excess compared to the expected fluxes (cyan squares) computed from the convolution of the best-fit synthetic SED (black line) with the adopted photometric filters. The clear excess shown at small wavelengths by the observed points with respect to the expectation from the SED that best-fits the BSS emission testfies the presence of a hot companion. Figure taken from Reggiani et al. (2025).

1.2.4.3 Photometric observations of PCC clusters

Another feature that can be used to distinguish between MT- and COL-BSS emerged from the photometric observation of BSSs in PCC clusters. Recent studies found a double BSS sequence in the CMD of the investigated clusters, which include M30 (see Figure 1.9; Ferraro et al., 2009), NGC 362 (Dalessandro et al., 2013), M15 (Beccari et al., 2019) and NGC 6256 (Cadelano et al., 2022). As mentioned in Section 1.1.2, the central density of the cluster increases significantly during the CC phase. This induces an increase in the collisional activity, leading to the rapid formation of COL-BSSs. The comparison with theoretical models of BSSs formed through collisions confirms that the blue sequence is well fitted by evolutionary models of COL-BSSs generated 1-2 Gyr ago (Sills et al., 2009). Therefore, the blue sequence has been interpreted as the evidence of recent COL-BSS formation resulting from

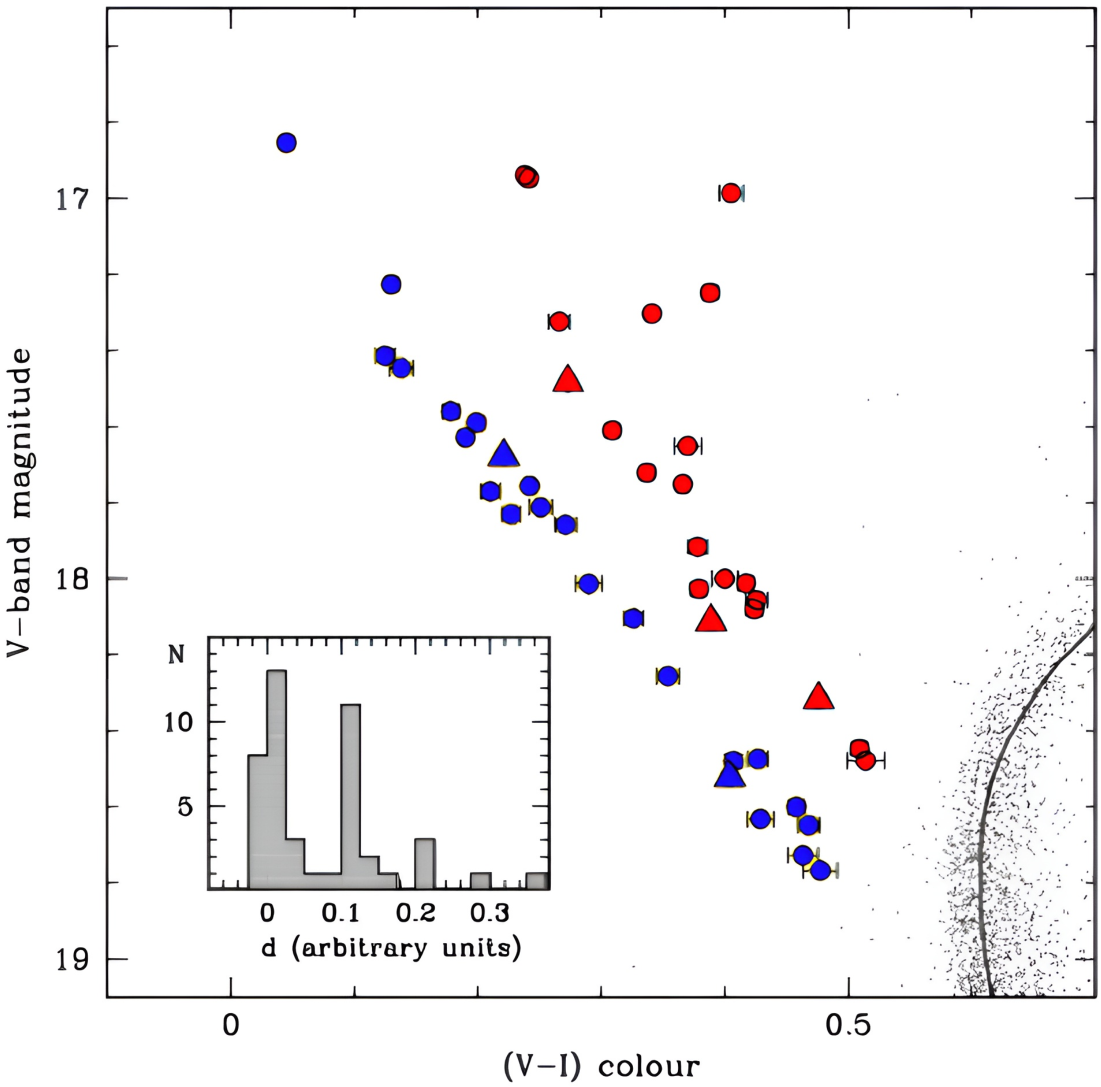

FIGURE 1.9: Zoom in the BSS region of the optical (V-I, V) CMD of M30. Blue and red dots represent COL and MT-BSSs, respectively. Figure taken from Ferraro et al. (2009).

the CC. On the contrary, the red sequence is well fitted by binary evolution models, that predict a sequence brighter by 0.75 mag than the zero-age MS. Therefore, the BSSs on the red sequence are thought to be undergoing the transfer of mass in binary systems. In addition, the observation of two well-separated sequences is evidence of recent formation of the COL-BSS population, because all MS stars tend to move to the red due to stellar evolution, thus crossing and filling the gap. Hence, the BSSs populating the blue sequence must have formed simultaneously and recently, and the observed double sequence promises to be a powerful tool to estimate the epoch of CC: based on this feature, Ferraro et al. (2009) suggest that M30 went through the CC phase 1-2 Gyr ago.

1.2.5 The "dynamical clock"

As mentioned in Section 1.2.2, BSS are more massive than standard cluster stars. Hence, they experience dynamical friction (see Section 1.1.2), which makes them gradually sink toward the innermost regions of the cluster. Therefore, the BSS radial distribution traces the dynamical age of the cluster, which differs from its chronological age (i.e., the epoch of formation of cluster stars). The empirical method used to measure the level of dynamical evolution of star clusters through the BSS radial distribution is known as "dynamical clock" (Ferraro et al., 2012).

To properly measure the level of segregation of BSSs, the double normalized ratio has been introduced (R_{BSS}; Ferraro et al., 1993). This is defined as the ratio between the fraction of BSSs observed in a radial bin and the fraction of the cluster's total light contained within that same bin, and is given by:

$$R_{BSS} = \frac{N_{BSS}/N_{BSS,tot}}{L^{sampled}/L_{tot}^{sampled}} \tag{1.9}$$

For a standard cluster population (e.g. RGB, AGB, HB), not affected by dynamical friction, the double normalized ratio is equal to one, since the number of stars follows the distribution of the cluster's integrated luminosity. Therefore, the double normalized ratio of a more massive population is an effective tool for measuring differences in radial distribution with respect to that of a lighter cluster population.

Utilizing the double normalized ratio, Ferraro et al. (2012) identified 3 different families of GCs (see Figure 1.10):

1. *Family I*: R_{BSS} is flat. The BSS radial distribution is fully consistent with that of standard (lighter) cluster stars over the entire cluster extension. This means that dynamical friction did not have sufficient time to influence the BSS population, not even in the innermost regions where it is maximally efficient. Therefore, the cluster is dynamically young (Ferraro et al., 2006a; Dalessandro et al., 2008).

2. *Family II*: R_{BSS} shows a bimodal distribution, with a peak in the cluster core, a minimum (r_{min}) at intermediate radial distances and a rising branch in the outskirts. Relative to other cluster stars there is an enhancement of BSSs in the central region, a decrease at intermediate radial distances, and a similar distribution in the outskirts. In this scenario, dynamical friction has begun to segregate the innermost fraction of the BSS population, while the most external BSSs are still unaffected. This means that GCs have an intermediate dynamical age (Ferraro et al., 1997, 2004; Mapelli et al., 2006; Lanzoni et al., 2007a).

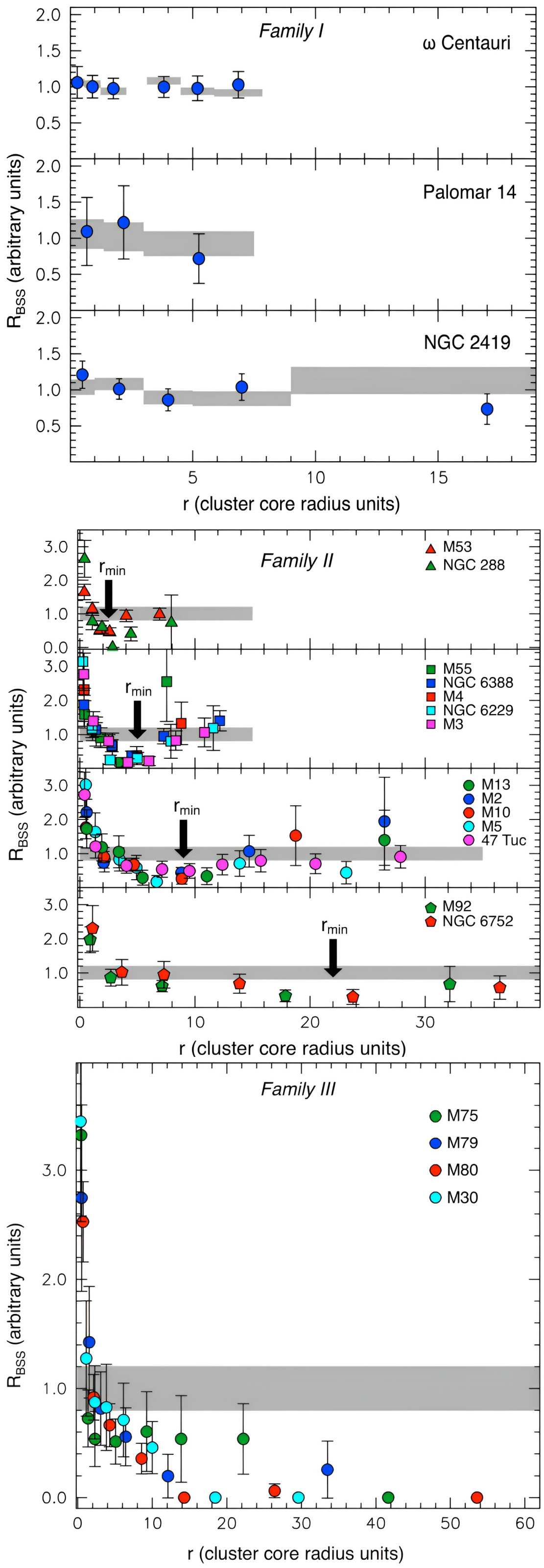

FIGURE 1.10: BSS radial distribution (colored symbols) compared to that of standard cluster stars (gray areas) in GCs with different dynamical ages and grouped in three distinct families corresponding to poor, intermediate, and high dynamical evolution (Family I, II, and III, respectively). Figure taken from Ferraro et al. (2012).

3. *Family III*: R_{BSS} shows a central peak followed by a monotonic decrease and no external upturn. In this case, dynamical friction has affected the BSS population at all radii. This behavior identifies the cluster as dynamically old (Lanzoni et al., 2007b; Ferraro et al., 2009; Contreras Ramos et al., 2012).

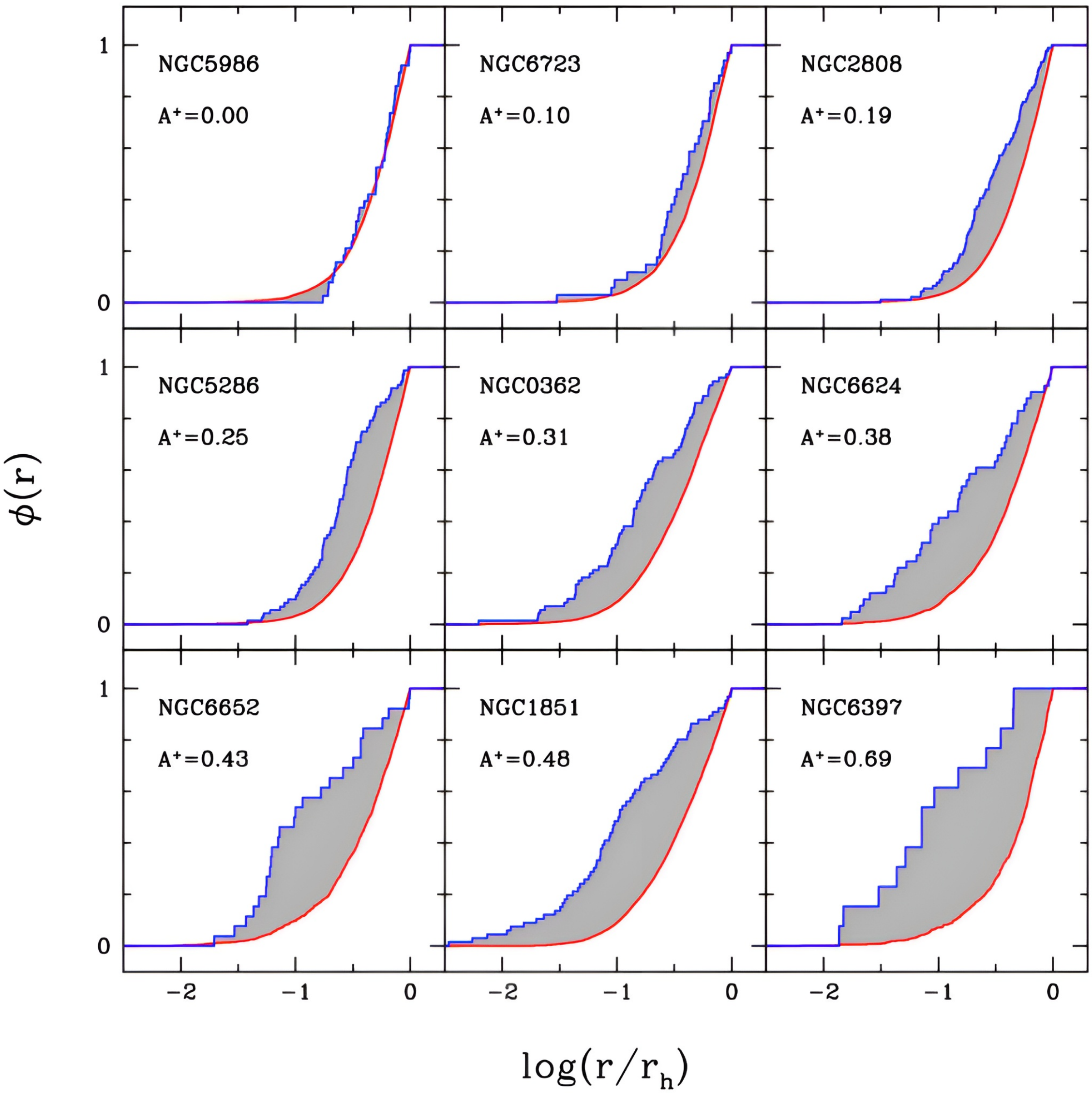

FIGURE 1.11: Cumulative radial distributions of BSS (blue line) and reference population (red line) in nine GGCs. The gray area between the two distributions represents the value of the A^+ parameter (see labels). Figure taken from Ferraro et al. (2020).

In a subsequent study Alessandrini et al. (2016) introduced the so-called A^+ parameter, which quantifies the level of BSS central segregation with no need of radial binning. It is defined as the area between the cumulative radial distributions of BSSs (ϕ_{BSS}) and of a reference population of lighter stars (ϕ_{REF}) within one half-mass radius (r_h) from the cluster center:

$$A^+(x) = \int_{x_{min}}^{x} \phi_{BSS}(x') - \phi_{REF}(x')\, dx' \tag{1.10}$$

where $x = r/r_h$. In dynamically young clusters, dynamical friction has not had enough time yet to influence the BSS population. Therefore, BSSs and reference stars have the same cumulative radial distribution and the A^+ parameter is equal to zero. As mass segregation proceeds, BSSs sink toward the cluster central regions and the two cumulative distributions start to separate, with an increasing value of the A^+ parameter (see Figure 1.11). This method has been successfully adopted to rank a large sample of GGCs (Ferraro et al., 2018a, 2023b) and extra-Galactic star clusters (Ferraro et al., 2019; Dresbach et al., 2022) in terms of their dynamical stage. Lanzoni et al. (2016) found that this parameter nicely correlates with the value of r_{min} in the dynamical clock, and anti-correlates with the cluster central relaxation time (t_{rc}). Moreover, Ferraro et al. (2018a) found a clear correlation between the A^+ parameter and N_{relax}, which quantifies the number of central relaxation times occurred during the cluster lifetime. All these correlations strongly confirm the reliability of the A^+ parameter for the determination of the dynamical age of star clusters.

1.2.6 Rotation

Rotation can add fundamental information about BSS evolutionary processes. From the theoretical point of view, high rotational velocities are expected at birth for MT-BSSs (Sarna & De Greve, 1996). In fact, during the mass transfer phase, angular momentum is also transferred from the donor star to the accreting proto-BSS. As a result, the BSS increases its rotational velocity. Unfortunately, also COL-BSSs are expected to rotate fast after their formation (Benz & Hills, 1987). To further complicate the picture, braking mechanisms (i.e. magnetic braking and disk locking) can intervene over time and slow down high rotational velocity stars, with timescales and efficiencies that are not understood yet (Leonard & Livio, 1995; Sills et al., 2005). Only recently, some observational constraint finally started to emerge. From the study of the BSS population in the old OC NGC 188, Leiner et al. (2018) suggests that post MT objects have magnetic braking timescales of $\sim$ 1 Gyr. This conclusion has been derived from the comparison between the rotation rates and the ages (as obtained from the cooling time of the white dwarf companion) of mass-transfer products, with models of angular momentum evolution of MS stars. The authors found that after 5-10 Myr these systems rotate at $\sim 30\%$ of their break-up velocities (see Figure 1.12). These values corresponds to the fastest rotations observed among solar-type stars in young clusters. Hence, post-MT stars

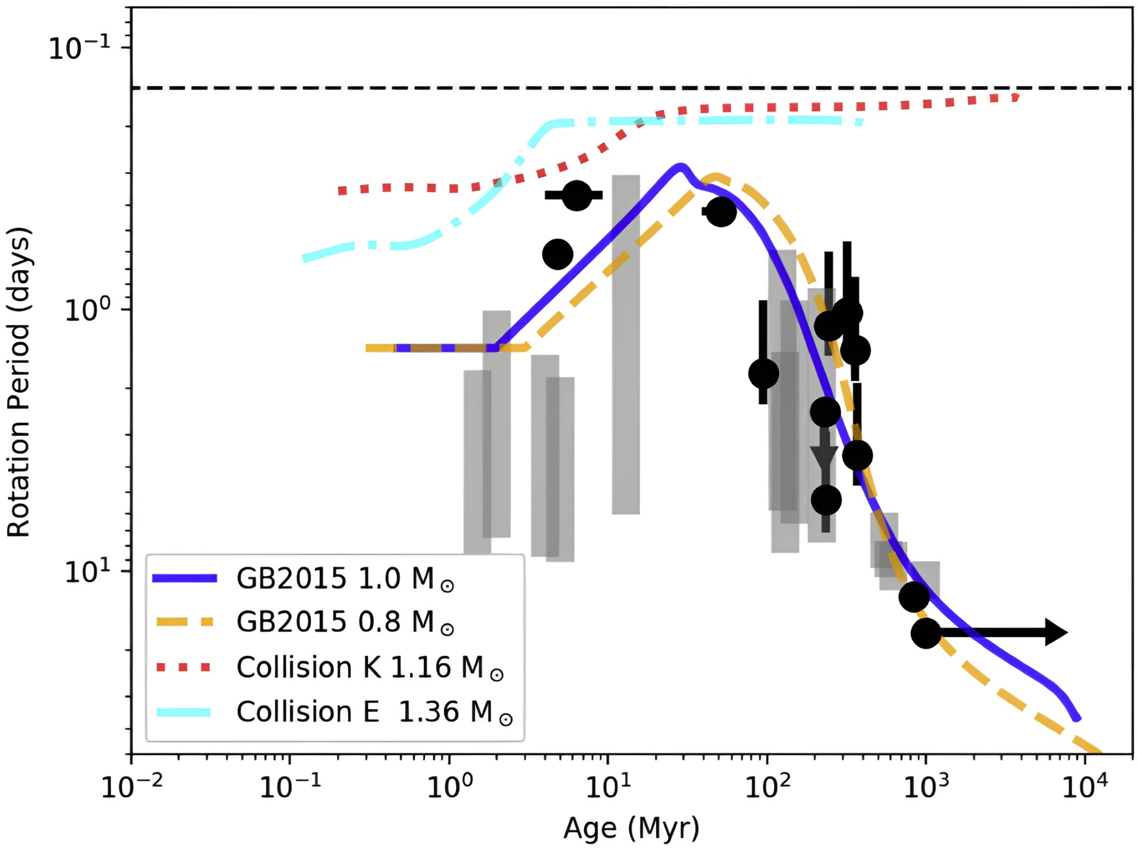

FIGURE 1.12: Rotation period as a function of the age of a sample of post mass-transfer binary systems. Figure taken from Leiner et al. (2018).

spin with timescales comparable with those of normal stars (indeed, these peculiar objects share the same structure of normal stars in terms of convective envelope and magnetic field; Gallet & Bouvier, 2015). In particular, the braking is thought to occur through angular momentum loss via a magnetized stellar wind. This result indicates that the BSS rotation rate can potentially be used as a gyro-chronometer to measure the time since the end of MT. Additional complexity is introduced by phenomena like the synchronization of close binaries (e.g., Hut, 1981), which tends to spin up the stars but is very hard to constrain observationally since it requires dedicated multi-epoch observations in both photometry and spectroscopy (see, e.g., Meibom et al., 2006; Lurie et al., 2017; Leiner et al., 2019 and references therein). Indeed, our comprehension of the processes able to slow down post-MT stars and of their characteristic timescales is just at its dawn, and any new additional piece of information is crucial. In this context, my PhD Thesis presents the results obtained from the first comprehensive systematic study of the BSS rotational velocity in a sample of GGCs with different structural characteristics.

CHAPTER 2

The BSS rotational velocity survey

2.1 The BSS rotational velocity survey before this thesis

Several years ago, our group started an extensive high-resolution spectroscopic survey using the multi-object spectrograph FLAMES-GIRAFFE mode at the Very Large Telescope (VLT) of the European Southern Observatory (ESO), see Section 2.2.1. This survey targeted GGCs with different structural parameters (e.g. King concentration and central luminosity density), with the aim to provide the chemical and rotational properties of a representative sample of BSSs formed and evolved in different environments.
The clusters that have already been studied include 47 Tucanae (Ferraro et al., 2006b), M4 (Lovisi et al., 2010), NGC 6397 (Lovisi et al., 2012), M30 (Lovisi et al., 2013a), NGC 6752 (Lovisi et al., 2013b), and ω Centauri (Mucciarelli et al., 2014).

2.1.1 47 Tucanae

The first BSS sample studied in the survey was drawn from GGC 47 Tucanae. This cluster is one of the most massive known GGCs. Its general properties are reported in Table 2.1.
The main goal of the study was to perform a spectroscopic analysis aiming at measuring the chemical abundances of carbon and oxygen in order to get information about BSS formation channels. Two different high resolution (HR) setups were used, in order to sample carbon and oxygen lines: HR22 ($R = 11,700$; $\lambda_c = 9205$ Å), and HR18 ($R = 18,300$; $\lambda_c = 7691$ Å), sampling the neutral carbon line at $\lambda \sim 9111$ Å and the neutral oxygen triplet at $\lambda \sim 7774$ Å, respectively.
As shown in Figure 1.5, a BSS sub-population was found to exhibit a CO depletion. As discussed in Section 1.2.4, this feature has been interpreted as the signature of the MT formation channel. The study of the rotational velocities of CO-depleted and normal BSSs can help to better understand this important physical property.

TABLE 2.1: General properties of the GGC 47 Tucanae

RA J2000	6°.023792	Baumgardt & Hilker (2018)
Dec J2000	-72°.081306	Baumgardt & Hilker (2018)
Mass M	$8.53 \times 10^5\ M_\odot$	Baumgardt & Hilker (2018)
Distance from Sun	4.5 kpc	Harris (1996)
Core radius r_c	0.36'	Harris (1996)
King concentration c	2.07	Harris (1996)
Central luminosity density $log\ \rho_0$	$4.88\ L_\odot\ pc^{-3}$	Harris (1996)
$[Fe/H]$	-0.74 dex	Harris (1996)
A^+_{rh} parameter	0.29	Lanzoni et al. (2016)

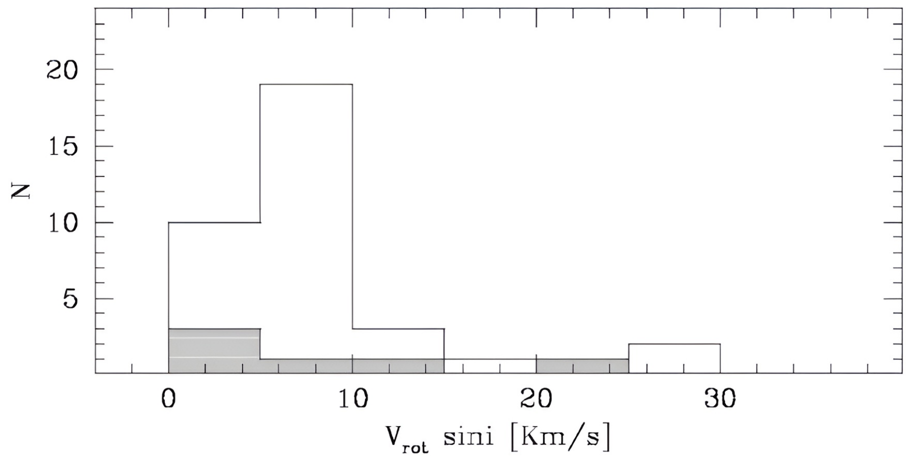

FIGURE 2.1: Rotational velocity distribution of normal BSS (unshaded histogram) compared to the CO-depleted BSS distribution (gray-shaded histogram). Figure taken from Ferraro et al. (2006b).

Figure 2.1 shows the comparison of the rotational velocity distributions of the two sub-populations. Clearly, the two distributions are indistinguishable. In particular both sub-populations have almost all the stars that rotate slower than 30 $km\ s^{-1}$. These two sub-samples seem to share also the same radial and mass distributions, with masses ranging from $\sim 0.95\ M_\odot$ to $\sim 1.35\ M_\odot$. Only one BSS of the sample have a very large rotational velocity of $\sim\ 82\ km\ s^{-1}$. It was not possible to determine the chemical abundances for this BSS due to its high rotational velocity (*v sin(i)*, with *i* being the inclination angle on the plane of the sky). Interestingly, the most rapid rotators in their sample are concentrated in the outer regions of the cluster, with the fastest one located more than $9'$ from the cluster center.

2.1.2 M4

The second study of the survey analyzes the chemical and rotational properties of BSSs in the GC M4, in order to obtain information on their formation mechanisms.

TABLE 2.2: Main physical properties of the GGC M4

RA J2000	245°.89674	Baumgardt & Hilker (2018)
Dec J2000	-26°.52575	Baumgardt & Hilker (2018)
Mass M	$9.04 \times 10^4\ M_\odot$	Baumgardt & Hilker (2018)
Distance from Sun	2.2 kpc	Harris (1996)
Core radius r_c	1.16'	Harris (1996)
King concentration c	1.65	Harris (1996)
Central luminosity density $log\ \rho_0$	$3.64\ L_\odot\ pc^{-3}$	Harris (1996)
$[Fe/H]$	-1.16 dex	Harris (1996)
A^+_{rh} parameter	0.12	Lanzoni et al. (2016)

Table 2.2 reports the main physical properties of this cluster, which exhibits a significantly lower concentration and stellar density compared to 47 Tucanae.

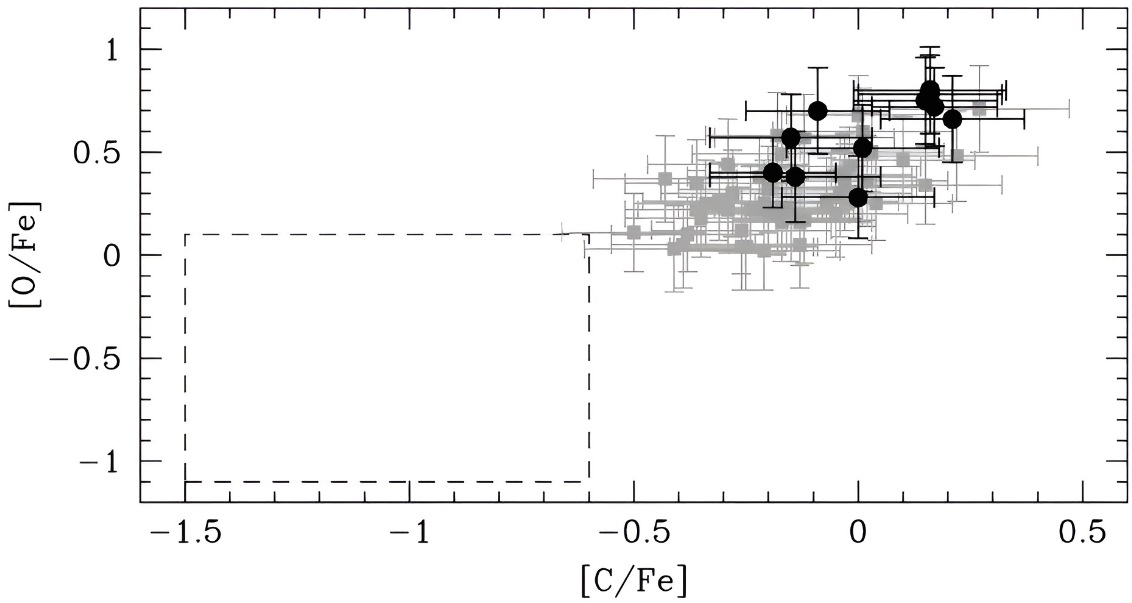

FIGURE 2.2: [O/Fe] ratio as a function of [C/Fe] for the measured BSSs (black dots) and SGBs (gray dots). The dashed box marks the position of the CO depleted BSSs observed in 47 Tucanae. Figure taken from Lovisi et al. (2010).

The dataset consists of 20 BSSs, 53 SGB stars and 38 RGBs. Three different setups of FLAMES-GIRAFFE have been used for the spectroscopic observations: HR15 ($R \sim 21,300$; $\lambda_c \sim$

6797 Å), HR18, and HR22 in order to observe the *Hα* line, as well as the same oxygen and carbon lines previously analyzed in 47 Tucanae.
Interestingly, five BSSs exhibit anomalous radial velocity values. By analyzing proper motions and comparing metallicities with the field distribution, the authors concluded that these anomalous stars belong to the cluster.

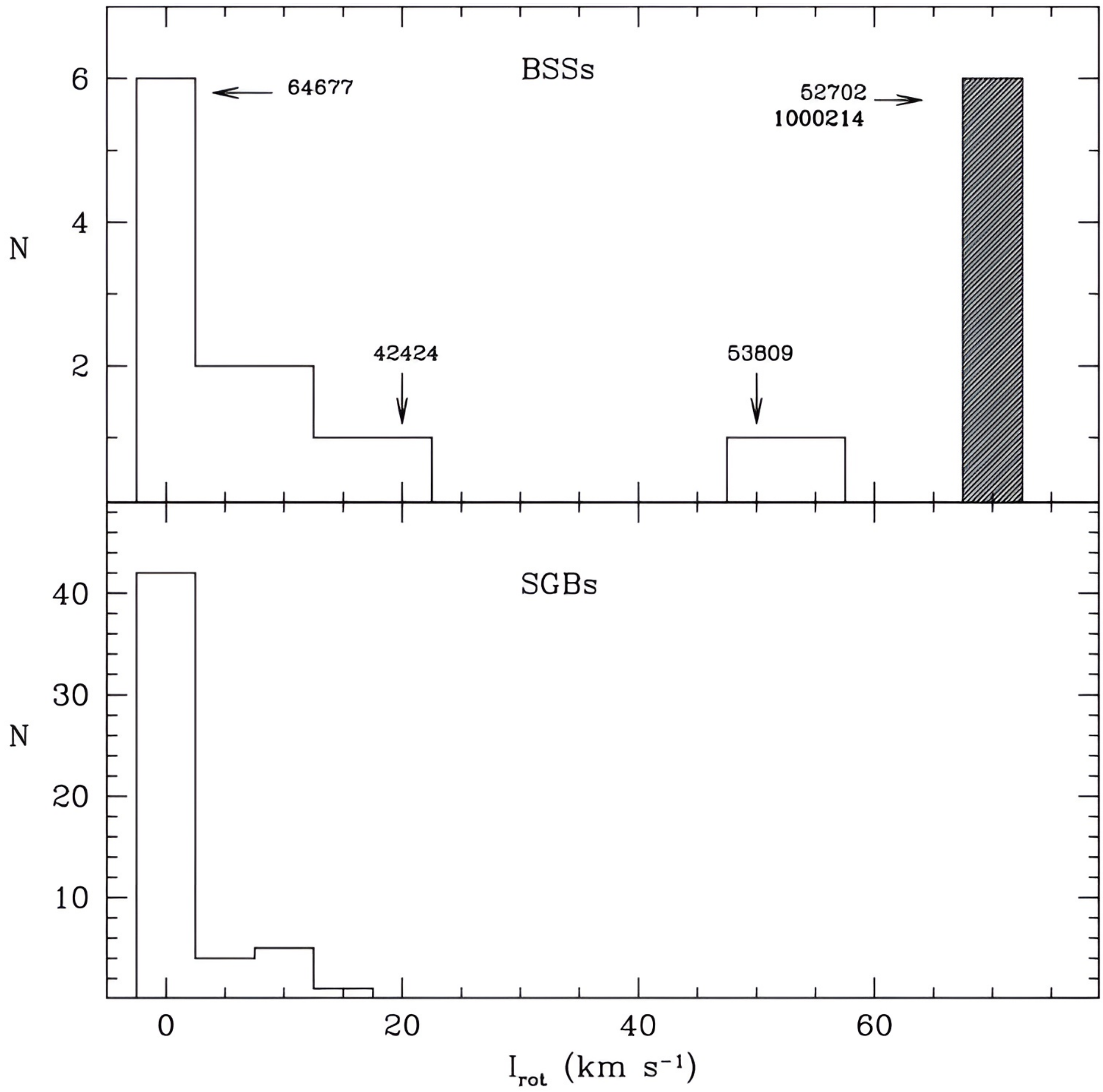

FIGURE 2.3: Rotational velocity distribution of BSSs (upper panel) and SGB stars (lower panel). The six fast rotating BSSs are plotted within the gray shaded block. Figure taken from Lovisi et al. (2010).

Contrary to that found for the previous cluster, chemical analysis did not reveal any signatures of CO depletion. The carbon and oxygen abundances of BSSs are fully consistent with those of the SGB stars. The absence of CO depleted BSSs may be an effect of low statistics and is still consistent with the expectations. Alternatively, it might be the signature of the COL scenario, for which chemical anomalies are not expected. This scenario is less likely, as the majority of BSSs in GCs are believed to form through a MT process (Ferraro et al., 2026). Moreover, as discussed in Section 1.2.4.1, CO depletion is a transient phenomenon and its absence does not entirely rule out the MT scenario.

Figure 2.3 shows the rotational velocity distribution of BSSs and SGBs[1]. In the case of SGB stars, all exhibit rotational velocities below 20 $km\ s^{-1}$, while a significant fraction of BSSs ($\sim$ 40%) rotate faster than 40 $km\ s^{-1}$. This is the first time that such a high fraction of fast-spinning BSSs has been observed. The fastest BSS in the dataset has a rotational velocity value of 150 $km\ s^{-1}$ and has been classified as W Ursae Majoris (W UMa), a type of contact binary variable characterized by a common envelope with ongoing mass and angular momentum transfer.

The fast spinning BSSs are distributed at all luminosities, temperatures and radial distances. Regarding the radial distribution there is no statistical significant that fast and slow spinning BSSs have two distinct radial distributions.

Interestingly enough, three out of five BSSs that show radial velocity anomalies have a large value of rotational velocity. For these stars they proposed a scenario in which the anomalies in radial and rotational velocity are caused by three and four body encounters in the cluster core. The effect of these interactions could have originated and kicked out fast spinning BSSs towards the outskirts of the cluster (two of them are located well beyond the cluster core radius).

2.1.3 NGC 6397

TABLE 2.3: Main physical properties of the GGC NGC 6397

RA J2000	265°.17538	Baumgardt & Hilker (2018)
Dec J2000	-53°.67434	Baumgardt & Hilker (2018)
Mass M	$8.24 \times 10^4\ M_\odot$	Baumgardt & Hilker (2018)
Distance from Sun	2.3 kpc	Harris (1996)
Core radius r_c	0.05'	Harris (1996)
King concentration c	2.50	Harris (1996)
Central luminosity density $log\ \rho_0$	5.76 $L_\odot\ pc^{-3}$	Harris (1996)
$[Fe/H]$	-2.02 dex	Harris (1996)
A^+_{rh} parameter	0.69	Ferraro et al. (2018a)

The third study on BSS chemical and rotational properties was published by Lovisi et al. (2012) and focuses on spectroscopic observations of BSSs in the cluster NGC 6397.

Table 2.3 shows the main physical properties of this GGC. Currently, NGC 6397 is the most

[1] Note that here they used I_{rot} which is linked to *v sin(i)* by means of a coefficient α: $I_{rot} = v\ sin(i)/\alpha$. The comparison with synthetic spectra indicates that α is close to unity.

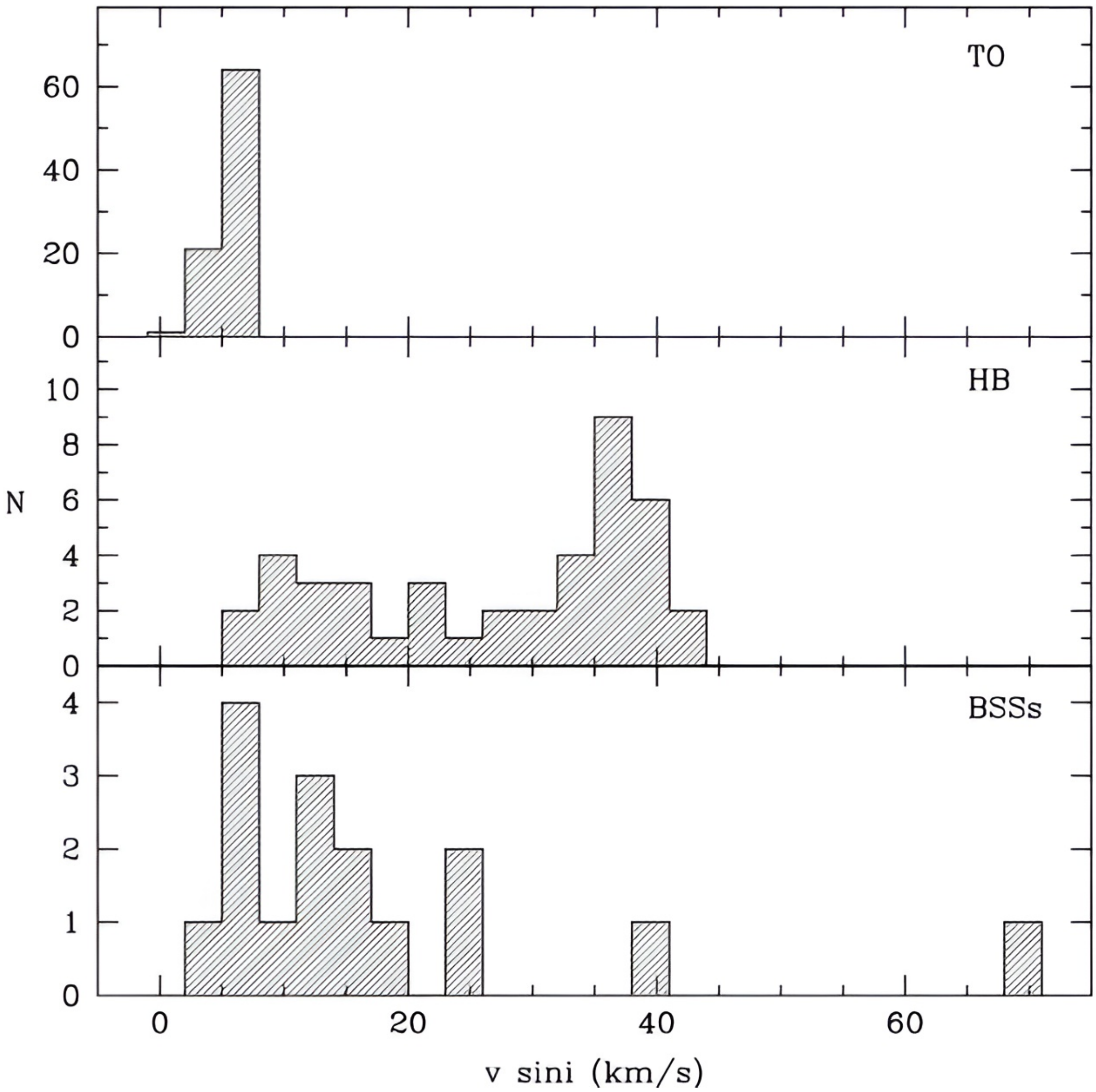

FIGURE 2.4: Rotational velocity distribution for TO (upper panel), HB stars (middle panel), and BSSs (lower panel) . Figure taken from Lovisi et al. (2012).

dense cluster of the survey. This cluster underwent the CC (see Section 1.1.2), which resulted in an increase in its central density. The observed dataset consists of 18 BSSs, 42 HBs, 86 MS-TO and SGB stars. They used different setups in order to sample different spectral lines: HR5A ($R \sim 20,250$; $\lambda_c \sim 4471$ Å) that samples Fe and Mg lines, HR18 for oxygen neutral lines and HR15N ($R \sim 19,200$; $\lambda_c \sim 6650$ Å) that samples the Hα line.
Regarding the chemical and rotational properties of TO stars, they found good agreement with previous studies. In particular, these stars exhibit low rotational velocities, with a mean value $\sim 7\ km\ s^{-1}$, and a homogeneous distribution in their chemical abundances. Instead, BSSs and HBs show different *v sin(i)* distributions (see Figure 2.4). In particular, HB stars

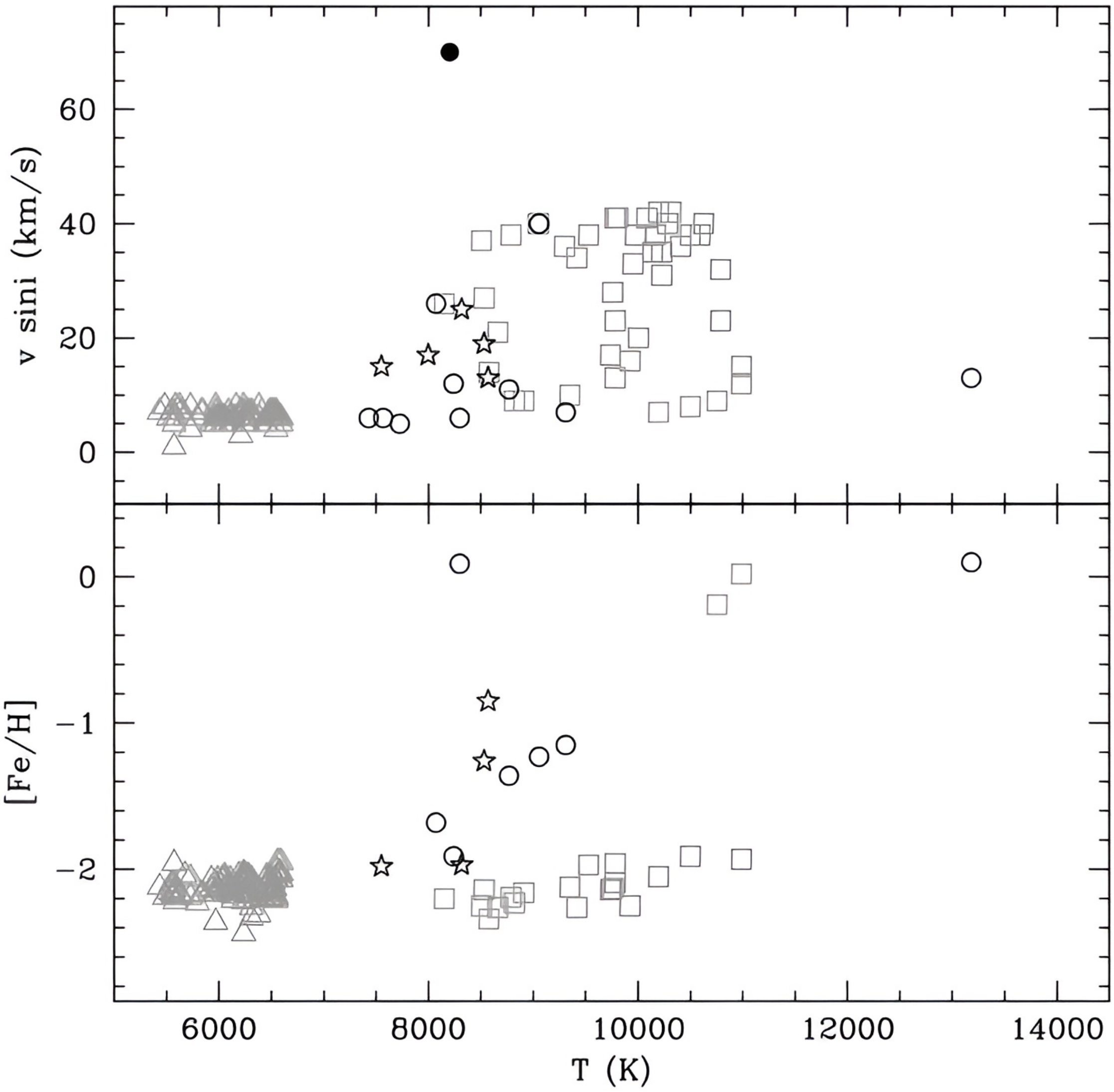

FIGURE 2.5: Rotational velocities (top panel) and [Fe/H] (bottom panel) as a function of the stellar temperatures for TO (empty gray triangles), HB (empty gray squares), and BSSs (same symbols used in the previous figures). Figure taken from Lovisi et al. (2012).

exhibit a slightly broader rotational velocity distribution, with values ranging between 5 to 40 $km\ s^{-1}$, in agreement with previous findings reported in the literature. In this context, Hubrig et al. (2009) previously measured the rotational velocity of three blue HB stars belonging to this cluster obtaining *v sin(i)* $\sim 8 - 10\ km\ s^{-1}$. Moreover, Behr et al. (2000a) found a discontinuity in the stellar rotational velocity around $T_{eff} \sim 11,000\ K$ in the HB of M13. Blue-ward HB stars show modest rotation (*v sin(i)* $< 10\ km\ s^{-1}$), whereas the red-ward side has several fast spinning stars (up to 40 $km\ s^{-1}$). A similar trend has been found by the same authors in the GGC M15 (Behr et al., 2000b). Furthermore, Recio-Blanco et al. (2002) studied HB belonging to four different GCs. Firstly, they found that all the hot stars

($T_{eff} > 11,500\ K$) are slow rotators, with *v sin(i)* $< 12\ km\ s^{-1}$. In particular, in the GC M79 they found that half of the stars cooler than that temperature are fast spinning stars, whereas in NGC 2808 and M80 they did not find evidence of fast spinning HB objects. Another study (Behr, 2003) found similar results. In some clusters, approximately one third of the cooler HB stars rotate quite fast (*v sin(i)* $\sim 30 - 40\ km\ s^{-1}$), while the other two thirds have a modest value. Different possible explanations have been raised, e.g. core retention of angular momentum in the MS lifetime, results of stellar mergers or non-merger interactions. Although different scenarios have been suggested, the HB rotational velocity distributions still remain an open challenge.

The rotational velocity distribution of BSSs is even broader, with *v sin(i)* ranging from 0 to $70\ km\ s^{-1}$. Additionally, a systematic trend of iron abundance with the temperature has been observed (see Figure 2.5). The coldest BSSs have a [Fe/H] partially in agreement with TO stars, whereas for stars with $T > 8200\ K$, [Fe/H] enhances to solar iron abundance. This is a hint that, at high temperatures, an element transport mechanism driven by radiative levitation occurs. This scenario is also supported by the He depletion. Helium is progressively transported toward the inner regions of the star due to gravitational settling, with a resulting decrease in its surface abundance. This mechanism is much more effective in absence of rotation, which would prevent the metal levitation. In this regard, no trend between [Fe/H] abundance and rotation has been found.

2.1.4 M30

M30 is the first cluster in which two distinct sequences of BSSs (see Figure 1.9), thought to be the signature of the double formation scenario likely triggered by the effects of CC, have been observed (Ferraro et al., 2009).

TABLE 2.4: Main physical properties of the GGC M30

RA J2000	325°.09213	Baumgardt & Hilker (2018)
Dec J2000	-23°.17986	Baumgardt & Hilker (2018)
Mass M	$1.21 \times 10^5\ M_\odot$	Baumgardt & Hilker (2018)
Distance from Sun	8.1 kpc	Harris (1996)
Core radius r_c	0.06'	Harris (1996)
King concentration c	2.50	Harris (1996)
Central luminosity density $log\ \rho_0$	$5.01\ L_\odot\ pc^{-3}$	Harris (1996)
$[Fe/H]$	-2.27 dex	Harris (1996)
A^+_{rh} parameter	0.52	Lanzoni et al. (2016)

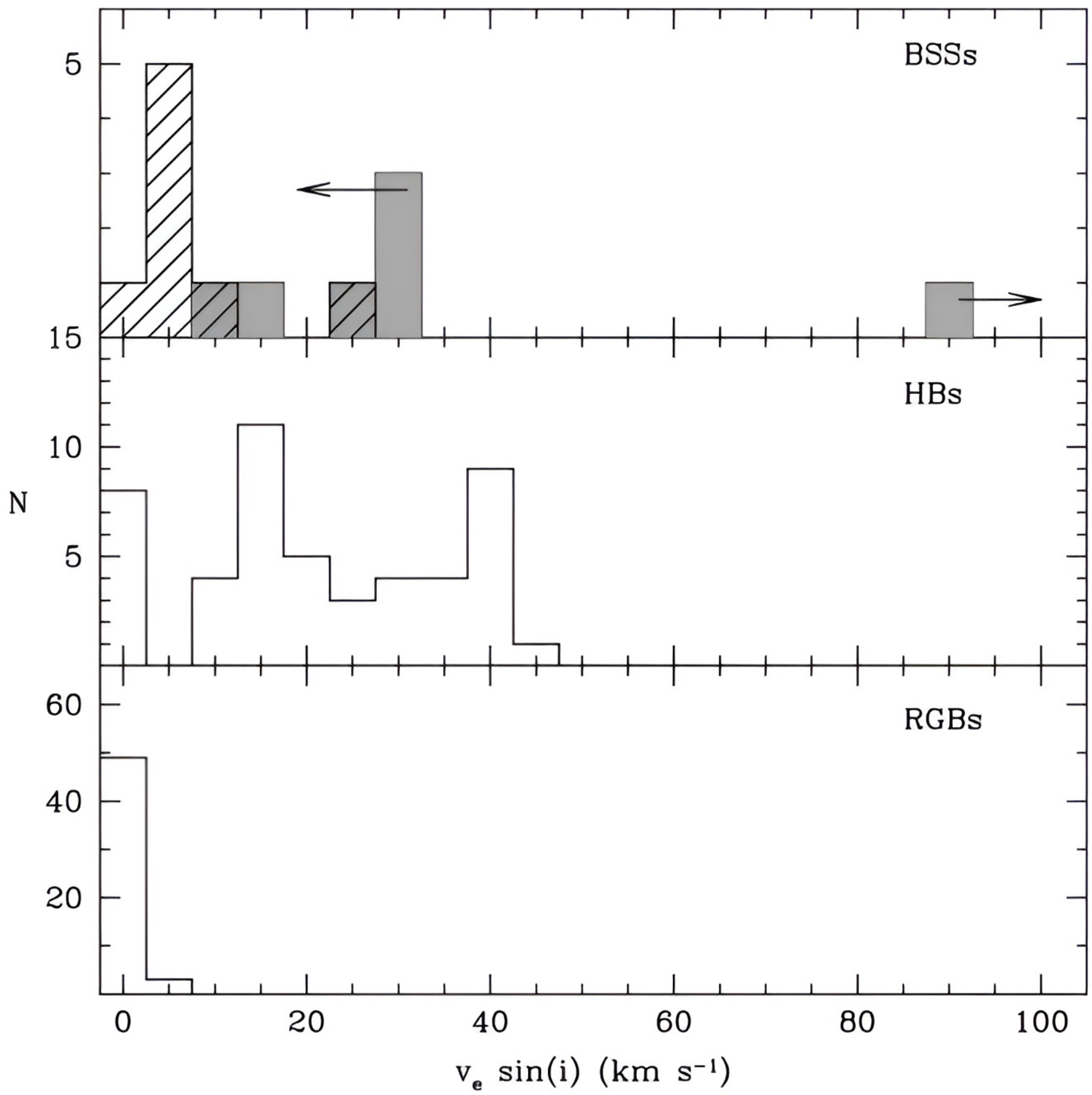

FIGURE 2.6: Rotational velocity distribution of BSSs (upper panel), HB stars (middle panel) and RGB stars (lower panel) that belong to the cluster M30. In the upper panel, gray and shaded histograms represent blue and red sequence BSSs, respectively. Figure taken from Lovisi et al. (2013a).

Table 2.4 shows the main physical properties of this GGC, which is a very old, dense, highly concentrated PCC GC, such as NGC 6397. The spectroscopic dataset consists of 15 BSSs, seven of them selected from the blue sequence and eight from the red one. Observations have been performed with FLAMES and XSHOOTER, both mounted at the Unit Telescope (UT) 2 at the VLT@ESO. Regarding FLAMES, HR5A and HR18 have been adopted in order to sample some metallic lines and the neutral oxygen line used in the previous works. Typical signal-to-noise ratio (SNR) values range from 30 to 70 for BSSs and ≥ 80 for RGBs and HBs. The FLAMES sample includes 12 BSSs (four and eight of them belonging to the blue and red sequences, respectively), 52 RGBs and 49 HB stars. The other three BSSs have been observed with XSHOOTER. These targets have been observed in stare mode allowing simultaneously observations for the UVB (slit of 0.8"; $R = 6,200$) and VIS (slit of 0.7"; $R = 11,000$). Although the spectral resolution is much lower than that of FLAMES, these stars are too faint ($V \sim 18$) to be observed with FLAMES within a reasonable exposure time. Therefore, XSHOOTER can be useful to infer some more information.

As observed in NGC 6397, the distribution of BSS rotational velocities is significantly broader than that of RGB stars (see Figure 2.6). The majority of BSSs are quite slow rotators, $v\ sin(i) < 30\ km\ s^{-1}$, with one exceptional star that has $v\ sin(i) > 90\ km\ s^{-1}$. This BSS distribution is much more similar to the ones observed in 47 Tucanae and NGC 6397, while M4 exhibits a noticeably broader distribution. Unfortunately, almost all stars in both sequences are slow rotators, although those in the blue sequence tend to have slightly higher rotational velocities than those in the red sequence (see upper panel of Figure 2.6).

From a chemical point of view, an increase of BSS iron abundances with the increasing of the temperature has been observed, in agreement with findings in NGC 6397. This evidence supports the scenario of particle transport mechanism driven by the radiative levitation for BSSs with $T \sim 8,000\ K$. In this regard, NGC 6397 and M30 are the first two clusters in which the effect of radiative levitation has been observed among the BSS population. Although a sub-population of BSSs is affected by radiative levitation, some BSSs show [Fe/H] ratios completely compatible with the cluster ones. This certifies that the surface abundances are not altered by the radiative levitation. This allowed them to study the chemical composition of those stars. In this regard, an intriguing result emerges from the observations of the oxygen abundances. In four out of five red cold BSSs the estimated oxygen abundances are significantly lower than those measured in "normal" cluster stars, such as those long the HB and RGB. The more probable scenario is the oxygen depletion due to the MT origin of the red sequence (in according to what affirmed in Ferraro et al., 2009). Unfortunately, blue BSSs are too faint to be observable with FLAMES. Moreover, the low metallicity of this cluster did not allow to measure the carbon abundance.

2.1.5 NGC 6752

NGC 6752 is the fifth cluster studied in the chemical and rotational GC survey.

Similar to NGC 6397 and M30, this cluster appears to have undergone CC. The observed dataset consists of 22 BSSs and 26 RGB stars. Four different setups were used (HR5A, HR15N, HR18 and HR22A) to sample metallic lines, the neutral oxygen triplet and carbon lines at $\lambda \sim 9078.3$ and 9111.8 Å.

TABLE 2.5: Main physical properties of the GGC NGC 6752

RA J2000	287°.717102	Baumgardt & Hilker (2018)
Dec J2000	-59°.984554	Baumgardt & Hilker (2018)
Mass M	$2.61 \times 10^5\ M_\odot$	Baumgardt & Hilker (2018)
Distance from Sun	4.0 kpc	Harris (1996)
Core radius r_c	0.17'	Harris (1996)
King concentration c	2.50	Harris (1996)
Central luminosity density $log\ \rho_0$	$5.04\ L_\odot\ pc^{-3}$	Harris (1996)
$[Fe/H]$	-1.54 dex	Harris (1996)
A^+_{rh} parameter	0.33	Lanzoni et al. (2016)

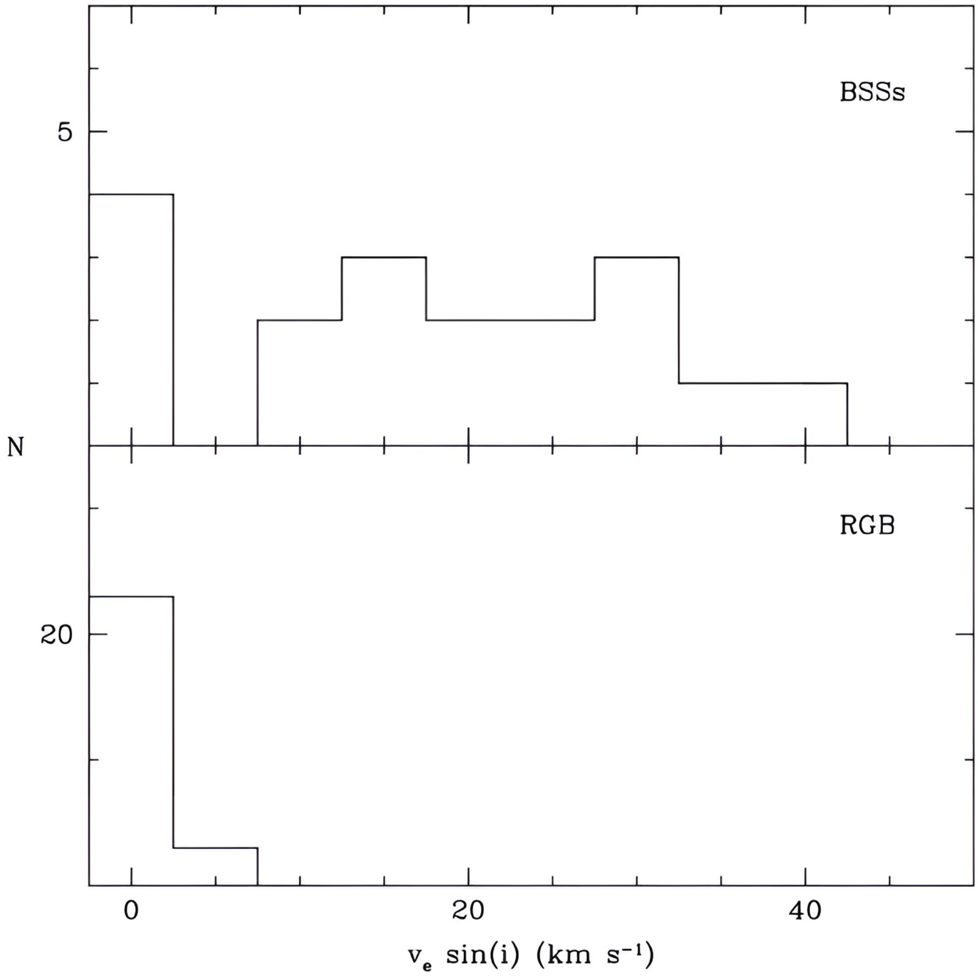

FIGURE 2.7: Rotational velocity distribution of BSSs (upper panel) and RGB stars (lower panel). Figure taken from Lovisi et al. (2013b).

Figure 2.7 shows the *v sin(i)* distribution of BSSs and RGB stars belonging to this GGC. As expected there is a clear difference between the two distributions. In particular, BSS population has a broader distribution than that of RGB, although no BSSs with *v sin(i)* > $40\ km\ s^{-1}$ were observed. Interestingly, all the four clusters of the sample with a small fraction of very fast spinning BSSs are high-density and dynamically evolved clusters. Indeed, three out of four clusters already experienced the collapse of the core.

From the chemical analysis emerges that the sampled BSSs, not affected by the radiative levitation, do not show any CO depletion. As said for NGC 6397, one possible explanation is low statistics. Another explanation might be that these BSSs formed via the COL channel, for which chemical anomalies are not expected. This would be in agreement with the dynamical state, i.e. PCC, of this cluster.

2.1.6 ω Centauri

TABLE 2.6: Main physical properties of ω Centauri

RA J2000	201.°69699	Baumgardt & Hilker (2018)
Dec J2000	-47.°47947	Baumgardt & Hilker (2018)
Mass M	$3.94 \times 10^6\ M_\odot$	Baumgardt & Hilker (2018)
Distance from Sun	5.2 kpc	Harris (1996)
Core radius r_c	2.37'	Harris (1996)
King concentration c	1.31	Harris (1996)
Central luminosity density $log\ \rho_0$	$3.15\ L_\odot\ pc^{-3}$	Harris (1996)
$[Fe/H]$	-1.53 dex	Harris (1996)
A^+_{rh} parameter	-0.01	Lanzoni et al. (2016)

ω Centauri is one of the most complex stellar systems present in the MW. Indeed, it is quite massive, with a mass of $3.94 \times 10^6\ M_\odot$ (Baumgardt & Hilker, 2018) but the impressive characteristic is its iron distribution. In fact, typical GCs have a broader distribution of light elements and a narrow distribution of heavy elements. However, this system has a metallicity distribution that spans almost 2 dex, from ~ 2.2 up to ~ 0.5 dex (Johnson & Pilachowski, 2010; Mészáros et al., 2021), with a mean value $[Fe/H] = -1.53$ dex (Harris, 1996). Although, it could be considered as the bulge of a disrupted dwarf galaxy (Bekki & Freeman, 2003), studies carried out in the last decades demonstrates that this system behaves like a GC. In particular, this GC-like stellar system harbor the largest known BSS population number

($\sim$ 300 stars; Ferraro et al., 2006a). As shown in Table 2.6, it is a moderately loose and low-concentrated stellar system.
For this cluster Mucciarelli et al. (2014) observed a dataset of 109 BSSs (the largest dataset of the survey), that includes two samples acquired with FLAMES, VLT@ESO. The first sample has been observed with HR5A, HR14A ($R = 18,000$, $\lambda_c = 6515$Å) and HR15N setups. For the second dataset has been used HR2 ($R = 22,700$, $\lambda_c = 3958$Å) and HR4 ($R = 24,000$, $\lambda_c = 4297$Å). The line used to determine the rotational velocity is the Ca II K line, which is a robust diagnostic because it remains observable even at very high rotational velocities.

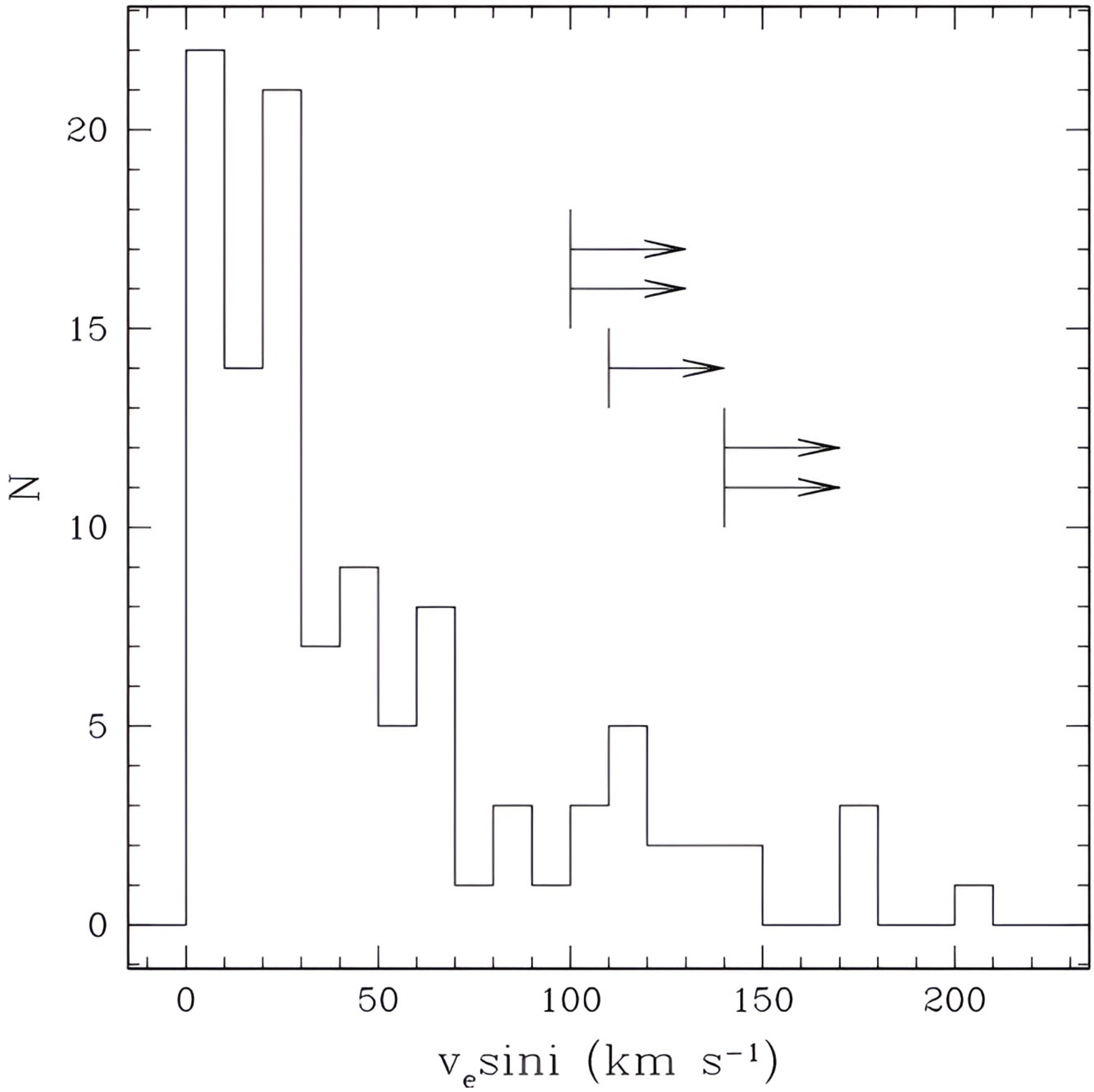

FIGURE 2.8: Rotational velocity distribution of the sampled BSSs in ω Centauri. Figure taken from Mucciarelli et al. (2014).

Figure 2.8 shows the *v sin(i)* distribution of the sampled BSSs in ω Centauri. The distribution has a peak at low rotational velocity and a long tail at large values, reaching also 200 $km\ s^{-1}$.

44 out of 109 stars ($\sim 40\%$ of the sample) have large *v sin(i)* values ($> 40\ km\ s^{-1}$). This is very interesting because it is the second cluster in the survey with a high fraction of fast-rotating BSSs.

2.1.7 The presence of an anti-correlation?

Interestingly, both clusters showing a high fraction of fast rotating BSSs are moderately loose systems. On the contrary, the four high-density and more concentrated clusters of the survey have a much smaller fraction of fast spinning BSSs. Hereafter, we will consider as fast rotating (FR) BSSs the stars that have a *v sin(i)* $\geq 40\ km\ s^{-1}$. The threshold has been selected by considering the observed rotational velocity distributions, since it has been noted that some clusters show a clear drop in the fraction of FR-BSSs in correspondence with this value. Nevertheless, it has been demonstrated that choosing a slightly different threshold (such as 30 or 50 $km\ s^{-1}$) has no impact on the results (see Ferraro et al., 2023a). As shown in Figure 2.9, there appears to be a possible correlation between the fraction of FR-BSSs and the cluster King concentration or the central luminosity density. However, given the limited sample of only six clusters studied, constraining the shape of the distribution remains challenging, especially because of the scarcity of systems in the low- and intermediate-density regimes.

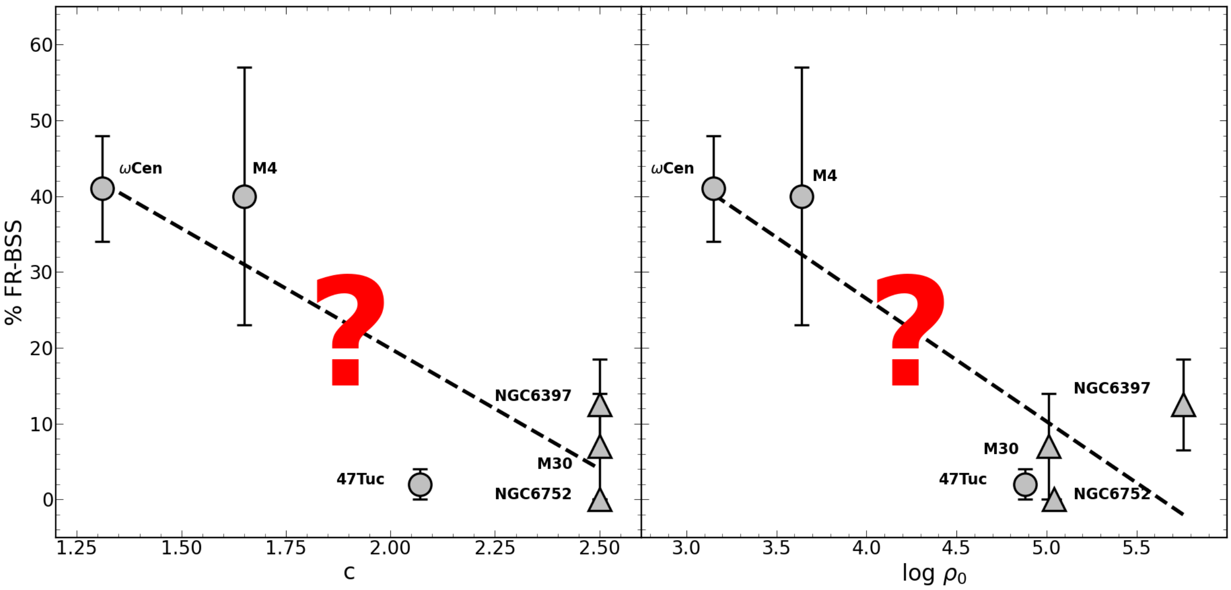

FIGURE 2.9: Percentage of FR-BSSs as a function of the King concentration c and the central luminosity density $log\ \rho_0$ for the six clusters of the survey published before this thesis.

2.2 The BSS rotational velocity survey: this thesis

The aim of this PhD Thesis is the determination of the rotational velocity of a representative sample of BSSs in three low/intermediate concentrated clusters (namely, NGC 3201, M55, and NGC 1851), not only to verify the existence of the suspected relation between the fraction of FR-BSSs and the cluster density, but also to collect new additional information about the physical properties of these puzzling stars.

2.2.1 Telescopes and instruments

The spectroscopic observations analyzed in this thesis have been carried out with two ground-based telescopes located in Chile: the Magellan Telescope located at Las Campanas Observatory, and the VLT@ESO located at Cerro Paranal.
The spectrographs that have been used to observe BSSs are the Michigan/Magellan Fiber System (M2FS, Mateo et al., 2012) for the Magellan Telescope, and FLAMES in the GIRAFFE MEDUSA mode for the VLT (Pasquini et al., 2002; see Figure 2.10).
M2FS is composed of two twins spectrographs that simultaneously observe stellar light in the same spectral range. Each one is equipped with 128 fibers with a resolution that ranges from few hundreds ($\sim$ 200) to tens of thousands ($\sim$ 34,000).
FLAMES is mounted on UT2 of the VLT. The field of view is $\sim$ 25' in diameter. It has two different spectrographs, GIRAFFE and UVES fiber mode, that cover the entire optical spectral range. GIRAFFE MEDUSA mode is fed by 132 fibers that can be used simultaneously for each exposition and a resolution ranging from 5,000 to 30,000. In this mode, each fiber has an aperture of 1.2" on the sky. Each fiber is designed to collect the light of a single star. UVES fiber mode, instead, has only 8 fibers with a resolution $R \sim 47{,}000$.
These instruments are fiber-fed systems, that allow us to obtain multiple stellar spectra within a single exposure. Since we need to observe a large number of stars and the time needed to obtain a useful SNR is long, a fiber-fed system is an ideal instrument to efficiently and simultaneously obtain high-resolution (R $\sim$ 20,000) spectra for many objects in the same stellar system. Approximately ten fibers are allocated to collect sky background, which must be subtracted from the stellar spectra. The high resolutions of the instruments allow us to have a high precision in the estimation of the rotational velocity uncertainty. With a resolution of $\sim$ 20,000, the rotational velocity uncertainty is of the order of a few km s^{-1}.

FIGURE 2.10: Picture of FLAMES in GIRAFFE MEDUSA mode. View of the back of one OzPoz plate where all the fibers are attached with magnetic buttons. Credits: ESO.

2.2.2 Methodology

In this section I will describe the methodology and different steps that allowed us to obtain the BSS rotational velocity values.

2.2.2.1 CMD selection of the BSS

In order to obtain stellar spectra, the first step is to select the sample in the CMD. Regarding BSSs, a useful way to do it, is to select the BSS sample in a UV plane (e.g. $m_{F275W} - m_{F336W}$,

m_{F275W} in the HST photometric system). This is extremely useful because BSSs, being hotter than most cluster stars, are brighter than other cluster members at UV wavelengths, and not particularly bright at optical wavelengths, which are mainly dominated by the light from cooler stars (e.g., AGBs and RGBs). This also allows to make a complete selection of BSSs in the GCs, since they are the most crowded environments of the Galaxy. In this way, even stars concentrated in the innermost regions of the cluster can be observed, as they are brighter than the surrounding stars.
Another important criterion adopted is the selection of isolated stars, avoiding possible contamination of the spectra by scattered light from nearby stars. Otherwise, the light of surrounding stars would enter the fiber and contaminating the BSS spectrum. Hence, all the potential targets having stars of comparable or brighter luminosity within a distance of about 3" (which is more than twice the spectroscopic fiber size) have been excluded from the selection.

2.2.2.2 Pre-reduction

After the observations, the first step of the analysis consists in the pre-reduction of the data, e.g. bias subtraction, flat field correction, wavelength calibration and one-dimensional spectra extraction.
The median of the sky spectra secured during the observations has been assumed as master-sky spectrum and used to remove the sky contribution from each individual exposure. Then, for each target the sky-subtracted spectra have been combined, providing the final spectra for the analysis. The combination of multiple exposures is fundamental to reach the SNR required to obtain small uncertainties. In this way, the SNR increases with the square root of the number of exposures. Finally, sky-subtracted combined one-dimensional spectra have been corrected for the heliocentric velocity.

2.2.2.3 Estimation of atmospheric parameters

Atmospheric parameters (e.g. effective temperature T_{eff} and surface gravity *log g*) are fundamental ingredients for the computation of appropriate synthetic spectra to be compared with those observed, from which radial and rotational velocities are then measured. In order to obtain atmospheric parameter values, we performed an isochrone fitting method, that consist in the orthogonally projection of the CMD position of each single star to the closest isochrone. For HB stars, an HB model has been used instead. The models have been retrieved from the online BASTI-IAC database (Pietrinferni et al., 2021), adopting an α-enhanced mixture, and the metallicity and age proper of each cluster. Absolute magnitudes were converted to observed magnitudes using a distance modulus $(m - M)_V$ and reddening $E(B - V)$ proper of each cluster.

2.2.2.4 Cluster membership

The next step in the analysis is to identify the cluster member stars within the sample. Indeed, it is possible that some field interlopers are located in the line of sight of the cluster. Two useful quantities to assess cluster membership are the radial velocity and proper motion.
The radial velocities of the sampled stars have been measured by using the IRAF task *fxcor*, which performs a cross-correlation between the observed spectrum and a template of known radial velocity (Tonry & Davis, 1979). As templates we adopted synthetic spectra computed with the code SYNTHE (Sbordone et al., 2004; Kurucz, 2005) by adopting the last version of the Kurucz/Castelli linelist for atomic and molecular transitions. To take into account the different stellar parameters and line strengths, we defined a template for each evolutionary stage. The model atmospheres have been computed with the ATLAS9 code (Kurucz, 1993; Sbordone et al., 2004) under the assumptions of local thermodynamic equilibrium and plane-parallel geometry, and adopting the new opacity distribution functions by Castelli & Kurucz (2003) with no inclusion of overshooting (Castelli et al., 1997). In all three analyzed clusters, radial velocities prove to be a remarkably efficient diagnostic for membership determination, as the clusters mean radial velocities are clearly distinct from those of the field stars. Stars with radial velocities within 3σ from the median cluster radial velocity have been selected as member stars. In cases where the radial velocity measurement was not sufficiently precise due to high rotational velocities, membership was confirmed by estimating the Gaia Data Release (DR) 3 proper motions (Gaia Collaboration et al., 2016, 2023).

2.2.2.5 Rotational velocity calculation

Finally, after performing the radial velocity correction and estimating the atmospheric parameters, the last step is the calculation of the rotational velocity. Rotational velocities have been measured by comparing the normalized observed spectra with a grid of synthetic spectra calculated with the atmospheric parameters discussed above and with different values of *v sin(i)*. To estimate their uncertainties, we performed a Monte Carlo simulation. In particular, for each star we calculated a synthetic spectrum with the proper atmospheric parameters and the best-fit value of *v sin(i)*. Then, we randomly added Poissonian noise with the same SNR ratio of the observed spectrum and repeated the analysis described above, thus deriving a new best-fit value of *v sin(i)*. By repeating the procedure 300 times, we obtained a distribution of *v sin(i)* values, and finally adopted its standard deviation as the 1σ uncertainty on the rotational velocity of each star.

2.2.3 Thesis layout

This Thesis is structured as follows:

- In Chapter 3, I will present and discuss the main results obtained for a sample of BSSs and reference stars observed with the multi-object spectrograph M2FS at the Magellan Telescope, which belong to the low-concentration GGC NGC 3201, and compare them with results already available in the literature.

- In Chapter 4, I will discuss the rotational velocity and CMD distributions of BSSs and HB stars in M55, a low-concentration GGC observed with FLAMES at the ESO VLT, which stands out as the least concentrated and least dense cluster in the sample, offering a particularly interesting case for study.

- In Chapter 5, I will present the results on the BSS rotational velocity distribution in the GGC NGC 1851, whose intermediate King concentration value makes it a key system connecting low- and high-concentration clusters.

- In Chapter 6, I will discuss the overall results of this Thesis in comparison with those from the other clusters of the survey, emphasizing the main conclusions of the BSS rotational velocity investigation and describe the future perspectives of this work.

CHAPTER 3

Fast rotating Blue Straggler Stars in the Globular Cluster NGC 3201

Based on the results published in:

- *Billi, A., Ferraro, F. R., Mucciarelli, A., Lanzoni B., Cadelano M., Monaco L., Mateo M., Bailey III John I., Reiter M., and Olszewski W., 2023,* ApJ, *956, 2, 124.*

3.1 Introduction

NGC 3201 (see Figure 3.1) is the first cluster analyzed in this Thesis. Table 3.1 summarizes the main physical properties of this cluster.

Table 3.1: General properties of the GGC NGC 3201

RA J2000	154.°403417	*Lanzoni et al. (2026, in preparation)*
Dec J2000	-46.°412472	*Lanzoni et al. (2026, in preparation)*
Mass M	$1.93 \times 10^6\ M_\odot$	Baumgardt & Hilker (2018)
Distance from Sun	4.9 kpc	Harris (1996)
Core radius r_c	1.30'	Harris (1996)
King concentration c	1.29	Harris (1996)
Central luminosity density $log\ \rho_0$	$2.71\ L_\odot\ pc^{-3}$	Harris (1996)
$[Fe/H]$	-1.59 dex	Harris (1996)
A^+_{rh} parameter	0.19	Ferraro et al. (2023b)

Since this cluster has relatively low concentration and density, the results obtained will be extremely valuable for the BSS survey. A previous study Simunovic & Puzia (2014, hereafter SP14) investigated 37 BSSs belonging to this cluster using Inamori Magellan Area Camera &

FIGURE 3.1: Image of the GGC NGC 3201, obtained using Wide Field Imager at ESO La Silla telescope, Chile. Credits: ESO.

Spectrograph at the Baade Magellan Telescope, at a spectral resolution $R = 10,000$. Since the dataset of this Thesis is almost doubled and the resolution is much higher, the results obtained in this work are more reliable than those presented in SP14. This chapter is devoted to the detailed presentation of the analysis of 67 BSSs and 114 reference stars (e.g. SGB, TO, RGB and AGB) observed in NGC 3201. This is the second most populated BSS sample in the entire survey, after that of ω Centauri.

3.2 Observations

This work is based on stellar spectra acquired with the multi-object spectrograph M2FS (Mateo et al., 2012) mounted on the Clay Magellan Telescope, located at Las Campanas Observatory, Chile (see Section 2.2.1 for the instrumental description). The observations have been performed during two nights (on 2019, February 28 and March 2), adopting the Mgb_{Revb} configuration, which covers the spectral region between 5127 Å and 5184 Å, sampling the first two lines of the Mg triplet (at 5167.3 Å and 5172.6 Å) with a spectral resolution $R \sim 18,000$. Two different fiber configurations have been adopted to secure spectra for approximately 200 targets in the cluster direction. A total of 6 exposures of 30 minutes each, and 10 exposures of 20 minutes have been secured in the first and second night, respectively.

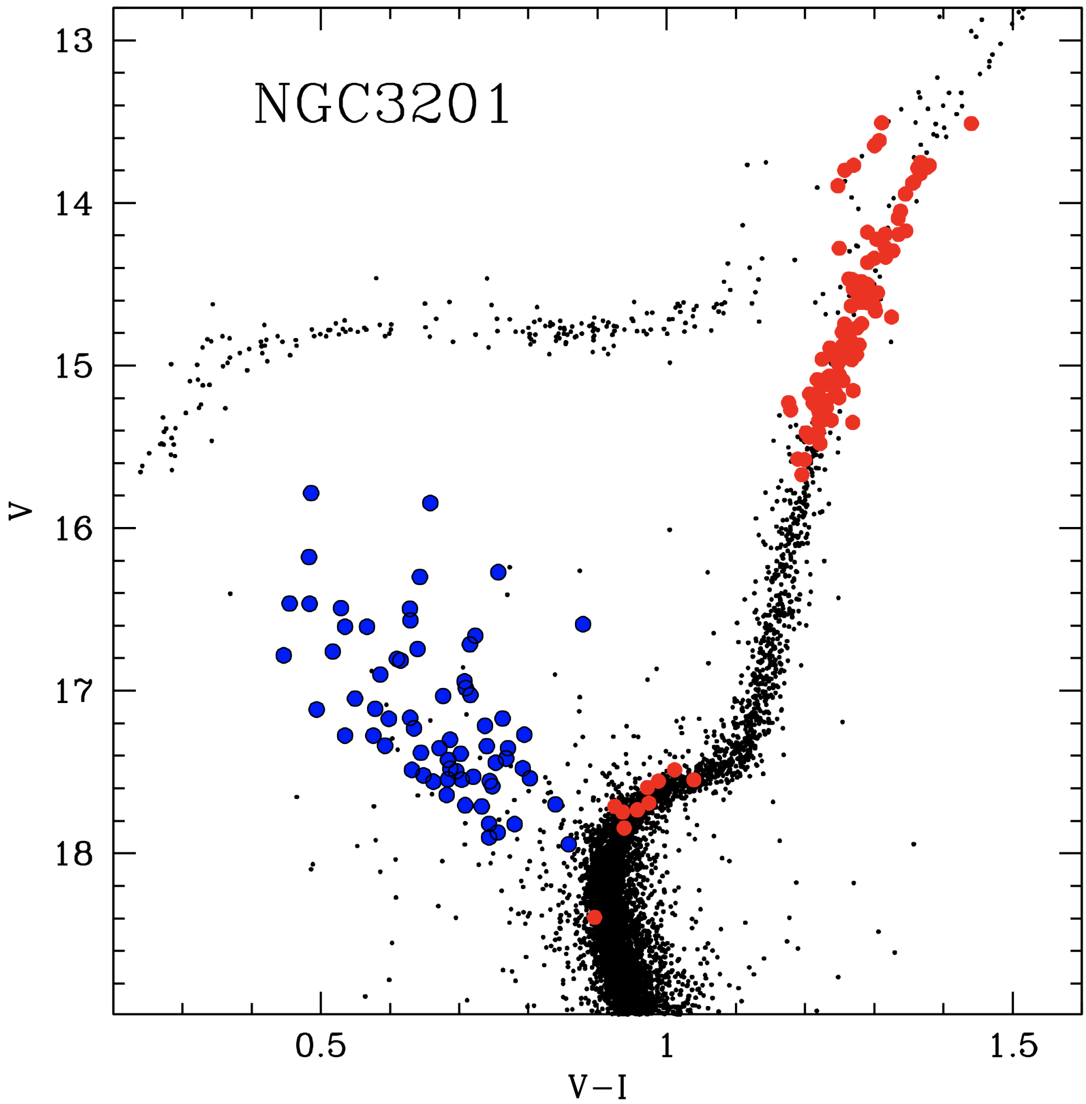

FIGURE 3.2: Proper motion selected and differential reddening corrected CMD of NGC 3201 (black dots), with the spectroscopic targets discussed in the paper highlighted as filled colored circles: the 67 BSSs are marked in blue, while the reference sample of MS, SGB, RGB and AGB stars are plotted in red.

For a proper comparison with SP14, particular care has been devoted to include in the sample most of the BSSs observed in that work (29 out 37). In addition, to compare the BSS rotational velocities with those of "normal" cluster stars, we simultaneously observed a significant sample of reference objects distributed in different evolutionary stages. Due to the high value of the seeing (larger than 1.50″), 2 and 3 exposures from the first and the second night, respectively, have been excluded from the analysis. As a result, we secured spectra of 67 BSSs, 9 SGB stars, one MS star, 98 RGB stars, and 6 AGB stars. Figure 3.2 shows the position of the observed sample in the proper motion selected and differential reddening corrected CMD of NGC 3201, obtained from the photometric catalog of the Stetson database (Stetson et al., 2019) by applying the method described in Cadelano et al. (2020, see also Deras et al., 2023).

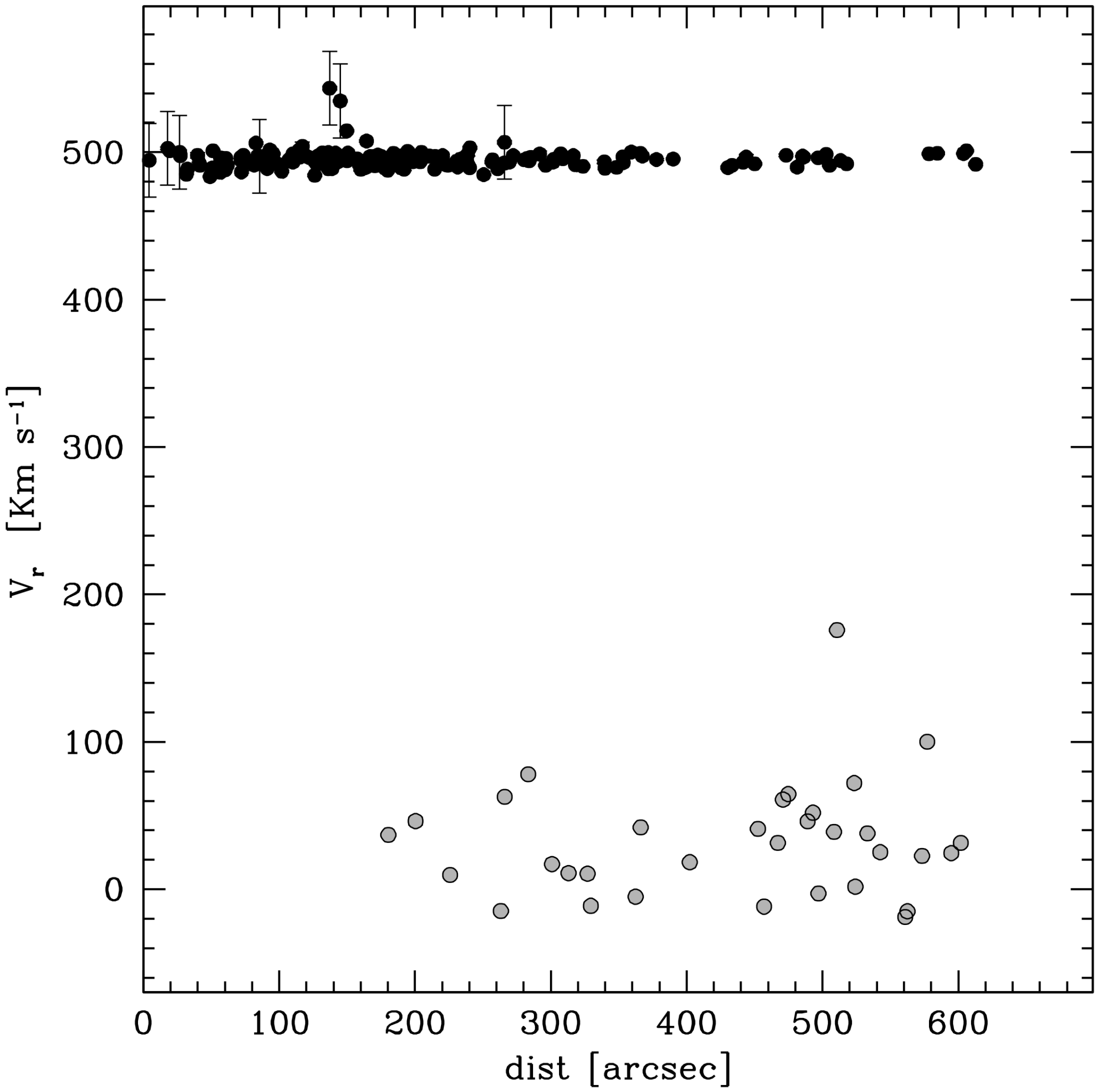

FIGURE 3.3: Radial velocities (in km s^{-1}) of the target stars as a function of their distance from the cluster center (in arcseconds). The stars belonging to NGC 3201 are shown as black circles, while the objects belonging to the Galactic field are colored in gray.

3.3 Radial velocities and cluster membership

Radial velocities have been measured using the methodology discussed in Section 2.2.2.4. Radial velocity values of BSSs are reported in Table 3.2. Figure 3.3 shows the distribution of the measured radial velocities as a function of the distance from the cluster center. Here we adopt the center of gravity obtained by B. Lanzoni et al. (2026, in preparation): α_{J2000} = $10^h17^m36.82^s$, δ_{J2000} = $-46°24'44''.9$. The acquired dataset extends from $r = 4''$, out to $\sim$ $630''$. The cluster population (black circles) is clearly distinguishable as a narrow component strongly peaked at the large systemic velocity of the cluster: $V_{\rm sys} = 494.5 \pm 0.5$ km s^{-1} (Ferraro et al., 2018b). This allows a straightforward identification of the few field stars included in the observed sample, which show much smaller radial velocities (gray circles in Figure 3.3). The few cluster members showing radial velocities larger than the average are rapidly rotating BSSs for which the measures are more uncertain because of the significant deformation of the absorption lines (see Section 3.5).

3.4 Atmospheric parameters

As discussed in Section 2.2.2.3, a set of $\alpha-$enhanced BASTI isochrones, computed by assuming the cluster metallicity ([Fe/H]= -1.59 dex; Harris, 1996), and ages ranging between 1 and 9 Gyr has been retrieved from the online tool BASTI-IAC (Pietrinferni et al., 2021) in order to obtain the effective temperature and surface gravity. The models have been reported to the observed CMD (see blue lines in Figure 3.4) by adopting an apparent distance modulus $(m - M)_V = 14.20$ and a color excess $E(B - V) = 0.27$, in agreement with Harris (1996). As is apparent from the figure, the grid of isochrones properly samples the portion of the CMD where BSSs are distributed. The resulting effective temperatures vary between 6700 and 8700 K, while *log g* ranges between 3.6 and 4.3 dex. An analogous procedure, but using the 12 Gyr old isochrone, has been performed for the reference stars. It is worth emphasizing that these photometric estimates of temperature and gravity are accurate enough to guarantee a solid determination of the rotational velocity. In fact, the impact of these two parameters on the measured rotation is modest. For instance, even large variations in temperature and gravity ($\pm 300 - 500$ K in T_{eff} and $\pm$ 0.8 dex in $log\ g$) produce a small effect ($\sim$ 1 km s^{-1}) in the measured value of *v sin(i)*. In addition, we assumed a microturbulence velocity of 1 km s^{-1} for the BSSs, and 1.5 km s^{-1} for the giant stars, although different assumptions for this parameter have no impact on the rotational velocity values.

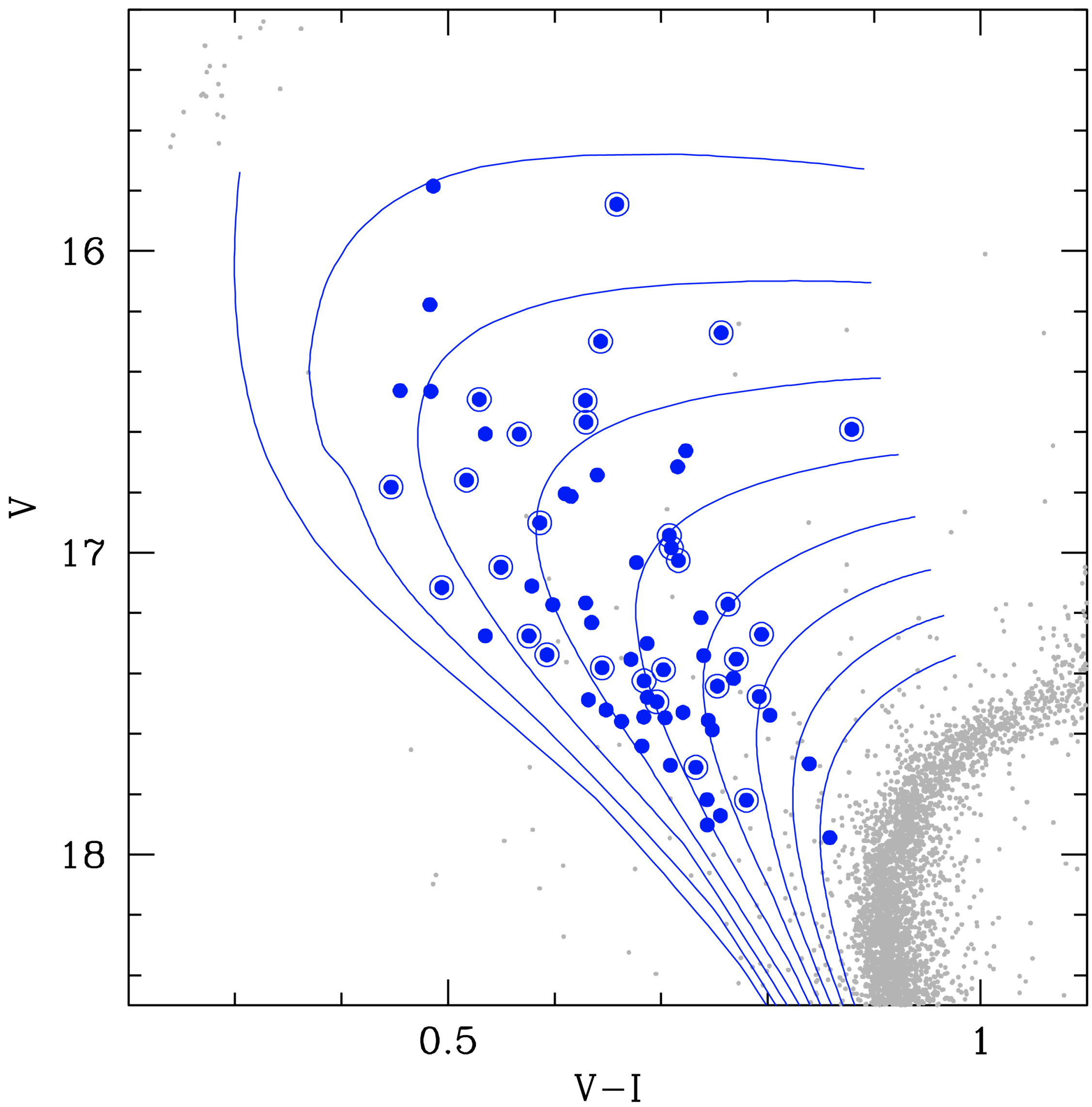

FIGURE 3.4: CMD of NGC 3201 (gray dots) with the 67 surveyed BSSs marked as blue circles, and a set of BASTI isochrones (Pietrinferni et al., 2021) with ages ranging from 1 to 9 Gyr overplotted as blue lines. The BSSs in common with SP14 are encircled.

3.5 Rotational velocities

The rotational velocity has been measured from the first two lines of the Mg triplet at 5167.3 and 5172.6 Å using the χ^2 minimization method described in Section 2.2.2.5. These two features are strong enough to allow an accurate measurement of *v sin(i)* also in the case of very large rotations (of the order of 100 km s^{-1}). For the sake of illustration, Figure 3.5 shows the comparison between the observed and the synthetic spectra of four stars with different rotational velocities for the line at 5172.6 Å. As can be seen, the absorption line is still clearly

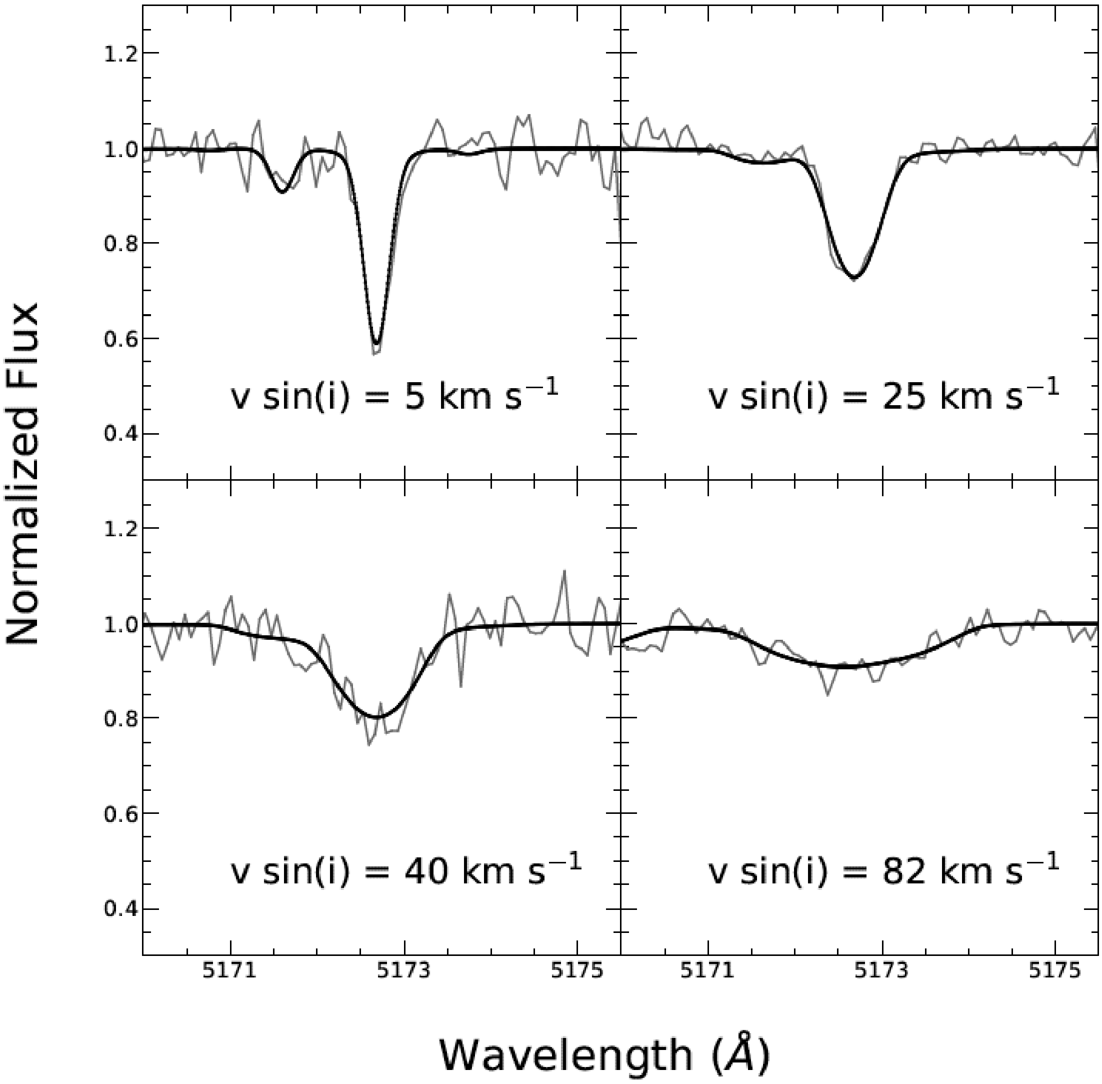

FIGURE 3.5: Comparison between the observed spectra (gray lines) and the best-fit synthetic spectra (black lines) for 4 BSSs with different rotational velocities, ranging from 5 to 82 km s^{-1}.

visible also in the star rotating at more than 80 km s^{-1}.

The estimated uncertainties range from a few (2-5) km s^{-1} for slowly rotating stars, up to 15-20 km s^{-1} for the fast spinning targets (with rotation of the order of, or larger than, 100 km s^{-1}).

As shown in Figure 3.6, the distributions of rotational velocities obtained for the observed samples of BSSs and normal cluster stars are strikingly different. Almost all the highly evolved stars (RGB and AGB targets), all the SGB stars and the MS star in the sample show negligible rotation ($v\ sin(i)\ <\ 10$ km s^{-1}), in agreement with the rotational velocities quoted in the literature for cluster and field stars in similar evolutionary stages (see, e.g., Lucatello & Gratton, 2003; Cortés et al., 2009; De Medeiros et al., 2014). Indeed only one RGB star has

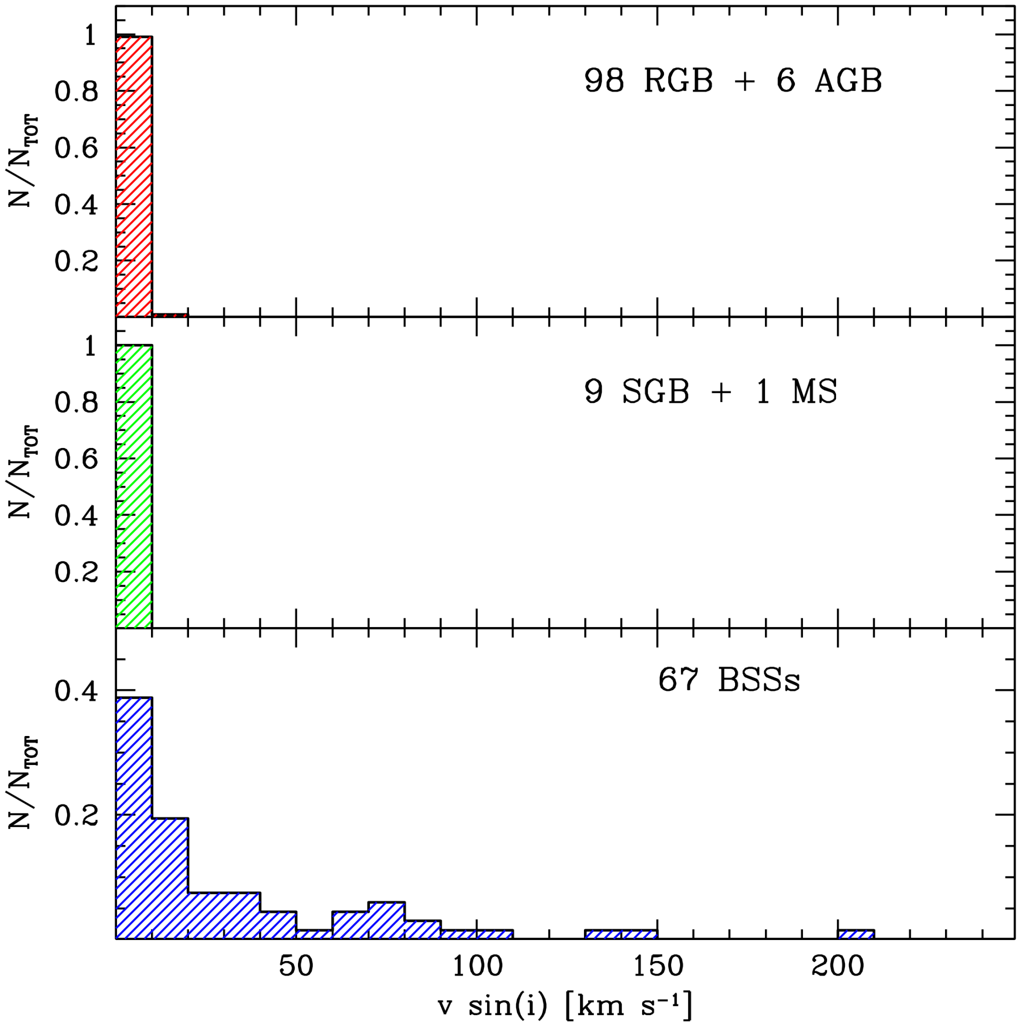

FIGURE 3.6: Distributions of the rotational velocities measured for highly-evolved, giant stars (red histogram in the upper panel), mildly-evolved (SGB and MS) stars (green histogram in the central panel), and BSSs (blue histogram in the bottom panel).

a rotation of 12 km s^{-1}, which could be due to an interaction with a companion object (unfortunately our dataset is not suitable to search for radial velocity variability, but this object is certainly worth of further investigations). Conversely, the distribution of BSS rotational velocities appears to be much more articulated, with a peak at low values followed by a long tail extending up to very large rotations (up to 207 km s^{-1}). Moreover, only less than 40% of the entire sample shows rotational velocities below 10 km s^{-1}, while 19 BSSs of our 67 ($\sim$ 28% of the total) spin faster than 40 km s^{-1} and are classified as FR-BSSs. Hence, this comparison clearly demonstrates that BSSs display a very peculiar rotational velocity distribution with respect to normal clusters stars. Table 3.2 reports rotational velocity values of BSSs with their uncertainties.

TABLE 3.2: Identification number, coordinates, V-band magnitude and (V−I) color (from Stetson et al., 2019), radial velocity and rotational velocity of the analyzed BSSs.

ID	R.A. [deg]	Decl. [deg]	V	(V−I)	V_r [km s^{-1}]	$v\ sin(i)$ [km s^{-1}]
1017509	154.3594693	-46.4223802	15.86	0.66	496.6 ± 2.3	70 ± 5
2717877	154.3609053	-46.3881454	15.86	0.52	543.4 ± 1.1	207 ± 13
2718774	154.3527168	-46.4121898	16.19	0.49	495.1 ± 3.0	62 ± 6
1012904	154.4019237	-46.4198272	16.23	0.74	500.0 ± 1.6	137 ± 12
1010831	154.4189046	-46.4216023	16.34	0.66	489.2 ± 1.2	25 ± 2
2714632	154.3860264	-46.4501061	16.43	0.44	495.4 ± 1.0	9 ± 1
2201178	154.4372466	-46.2438790	16.44	0.48	491.8 ± 1.0	5 ± 2
2720497	154.3341108	-46.4439012	16.49	0.60	496.4 ± 1.0	35 ± 4
2602689	154.2683715	-46.3318255	16.50	0.63	496.7 ± 1.9	41 ± 4
1006762	154.3834415	-46.4321004	16.60	0.88	495.6 ± 0.2	5 ± 1
2705123	154.4507866	-46.4315920	16.61	0.67	499.8 ± 0.8	15 ± 1
2715664	154.3784331	-46.3332489	16.62	0.54	498.8 ± 2.1	80 ± 8
2702518	154.4824695	-46.3775296	16.63	0.59	495.3 ± 0.7	10 ± 1
1009269	154.4330228	-46.4137157	16.64	0.58	495.7 ± 0.8	14 ± 2
1031149	154.4004033	-46.3970078	16.69	0.73	492.1 ± 0.4	5 ± 1
2713191	154.3951283	-46.3726009	16.71	0.63	534.8 ± 0.6	82 ± 5
1012746	154.4033625	-46.4136813	16.77	0.52	494.6 ± 0.8	89 ± 8
2711800	154.4035545	-46.4540524	16.79	0.61	514.5 ± 0.6	80 ± 7
2301092	154.2432987	-46.2935999	16.85	0.60	499.3 ± 0.9	17 ± 3
1025619	154.3816172	-46.4041477	16.86	0.63	491.2 ± 0.6	5 ± 1
2717902	154.3607599	-46.3985450	16.89	0.49	504.1 ± 2.7	50 ± 6
1022302	154.4098273	-46.4102006	16.93	0.60	502.7 ± 1.0	149 ± 15
1009786	154.4276377	-46.4137044	16.95	0.71	488.1 ± 0.5	16 ± 3
1005074	154.4006768	-46.4278998	17.04	0.72	490.7 ± 1.8	40 ± 4
1032796	154.3836383	-46.3943513	17.07	0.58	491.3 ± 1.3	70 ± 8
2704041	154.4626969	-46.4327815	17.08	0.75	507.6 ± 0.7	13 ± 2
1006473	154.3864661	-46.4382688	17.14	0.50	487.0 ± 0.8	56 ± 6
2714772	154.3851443	-46.4635956	17.15	0.60	489.5 ± 2.1	45 ± 6
1021152	154.4195717	-46.4093147	17.17	0.60	491.2 ± 0.6	9 ± 1
2716018	154.3760880	-46.4361699	17.19	0.61	496.4 ± 0.6	10 ± 3
2600533	154.3140993	-46.3867423	17.19	0.61	503.0 ± 0.8	5 ± 2
2714749	154.3855481	-46.5545236	17.20	0.50	494.3 ± 0.6	5 ± 2
1020369	154.4272846	-46.4087656	17.20	0.73	496.1 ± 0.9	5 ± 1
1016643	154.3700469	-46.4114471	17.22	0.78	506.2 ± 0.6	9 ± 3

Continue...

ID	R.A. [deg]	Decl. [deg]	V	(V−I)	V_r [km s^{-1}]	$v\ sin(i)$ [km s^{-1}]
2707141	154.4338850	-46.3495438	17.25	0.56	498.6 ± 1.1	26 ± 2
2711836	154.4034550	-46.4747336	17.25	0.70	491.2 ± 0.5	5 ± 2
1014355	154.3911378	-46.4196159	17.27	0.67	497.9 ± 1.8	74 ± 7
1013700	154.3962520	-46.4182565	17.27	0.79	498.2 ± 0.5	12 ± 2
2713289	154.3947502	-46.4416678	17.30	0.58	494.8 ± 1.0	35 ± 4
2603838	154.2324762	-46.3496011	17.36	0.73	489.9 ± 0.6	13 ± 2
2710692	154.4103191	-46.4691207	17.36	0.75	500.0 ± 0.6	5 ± 2
1035238	154.3842813	-46.3772396	17.38	0.65	494.9 ± 0.5	5 ± 2
1021331	154.4184729	-46.4027317	17.39	0.79	501.0 ± 0.2	5 ± 1
2708408	154.4249930	-46.3192117	17.42	0.67	489.2 ± 1.1	27 ± 3
1008650	154.4390510	-46.4182480	17.45	0.73	492.5 ± 0.7	15 ± 2
2601851	154.2893054	-46.4032201	17.46	0.67	496.5 ± 0.4	5 ± 1
1030901	154.4032020	-46.3843063	17.47	0.70	491.3 ± 1.9	36 ± 4
2705144	154.4505614	-46.4256266	17.47	0.72	484.3 ± 0.9	80 ± 7
2712276	154.4003359	-46.3386111	17.48	0.63	506.8 ± 1.1	103 ± 12
2714006	154.3898416	-46.3689811	17.51	0.67	488.4 ± 1.1	17 ± 3
1023539	154.3993515	-46.4078560	17.54	0.65	501.1 ± 0.6	5 ± 2
2705506	154.4472108	-46.3887971	17.54	0.82	489.1 ± 0.4	6 ± 2
2201091	154.4436556	-46.2464918	17.54	0.74	501.0 ± 0.5	0 ± 3
1019708	154.4337343	-46.4011820	17.57	0.73	497.3 ± 0.9	100 ± 10
1031222	154.3994121	-46.3927124	17.58	0.67	496.5 ± 0.7	16 ± 3
1025211	154.3849299	-46.4076830	17.58	0.74	483.5 ± 0.4	13 ± 2
2709841	154.4152943	-46.3652141	17.59	0.66	498.1 ± 1.6	25 ± 3
2717413	154.3656112	-46.5290841	17.59	0.66	489.6 ± 0.9	18 ± 3
1002749	154.4246075	-46.4282995	17.60	0.81	493.1 ± 0.4	5 ± 2
2801544	154.6364229	-46.4157168	17.64	0.77	498.9 ± 0.3	5 ± 2
2603587	154.2407347	-46.4623012	17.65	0.68	493.1 ± 0.6	0 ± 2
2602084	154.2836336	-46.3533481	17.71	0.69	499.3 ± 0.4	23 ± 5
2711709	154.4041397	-46.4461522	17.74	0.86	496.7 ± 0.6	5 ± 2
1026151	154.3766105	-46.4000632	17.77	0.76	493.1 ± 0.3	5 ± 2
1016923	154.3668729	-46.4150062	17.82	0.78	489.0 ± 0.8	20 ± 2
2601312	154.3002520	-46.4078210	17.83	0.72	493.5 ± 1.0	33 ± 4
2717272	154.3667567	-46.4837663	17.85	0.82	497.7 ± 0.3	5 ± 2

3.6 Comparison with SP14

As mentioned in Section 3.1, SP14 determined the rotational velocities of 37 BSSs in NGC 3201 (plus other BSSs in ω Centauri and NGC 6218) from the analysis of spectra acquired with the Inamori Magellan Area Camera & Spectrograph at the Baade Magellan Telescope, at a spectral resolution $R = 10,000$. The rotational velocity distribution derived by these authors is different from that plotted in Figure 3.6: it shows a peak at 25-30 km s^{-1}, which is not visible in our distribution, and only 6 stars ($\sim$ 19% of the total sample) spin faster than 40 km s^{-1}. Since we have 29 BSSs in common with SP14, we can perform a proper star-to-star comparison to understand the origin of the discrepancy.

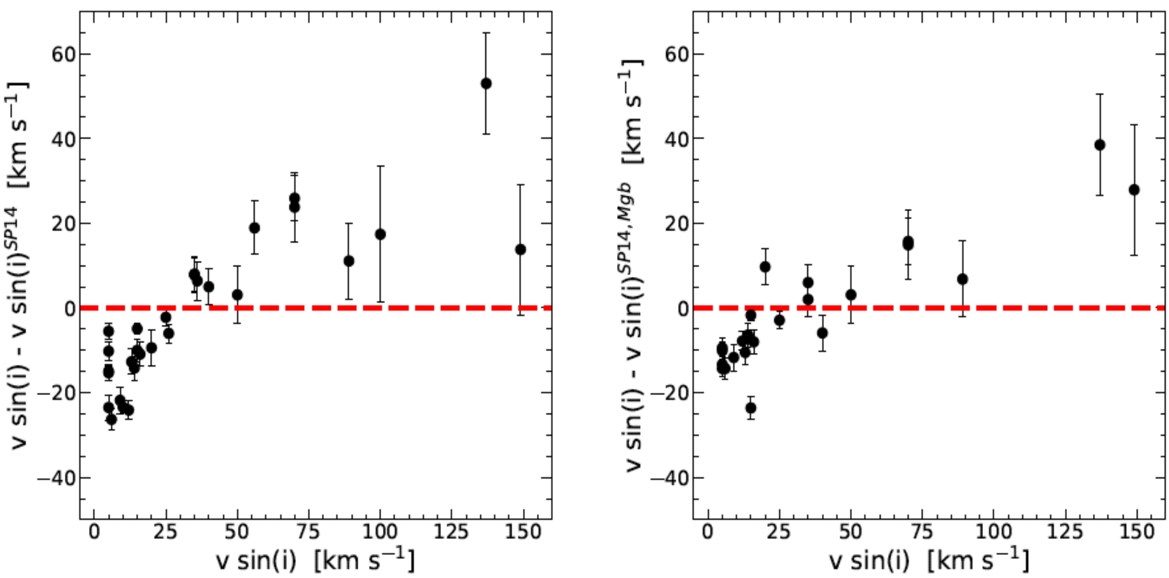

FIGURE 3.7: *Left panel:* Difference between the rotational velocities obtained in this work ($v\ sin(i)$) and those determined by SP14 ($v\ sin(i)^{\rm SP14}$) for the 29 BSSs in common, as a function of our measures. *Right panel:* as in the left panel, but for the rotational velocities of SP14 computed from the Mgb triplet line alone ($v\ sin(i)^{\rm SP14,Mgb}$).

Figure 3.7 shows the difference between the rotational velocities determined in this work and in SP14, as a function of our measures, for the 29 BSSs in common. As apparent, all the stars for which we find $v\ sin(i) < 30$ km s^{-1} have larger rotation in SP14 (in some extreme cases they are in excess by even ~ 25 km s^{-1}), while the opposite is true for most of the FR-BSSs. This trend is very similar to that found by Mucciarelli et al. (2014) in the case of ω Centauri (see their Figure 6), from the comparison between the measurements of SP14 and those obtained from higher resolution ($R > 18,000$) spectra acquired with FLAMES at the ESO-VLT for 14 BSSs in common. Also taking into account that the spectral resolution used in the present work and in Mucciarelli et al. (2014) is approximately the same and about twice that of SP14, we conclude that the origin of the discrepancies observed in NGC 3201 (Figure 3.7) and in ω Centauri (Figure 6 in Mucciarelli et al., 2014) is the same. The disagreement detected at low rotational velocities can be ascribed to the lower spectral resolution used in SP14, which naturally makes much more difficult the measure of small rotation values because the line profile is dominated by the instrumental broadening, instead of the rotational broadening.

The difference in the high velocity regime is mainly ascribable to the different absorption lines used in the SP14 analysis. In fact, in addition to the Mgb triplet, these authors also used the Balmer lines and the MgII 4481 line. The Balmer lines, however, are only marginally sensitive to rotation. In fact, as shown in Figure 8 of Mucciarelli et al. (2014), a change of rotational velocity from 0 to 200 km s^{-1} produces no significant variations in the line wing morphology and the full width at half maximum of the Balmer lines. The Mgb triplet lines are by far more sensitive to rotation than the Balmer ones, and the estimates they provide are therefore significantly more precise. This is also confirmed by the fact that the difference between the rotational velocities measured by SP14 from the Mgb triplet alone and the values determined in this work is reduced: the dispersion of the data with respect to zero decreases from $\sigma = 8.7$ to $\sigma = 6.4$ (see Figure 3.7). Indeed, by using the rotational velocities measured from the Mgb diagnostic alone, the fraction of FR-BSSs in the SP14 sample amounts to $\sim 20 - 25\%$ of the total, which is not that different from what we obtained here ($\sim 28\%$).

3.7 Results and discussion

As discussed in Section 2.1, the BSSs analyzed in this work were part of the spectroscopic survey that aim to study chemical and rotational properties of a representative sample of BSSs in a sample of GCs with different structural parameters values. Figure 3.8 shows the percentage of FR-BSSs of the six cluster already published and of this cluster as a function of the King concentration. The position of NGC 3201 is highlighted in blue. As can be seen, the percentage of FRs in NGC 3201 is fully compatible with that of the other low-concentrated clusters in the sample (namely, ω Centauri, and M4), while it is significantly larger than that measured in the four high-concentrated systems (namely, 47 Tucanae, M30, NGC 6752 and NGC 6397). This result will be discussed in more detail in Chapter 6.

Additional information can be obtained from the analysis of the CMD and radial distributions of the observed stars. The top-left panel of Figure 3.9 shows the CMD of NGC 3201 zoomed in the BSS region, with the slow rotators marked as small blue circles, and the FRs plotted as red circles of increasing size for increasing rotational velocity.

As is apparent from the figure, fast and slowly spinning BSSs are not homogeneously mixed

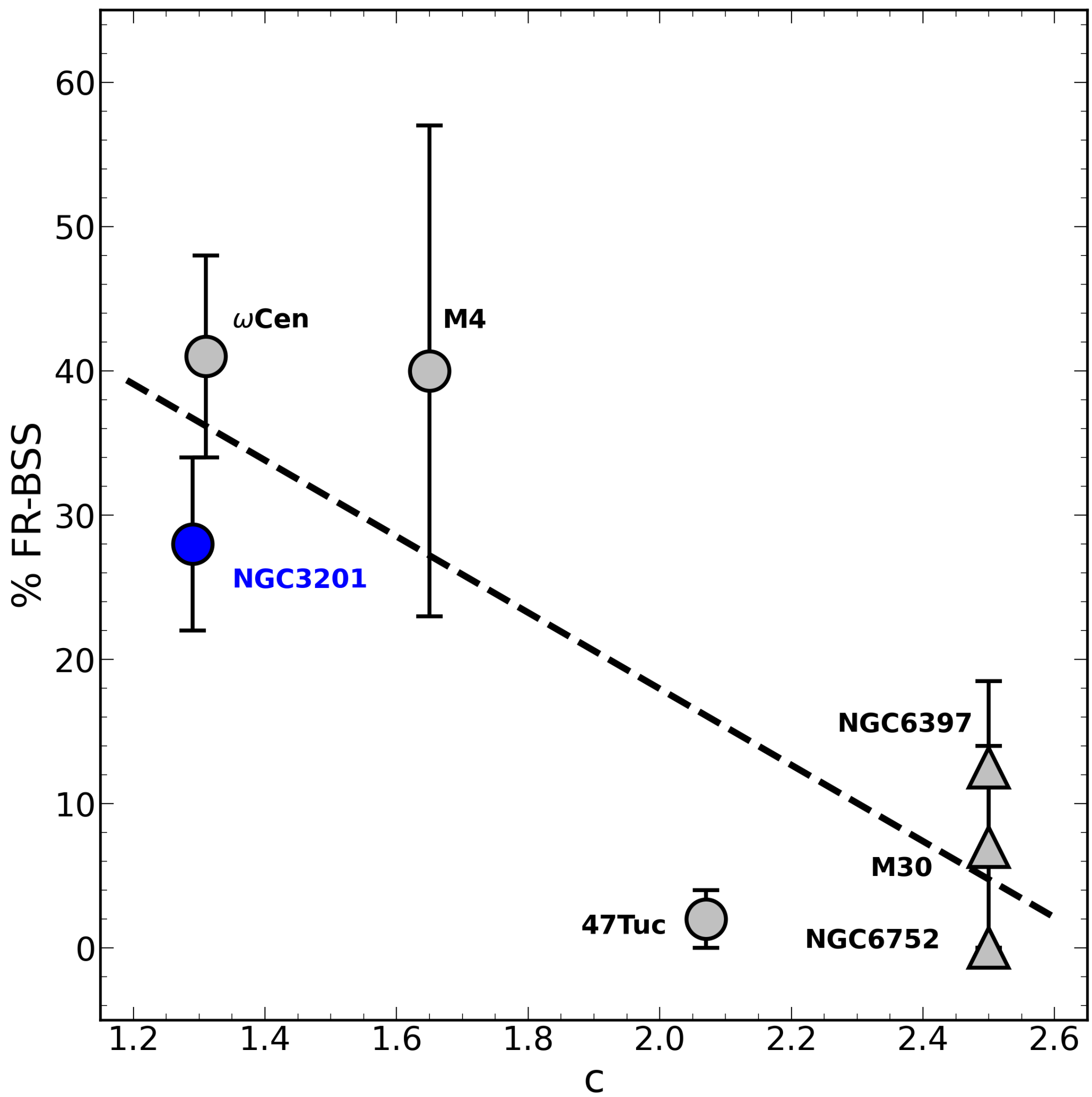

FIGURE 3.8: Percentage of FRs (i.e., number of BSSs with $v\ sin(i) \geq 40\ km\ s^{-1}$ over the total number of surveyed BSSs) as a function of the King concentration of the parent cluster, for NGC 3201 (blue circle) and the other GCs (namely, ω Centauri, M4, 47 Tucanae, M30, NGC 6752, and NGC 6397; gray circles).

in the CMD: FR-BSSs tend to be preferentially located in the upper-left side of the BSS sequence, while the region closer to the MS-TO is populated by slow rotators only. This suggests the existence of a trend between the rotational velocity and the BSS luminosity and color (temperature) that is worth to be further investigated.

The dependence of *v sin(i)* on the stellar color is shown in the upper-right panel of Figure 3.9. Although the statistics is small, not a single FR-BSSs is observed at $(V - I) > 0.75$, and a hint of decreasing rotational velocity for increasing color (i.e., decreasing surface temperature) can also be recognized. The tendency for FR-BSSs to preferentially have bluer colors

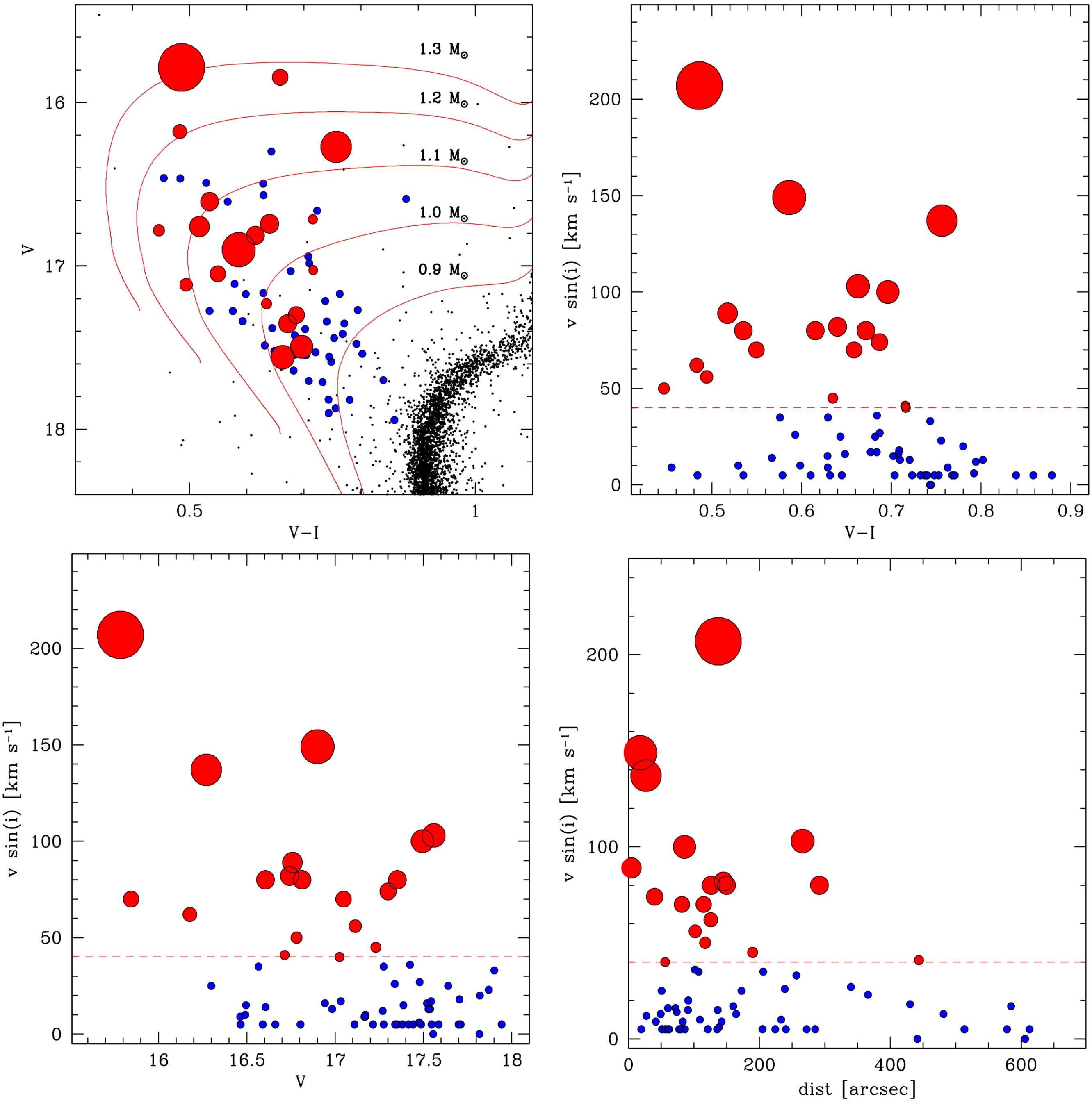

FIGURE 3.9: From top-left, to bottom-right: distribution of the surveyed BSSs in the CMD of NGC 3201, and rotational velocity distributions as a function of the $(V-I)$ color, the V magnitude, and the distance from the cluster center. In all the panels, the FRs are plotted as red circles with increasing size for increasing rotational velocity, while the BSSs spinning at $v\,\sin(i) < 40$ km s^{-1} are marked as small blue circles. A set of single-mass evolutionary tracks (Pietrinferni et al., 2021) for stars between 0.9 and 1.3 $M_{\odot}$ are also overplotted as red lines in the top-left panel.

than slowly spinning BSSs is also confirmed by the cumulative color distributions of the two

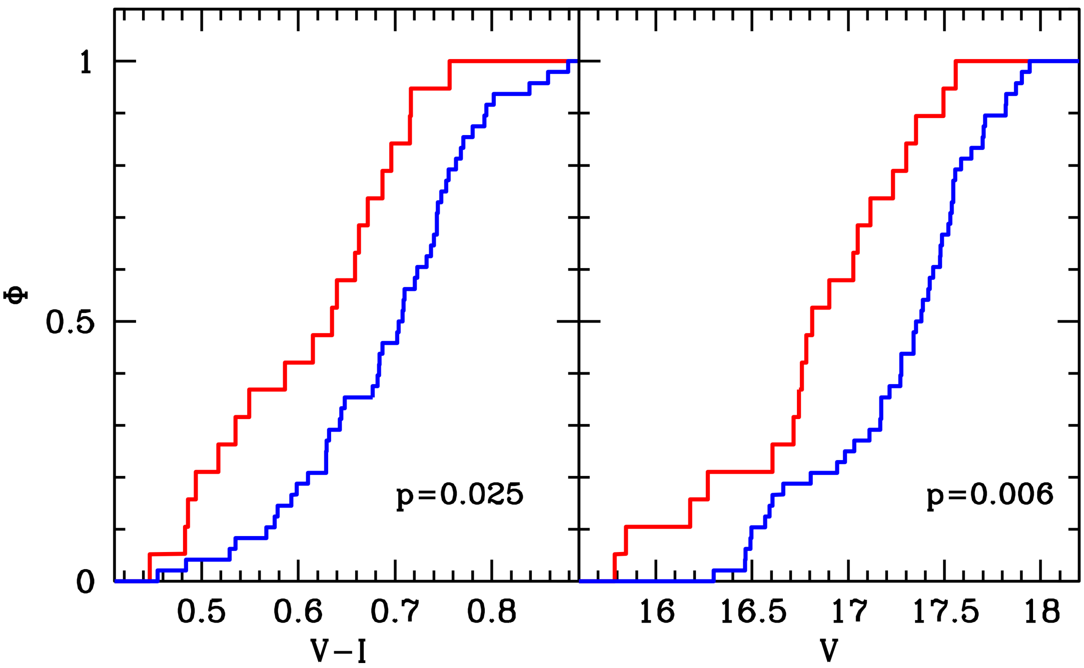

FIGURE 3.10: Cumulative distributions of the $(V-I)$ color (left panel) and V magnitude (right panel) for the sample of FRs (i.e., BSSs with $v\ sin(i) \geq 40\ km\ s^{-1}$; red lines) and slow rotators (blue lines). The Kolmogorov-Smirnov (KS) probability to be extracted from the same parent distribution p is marked in each panel. Note that the statistical significance of the KS test is somehow overestimated in this case due to the need of introducing a free parameter (namely the 40 $km\ s^{-1}$ threshold).

samples that is shown in the left panel of Figure 3.10. The significance of the detected difference is not very high (of the order of 2.2σ). However the same signal seems to emerge (even more clearly) with the magnitude. In fact the inspection of the bottom-left panel of Figure 3.9 shows a tendency for the most luminous BSSs to be the faster rotators, and no slowly spinning BSSs are observed at the brightest magnitudes. Although the statistics is relatively poor, the comparison between the cumulative luminosity functions of the fast and slow rotator samples (Figure 3.10) seems to confirm this trend.

Thus a general tendency to find fast spinning BSS at higher luminosity and at bluer colors (higher temperatures) is emerging from this study. The observed trend might also be read in terms of stellar mass (see the set of single-star evolutionary tracks overplotted as red lines in the upper-left panel of Figure 3.9). Indeed, it is generally accepted that more luminous BSSs are more massive than their lower luminosity sisters. Although caution must be used in deriving BSS masses from their luminosity distribution (e.g., Geller & Mathieu, 2011), a reasonable agreement has been found (Raso et al., 2019) between the mass derived from fitting the spectral energy distribution, and that obtained from the comparison of the BSS location

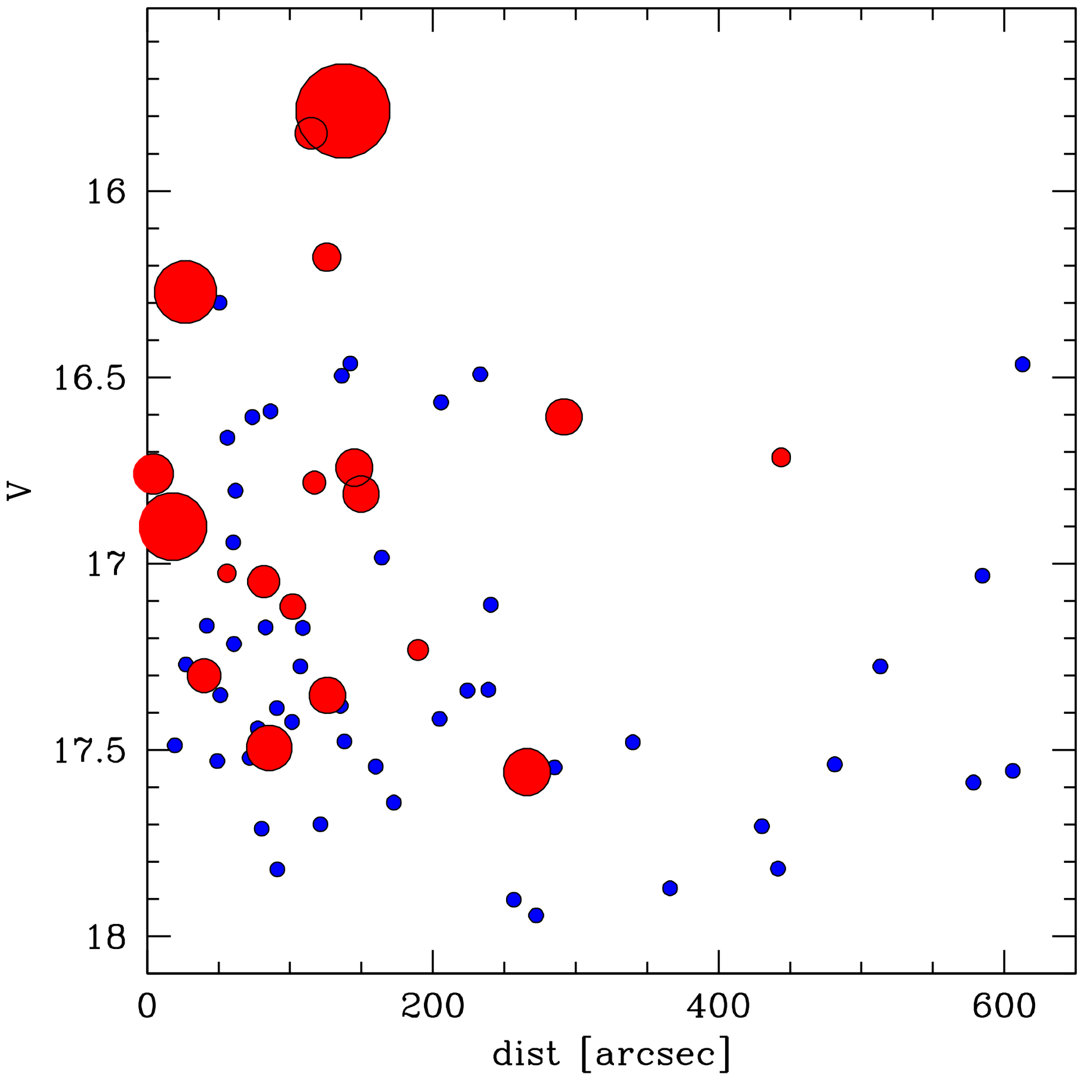

FIGURE 3.11: Distribution of magnitude as a function of the distance from the cluster center (in arcseconds) for the observed sample of BSSs. Symbols have the same meaning of Figure 3.9.

in the CMD with single-star evolutionary tracks. Such a connection between mass and luminosity is also confirmed by the observed radial distribution (see the bottom-right panel of Figure 3.9 and Figure 3.11): highly spinning BSSs (corresponding to the brighter, more massive, objects) are not found in the external regions of the cluster and tend to be preferentially located toward the center. This is consistent with an effect of mass segregation. Indeed, according to the value of the A^+_{rh} parameter (Ferraro et al., 2023a), NGC 3201 has an intermediate dynamical age, thus implying that dynamical friction is currently effective in making the heavier stars sinking toward the cluster center starting from the most massive ones (notably, 13 out of 19 FRs, i.e. almost $\sim 70\%$ of the total, appear to be more massive than 1 $M_\odot$ according to the evolutionary tracks shown in the upper-left panel of Figure 3.9).

How can the observed trend between rotational velocity and temperature (mass) be interpreted? Indeed, a decrease of rotational velocity for decreasing surface temperature has been observed also in the BSS population of the OC NGC 188 (Mathieu & Geller, 2009). Under the hypothesis that BSS rapid rotation in low-density environments is due to mass transfer, followed by a braking timescale of the order 1-2 Gyr, the rapid rotation of more massive BSSs in NGC 3201 may indicate that the most recent BSS formation activity preferentially involved more massive primordial binaries. Alternatively, it is worth noticing that normal MS stars show a similar trend, with an increasing rotation in higher-temperature objects ($V - I < 0.6$) that is attributed to their reduced convective envelopes, leading to much lengthened spin-down times (see, e.g., Kraft, 1967; van Saders & Pinsonneault, 2013). Hence, a similar process could be active also in the interior of BSSs, and this would be consistent with the hypothesis that most of these stars in NGC 3201 are generated from the evolution of binary systems: in fact, no convective envelope is predicted to develop in collisional products (Sills et al., 2005). Although the internal structure of BSSs is still poorly constrained, the connection of rotation with mass and temperature might be a useful clue for improved BSS models.

In conclusion, the statistical significance of the discussed trends is admittedly low, and many crucial pieces of information are still missing (including information about the binarity of these systems and their possible tidal synchronization; for recent results in the field and OCs, see, e.g., Lurie et al., 2017; Leiner et al., 2019, and references therein). However, the results presented in this work can be considered as the starting point for future observational campaigns and possible clues for improved theoretical models aimed at properly describing the physical properties of these puzzling stars, and the role that the host environment can play in setting them.

CHAPTER 4

Rotational velocities of blue straggler stars in the globular cluster M55

Based on the results published in:

- *Billi, A., Ferraro, F. R., Mucciarelli, A., Lanzoni B., Cadelano M., and Monaco L.,* 2024, A&A, *690, A156.*

4.1 Introduction

M55 (see Figure 4.1) is the second cluster analyzed in this Thesis. Table 4.1 reports the main physical properties of the GGC M55.

TABLE 4.1: General properties of the GGC M55

RA J2000	294°.99878	(Baumgardt & Hilker, 2018)
Dec J2000	-30°.96475	(Baumgardt & Hilker, 2018)
Mass M	$1.97 \times 10^5\ M_\odot$	(Baumgardt & Hilker, 2018)
Distance from Sun	5.4 kpc	(Harris, 1996)
Core radius r_c	1.80’	(Harris, 1996)
King concentration c	0.93	(Harris, 1996)
Central luminosity density $log\ \rho_0$	$2.22\ L_\odot\ pc^{-3}$	(Harris, 1996)
$[Fe/H]$	-1.94 dex	(Harris, 1996)
A^+_{rh} parameter	0.10	(Lanzoni et al., 2016)

Among the clusters of the survey, M55 has the lowest values of central density and King concentration. Hence, it is a fundamental result that allows us to broaden the range of structural parameters in the survey. This chapter is devoted to the detailed presentation and discussion of the analysis of 32 BSSs and 76 reference stars (e.g. HB and RGB) observed in this low-density cluster.

FIGURE 4.1: Image of the GGC M55, obtained using the 3.6-meter telescope at ESO La Silla, Chile. Credits: ESO.

4.2 Observations

This work is based on high resolution stellar spectra acquired with the multi-object spectrograph FLAMES-GIRAFFE (Pasquini et al., 2002) mounted at the VLT of ESO under program 093.D-0270 (PI: Lovisi). All spectra have been acquired with the HR2 grating, with a spectral resolution R = 22,700 in the wavelength range $\Delta\lambda = 3854 - 4049$ Å, in order to sample the Ca II K line at the wavelength $\lambda = 3933.6$ Å, which is very sensitive to the rotation of stars at high temperature (BSS and HB). For RGBs, we used different lines of Fe and Ti. A total of 16 exposures of 2760 seconds each have been secured. The observations have been performed in nine nights between June and July 2014. Six exposures had bad sky conditions (moon distance and airmass) so we excluded them from the analysis. The spectra have been acquired for 115 targets selected along the HB, the RGB, and the BSS sequence in the UV and optical CMDs presented in Lanzoni et al. (2007c).

The pre-reduction, sky subtraction, heliocentric velocity correction and combination of single exposure spectra has been performed as described in Section 2.2.2.2. The SNR values for the BSS sample ranges between 15 and 30. Instead, the SNR for HBs and RGBs ranges between 25-70 and 15-70, respectively.

4.3 Radial velocities and cluster membership

Radial velocities of the sampled stars have been measured by using the technique described in Section 2.2.2.4.

Figure 4.2 shows the distribution of the measured radial velocities of the 115 targets as a function of the distance from the cluster center. The vast majority of the targets defines a narrow distribution strongly peaked at the systemic velocity of the cluster. The mean value and the standard deviation of the mean obtained from our sample turn out to be 175.1 $\pm$ 0.5 km s^{-1}, while the standard deviation of the sample is σ = 5.2 km s^{-1}, and nicely agrees with the systemic velocity quoted in Baumgardt & Hilker (2018, $< V_r >$ = 174.8 $\pm$ 0.2 km s^{-1}). Such a narrow distribution allows for a straightforward identification of the few field stars contaminating the observed sample: indeed, only seven targets (corresponding to 6% of the total sample) display much smaller radial velocities (well below $< V_r >= 50$ km s^{-1}) and can thus be safely considered as field interlopers (gray circles in Figure 4.2).

Thus, we considered as member stars those within 3σ from the cluster systemic velocity. Only one star (namely #2700733) is marginally consistent with this assumption within the errors. Because this is a FR, the measure of its radial velocity turns out to be more uncertain than the others (see Table 4.2). However, as shown in Figure 4.2, the mean radial velocity of field stars in this region of the sky ($< V_r >= -23.1 \pm 18.5$ km s^{-1}) is very different from that of the cluster ($< V_r >= 175$ km s^{-1}). Hence, the probability that this star is a field interloper is very low. Moreover, its proper motion, from Gaia DR3 (Gaia Collaboration et al., 2016, 2023), turns out to be fully consistent with that of the cluster, thus further confirming its membership.

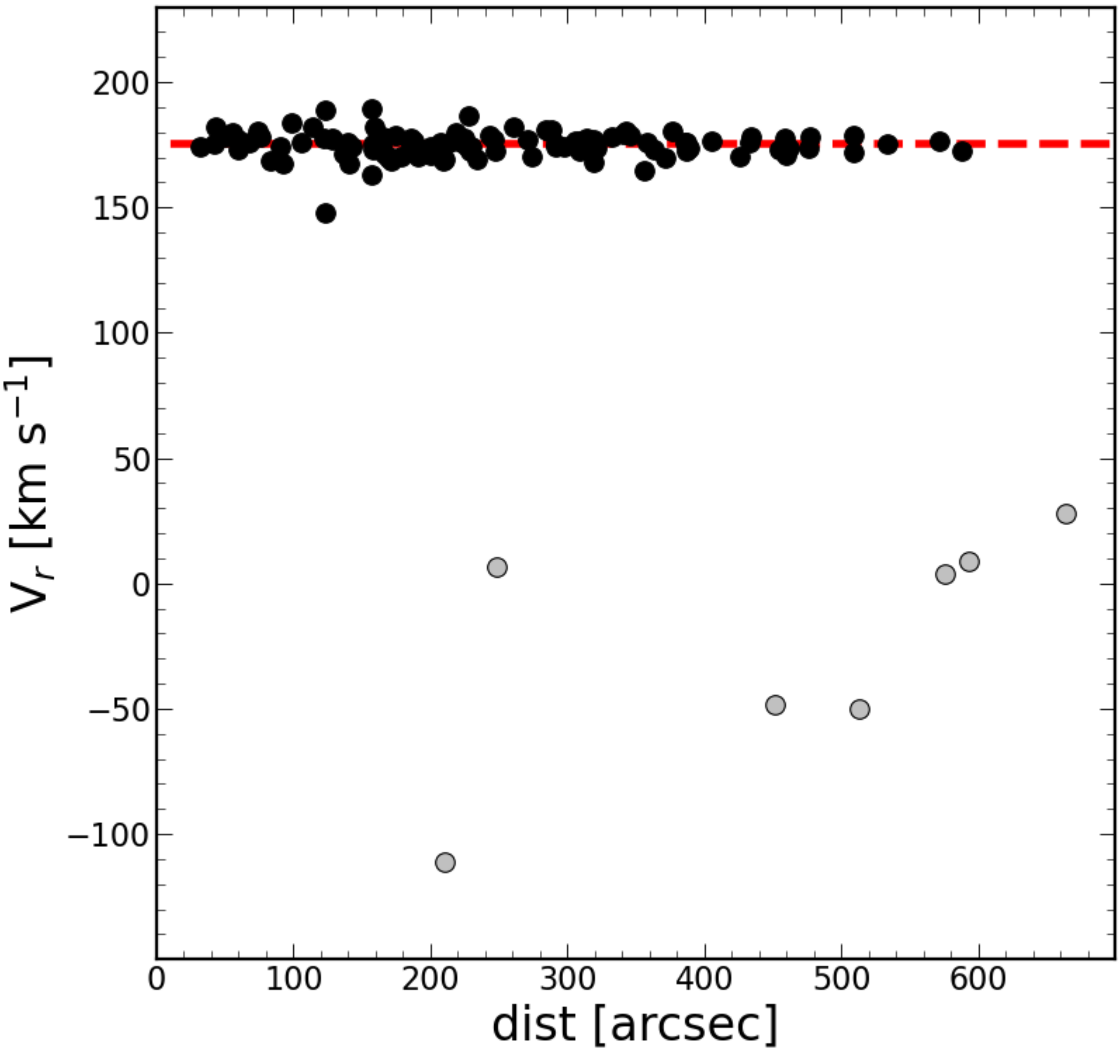

FIGURE 4.2: Radial velocity distribution, as a function of the distance from the cluster center, obtained from the acquired spectra. The black and gray circles correspond to cluster members and Galactic field interlopers, respectively. The red dashed line marks the average radial velocity of the member star sample.

In summary, our sample of likely cluster members include 32 BSSs, 30 RGBs, and 46 HB stars. The 32 surveyed BSSs are a representative sub-sample of the entire population, which in this cluster counts 55-58 objects. In addition, they have been selected to secure adequate sampling of both the luminosity extension of the BSS sequence and the BSS radial distribution. Also the HB sample can be considered representative, since it covers the entire distribution in color (temperature) of the HB evolutionary stage. On the other hand, the few observed RGB stars are just meant to provide a reference population of slow rotators.
For the sake of illustration, Figure 4.3 shows their position in the (B, B−I) CMD obtained from ground-based photometry (Stetson et al., 2019).

4.4 Atmospheric parameters

The values of effective temperature and surface gravity of the spectroscopic targets, have been estimated following the methodology described in Section 2.2.2.3. We used isochrones and HB models from the BASTI-IAC database (Pietrinferni et al., 2021), adopting an α-enhanced mixture and a metallicity [Fe/H]= -1.94 dex (Harris, 1996).

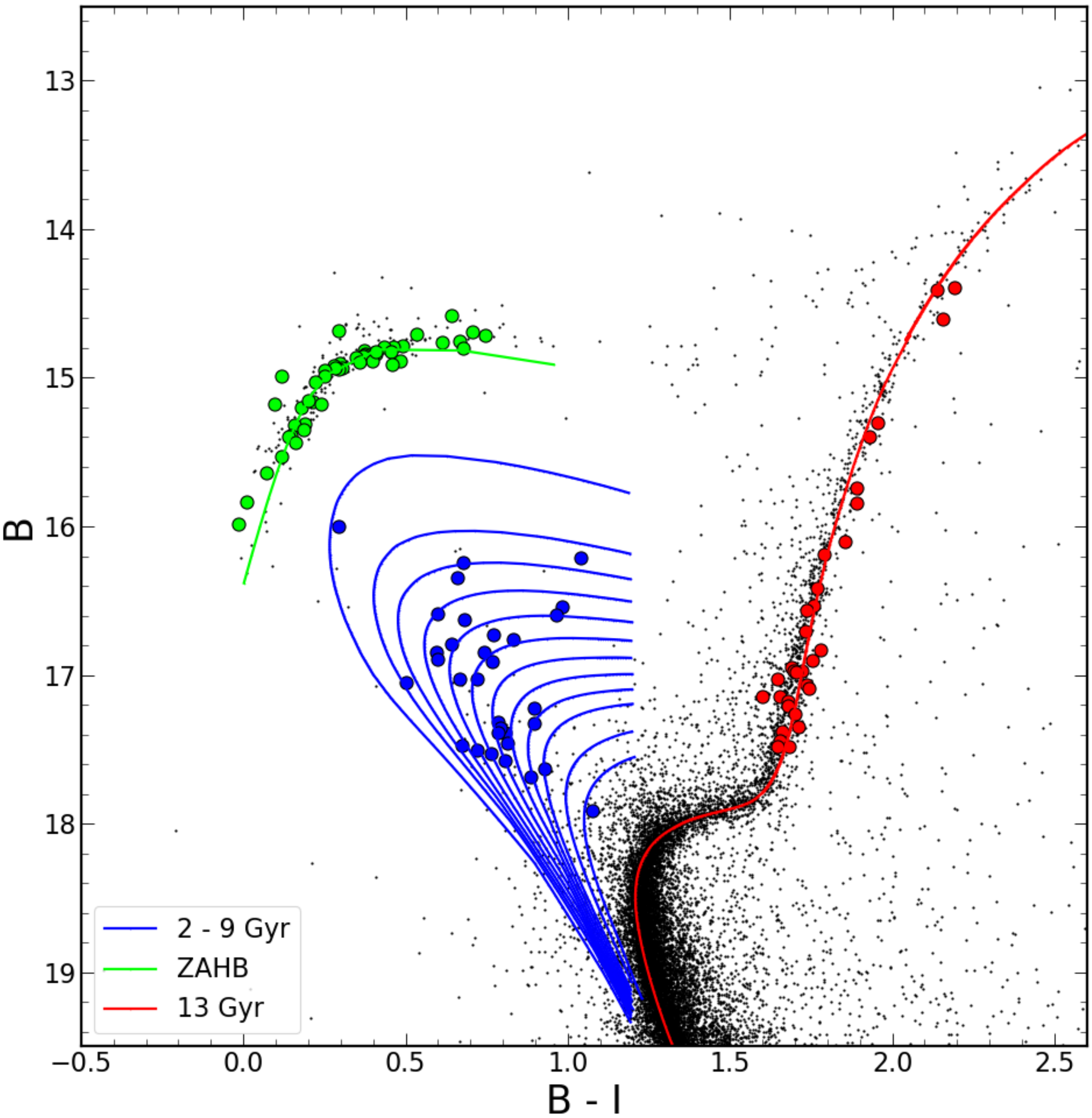

FIGURE 4.3: CMD of M55 (black dots) with the surveyed BSS, RGB and HB stars marked, respectively, as blue, red, and green circles. A set of BASTI isochrones (Pietrinferni et al., 2021) with ages ranging from 2 to 9 Gyr are overplotted as blue lines, a BASTI isochrone of 13 Gyr is overplotted as red line, and a BASTI HB model is overplotted as green line.

To transform the models into the observational CMD, we adopted the distance modulus quoted in Harris (1996) and then applied a slightly larger value of the reddening, E(B-V) =

0.11 mag, instead of E(B-V) = 0.08 (as quoted in Harris, 1996), to optimize the match between the models and the data. We used an HB model with masses ranging from 0.5 $M_{\odot}$ to 0.75 $M_{\odot}$, a 13 Gyr-old isochrone (according to the age estimate by VandenBerg et al., 2013; we note that adopting a slightly younger age has a negligible impact on the temperature and gravity determination) aptly reproducing the RGB location and a set of isochrones with ages ranging from 2 Gyr to 9 Gyr. This allows us to properly sample the BSS region of the CMD (see solid lines in Figure 4.3). Each spectroscopic target has been orthogonally projected on the closest model and the corresponding temperature and gravity have been associated. The resulting values of T_{eff} and $log\ g$ range between 7500-13400 K and 3.0-4.1 dex, respectively, for the HB stars, while for the RGB targets we find T_{eff} = 4800-5400 K and $log\ g$ = 1.7-3.3 dex; for the surveyed BSS sample, we obtained T_{eff} = 6800-9700 K and $log\ g$ = 3.6-4.3 dex. Finally, a microturbulence of 1 km s^{-1} has been assumed for BSSs and HB stars, while 1.5 km s^{-1} has been used for the RGB sample, which are typical values for stars with such temperatures and surface gravities. We note that varying this parameter has a negligible impact on the derived rotational velocities.

4.5 Rotational velocities

The rotational velocities have been determined using the method described in Section 2.2.2.5. This has been done in the spectral region around the Ca II K absorption line at $\lambda = 3933.6$ Å. For the sake of illustration, Figure 4.4 shows the comparison between the observed and the synthetic spectra of two BSSs with different rotational velocities. As can be appreciated, a large value of *v sin(i)* causes a large broadening of the line width. The additional absorption line which is visible in the observed spectra at $\lambda \sim 3931.3$ Å is due to the interstellar medium along to the line of sight. Note that the wavelength of this feature readable from Figure 4.4 is not the rest frame one, because we shifted the observed stellar spectrum to the rest frame to make an appropriate comparison with the synthetic one, but the interstellar medium has a radial velocity different from that of M55. For very slowly rotating BSSs, we assume an upper limit of 3 km s^{-1} for their *v sin(i)* value, because this is the typical uncertainty obtained from the Monte Carlo simulations for these objects.

The uncertainties in the rotational velocities were estimated by using Monte Carlo simulations as described in Section 2.2.2.5. The estimated uncertainties range from a few (2-5) km s^{-1} for slowly rotating stars, up to 10-15 km s^{-1} for the fast-spinning targets.

Figure 4.5 shows the comparison of the rotational velocity distributions obtained for the reference populations (RGB and HB stars) and the BSS sample. All RGB stars are consistent with null or very slow rotation (*v sin(i)* $<$ 10 km s^{-1}), while the HB targets show intermediate

TABLE 4.2: Identification number, coordinates, B-band magnitude and (B−I) color (from Stetson et al., 2019), radial velocity, rotational velocity, and variability type of the analyzed BSSs. The variability is from Kaluzny et al. (2010): SXP means SX Phoenicis, while EW is for contact binary.

ID	R.A. [deg]	Decl. [deg]	B	(B−I)	V_r [km s^{-1}]	$v\ sin(i)$ [km s^{-1}]	Var
100108	294.9850000	-30.9720000	15.99	0.29	178.3 ± 0.2	> 200	
100101	294.9927917	-30.9853056	16.21	1.04	178.1 ± 1.6	21 ± 3	SXP
2700607	295.0269583	-30.9911389	16.25	0.68	177.5 ± 8.5	107 ± 15	SXP
200142	295.0122083	-30.9582222	16.35	0.66	179.3 ± 1.9	95 ± 6	SXP
2700663	294.9460417	-30.9597222	16.54	0.98	174.8 ± 1.9	20 ± 4	SXP
2700733	295.0367500	-30.9546111	16.59	0.60	147.8 ± 12.0	202 ± 15	SXP
2800072	295.0967083	-30.9473611	16.59	0.96	173.6 ± 1.3	125 ± 4	
2700739	294.9941667	-30.9064444	16.63	0.68	169.4 ± 4.9	69 ± 4	
2700785	294.9553750	-30.9422222	16.73	0.77	163.3 ± 0.1	68 ± 5	SXP
2700747	294.9772917	-30.9997222	16.76	0.83	174.5 ± 6.7	70 ± 4	SXP
2700813	295.0688333	-30.9846944	16.79	0.64	186.7 ± 2.9	39 ± 3	
2700834	295.0217500	-30.9895556	16.84	0.59	182.1 ± 8.9	104 ± 10	EW
200178	295.0122917	-30.9748333	16.85	0.74	179.6 ± 1.6	17 ± 2	SXP
200196	294.9982500	-30.9483611	16.89	0.60	176.8 ± 1.3	225 ± 15	SXP
200204	295.0167500	-30.9705278	16.91	0.77	173.4 ± 4.5	199 ± 15	SXP
2700918	294.9522917	-30.9461389	17.03	0.72	173.0 ± 1.1	62 ± 10	SXP
2700925	294.9459583	-30.8815278	17.03	0.67	179.3 ± 1.4	17 ± 3	
100215	294.9859583	-30.9600833	17.05	0.50	182.0 ± 6.2	19 ± 2	
2701036	295.0175000	-30.9150278	17.23	0.89	176.6 ± 1.4	37 ± 2	
200256	295.0286250	-30.9425556	17.32	0.78	177.8 ± 1.2	12 ± 2	SXP
2701130	295.0383333	-30.9453056	17.32	0.89	167.5 ± 0.7	9 ± 3	SXP
100252	294.9789583	-30.9728611	17.35	0.34	176.1 ± 3.6	4 ± 1	SXP
2701162	294.9395000	-30.9343611	17.39	0.79	175.7 ± 4.0	40 ± 4	SXP
2701145	294.9740000	-31.0132222	17.39	0.81	172.5 ± 1.2	< 3	SXP
100256	294.9752083	-30.9690278	17.46	0.81	180.3 ± 5.6	35 ± 4	SXP
100280	294.9942083	-30.9569444	17.47	0.67	174.3 ± 3.5	< 3	SXP
2701235	295.0499583	-31.0348889	17.50	0.72	174.2 ± 3.4	26 ± 3	SXP
2701308	295.0078750	-30.9275556	17.53	0.76	171.3 ± 4.1	69 ± 6	SXP
2701374	294.9658750	-30.9316389	17.57	0.81	189.3 ± 1.1	< 3	SXP
2701376	295.0330417	-30.9474167	17.63	0.93	189.1 ± 1.4	59 ± 4	SXP
200354	295.0214583	-30.9805278	17.68	0.88	174.2 ± 1.4	20 ± 4	
2701676	294.9928333	-30.9187778	17.92	1.08	171.2 ± 1.6	< 3	

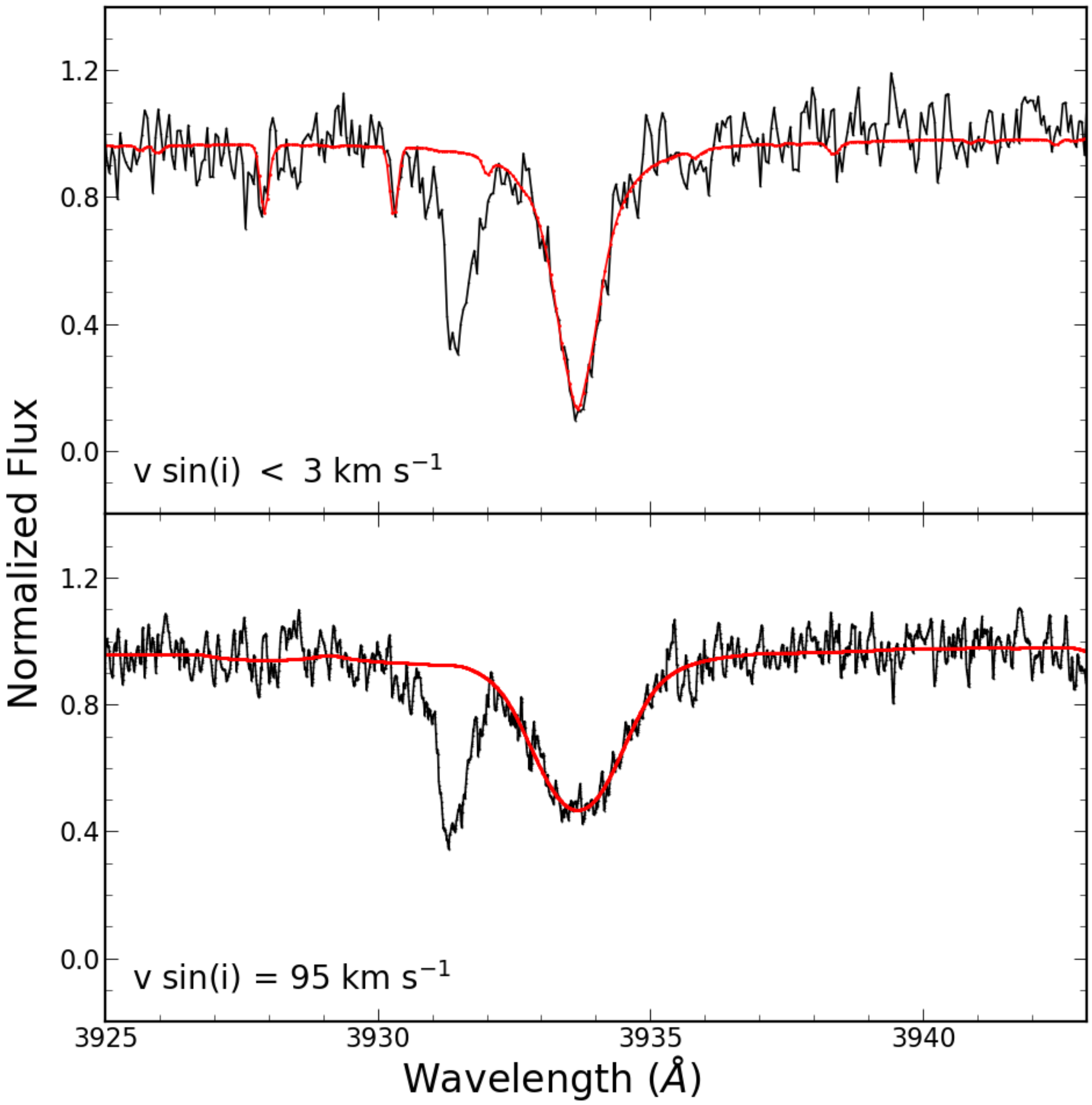

FIGURE 4.4: Comparison between the observed spectra (black lines) and the synthetic spectra (red lines) of two BSSs with different rotational velocities (see labels).

rotational velocity values, not exceeding 40 km s^{-1} (see Table 4.3). The distribution found for BSSs is instead much broader, with a tail extending up to rotational velocities of $\sim$ 200 km s^{-1}. In particular, the fraction of FR objects is zero in both the reference (RGB and HB) samples, while it rises to $\sim$ 47$\pm$14% (15 out of 32) for the BSS population. This is the largest fraction of FR-BSSs ever detected in a GC.

Figure 4.6 shows a zoom in the HB region of the CMD, with different markers corresponding to stars spinning faster and slower than 20 km s^{-1} (see the legend). With the exception of just one object (out of 13), the HB stars showing large *v sin(i)* were found to be located in the redder part of the sequence, at (B$-$I) $>$ 0.2. At bluer colors, only slowly rotating HB stars

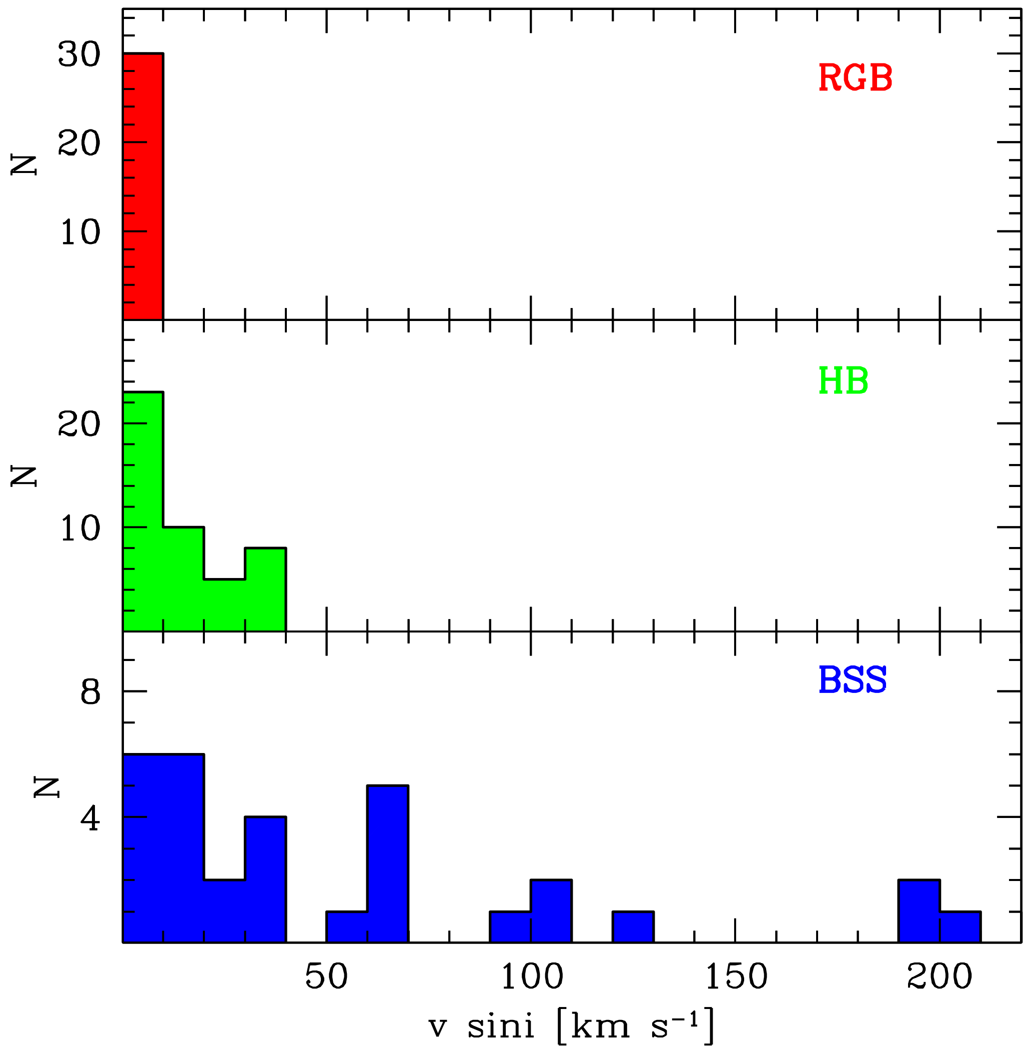

FIGURE 4.5: Rotational velocity distributions of RGB stars (top panel), HB stars (middle panel), and BSSs (bottom panel).

were found. A decrease of *v sin(i)* for increasing effective temperature in HB stars has been already observed in other GCs (see Section 2.1.3), for instance in M13, M15, and NGC 6397 (Behr et al., 2000a,b; Lovisi et al., 2012), but the physical mechanism that reduces the rotation in hot HB stars is not fully understood yet. Sills & Pinsonneault (2000) suggested that this might be due to the onset of gravitational settling mechanisms. The strong gradient in the element abundances can suppress the angular momentum transport and this prevents the stars from having a high *v sin(i)*. Vink & Cassisi (2002) argued that the decrease in rotational velocity for HBs hotter than 11,000 K is due to a loss of angular momentum caused by stellar winds set up by the radiative levitation.

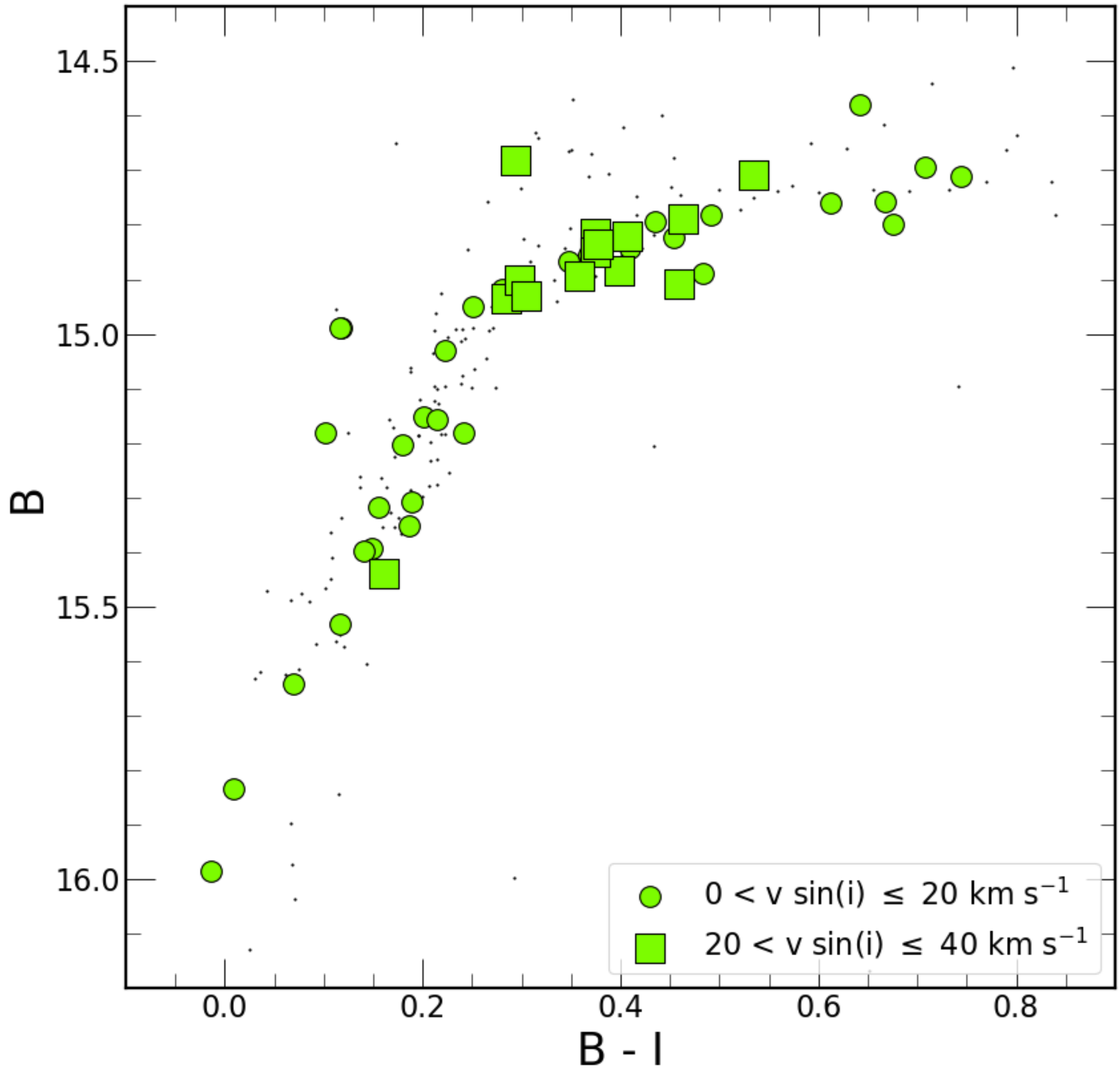

FIGURE 4.6: HB region of the CMD of M55 with the observed stars highlighted with different markers: small green circles for HB stars with *v sin(i)* $\leq$ 20 km s^{-1}, large green squares for those rotating faster (up to 40 km s^{-1}).

TABLE 4.3: Identification number, coordinates, B-band magnitude and (B−I) color (from Stetson et al., 2019), radial velocity and rotational velocity of the analyzed HBs.

ID	R.A. [deg]	Decl. [deg]	B	(B−I)	V_r [km s^{-1}]	$v\ sin(i)$ [km s^{-1}]
100022	294.97350000	-30.97238889	14.76	0.67	168.4 ± 0.6	0 ± 3
100040	294.99050000	-30.95561111	14.82	0.37	175.4 ± 4.3	30 ± 1
2600033	294.91079167	-30.98827778	14.88	0.40	180.8 ± 0.6	29 ± 1
2600030	294.89508333	-30.95577778	14.89	0.48	173.5 ± 0.8	19 ± 1
2600034	294.90591667	-30.89708333	14.91	0.46	180.7 ± 0.8	24 ± 1
2200022	294.97966667	-30.84552778	14.94	0.28	175.7 ± 0.6	40 ± 1
2600036	294.84300000	-30.90063889	14.95	0.25	175.5 ± 1.0	16 ± 1
2600043	294.89895833	-30.97269444	15.18	0.24	176.6 ± 0.6	11 ± 1
2600050	294.89700000	-30.91725000	15.35	0.19	176.1 ± 1.8	19 ± 1
2600049	294.90816667	-31.03872222	15.39	0.15	175.7 ± 0.6	19 ± 2
2600051	294.88725000	-31.01505556	15.40	0.14	173.5 ± 0.5	11 ± 1
2600052	294.91270833	-30.99797222	15.44	0.16	175.5 ± 4.7	37 ± 2
2600055	294.91037500	-30.97263889	15.53	0.12	170.5 ± 0.6	8 ± 1
2700108	295.05587500	-30.95638889	14.58	0.64	170.4 ± 0.6	9 ± 3
2700146	295.06483333	-30.97202778	14.68	0.29	171.0 ± 4.2	5 ± 3
2700155	295.05008333	-30.93752778	14.69	0.71	177.5 ± 0.5	16 ± 3
2700135	295.02591667	-31.03341667	14.71	0.53	182.0 ± 2.8	35 ± 1
2800007	295.11408333	-30.96672222	14.71	0.74	165.0 ± 0.6	6 ± 3
2700143	294.93083333	-31.03638889	14.76	0.61	178.0 ± 1.6	5 ± 3
2700163	294.98375000	-31.00127778	14.78	0.49	175.7 ± 2.7	9 ± 1
2700182	295.00612500	-31.01697222	14.79	0.46	172.2 ± 4.1	23 ± 1
2700172	294.98195833	-31.02808333	14.80	0.44	169.0 ± 1.9	0 ± 1
2700147	294.99037500	-31.07194444	14.80	0.68	176.2 ± 0.7	5 ± 3
2700175	294.93162500	-31.03033333	14.82	0.45	177.5 ± 2.5	10 ± 1
2700210	295.05012500	-30.96613889	14.84	0.38	182.0 ± 1.1	30 ± 1

Continue...

ID	R.A. [deg]	Decl. [deg]	B	(B−I)	V_r [km s^{-1}]	$v\ sin(i)$ [km s^{-1}]
2700208	294.93487500	-30.99125000	14.84	0.41	179.8 ± 0.6	10 ± 1
2700198	294.98683333	-31.02747222	14.85	0.37	172.5 ± 0.6	33 ± 1
2700195	294.98537500	-31.04411111	14.86	0.37	181.0 ± 2.7	8 ± 1
2700239	295.04704167	-30.97933333	14.87	0.35	175.5 ± 1.1	11 ± 1
2700235	295.07812500	-30.95716667	14.90	0.36	176.8 ± 1.8	32 ± 1
2700241	295.06908333	-30.94397222	14.90	0.30	174.0 ± 2.6	38 ± 1
2700256	295.07054167	-30.96963889	14.92	0.28	176.0 ± 0.6	6 ± 1
2700262	294.97854167	-30.92097222	14.93	0.30	170.0 ± 2.0	40 ± 1
2700240	295.03962500	-31.04566667	14.94	0.29	173.0 ± 1.6	18 ± 1
2700286	295.00025000	-31.02027778	14.99	0.12	171.0 ± 0.5	9 ± 1
2700279	295.08258333	-30.96252778	14.99	0.25	174.0 ± 0.9	8 ± 1
2700300	294.96691667	-30.90791667	15.03	0.22	174.0 ± 2.8	8 ± 1
2700333	294.99866667	-30.90719444	15.15	0.20	176.0 ± 2.7	7 ± 1
2700336	294.94416667	-30.97305556	15.16	0.22	168.5 ± 2.5	6 ± 1
2700343	295.08229167	-30.99952778	15.17	0.10	180.5 ± 1.0	10 ± 1
2700355	295.03258333	-31.00016667	15.20	0.00	178.0 ± 2.4	6 ± 1
2700384	294.93695833	-30.96238889	15.31	0.19	170.5 ± 3.6	18 ± 1
2700381	295.01091667	-31.03152778	15.32	0.16	178.5 ± 2.5	10 ± 1
2700453	294.94620833	-31.00797222	15.64	0.07	177.5 ± 0.6	7 ± 1
100105	294.96875000	-30.96430556	15.83	0.01	167.7 ± 0.7	8 ± 1
2700537	294.95195833	-30.99177778	15.98	-0.01	178.5 ± 0.6	8 ± 1

4.6 Results and discussion

This work presents the results of our study about the rotational velocities of BSSs in the GGC M55.

As shown in Figure 4.5, while the reference (RGB and HB) stars are all slow rotators, with values of $v\ sin(i)$ below the threshold of 40 km s^{-1}, the BSS rotational velocity distribution shows a more complex distribution with a long tail, extending up to $\sim$ 200 km s^{-1} at high values. This distribution is similar to those found in M4 (Lovisi et al., 2010), ω Centauri (Mucciarelli et al., 2014), and NGC 3201 (see Chapter 3).

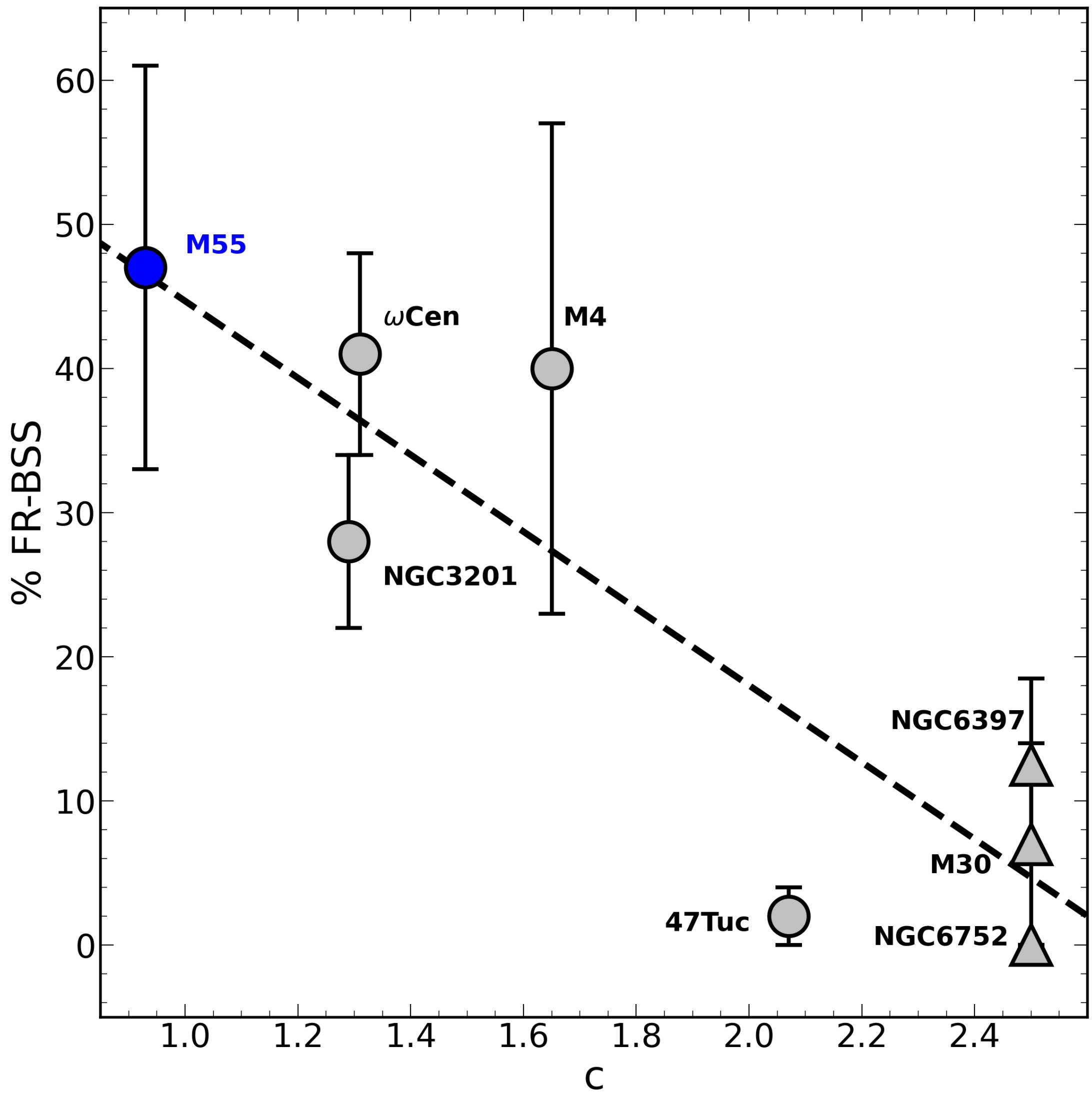

FIGURE 4.7: Percentage of FR-BSSs as a function of the King concentration of the parent cluster, for the systems studied in Ferraro et al. (2023a). The position of M55 is highlighted in blue.

In Figure 4.7, we report the behavior of the percentage of FR-BSSs as a function of the parent cluster King concentration, with M55 highlighted in blue. As can be seen, this is the system with the largest fraction of FR-BSSs and the smallest concentration value in the sample of GCs investigated so far.

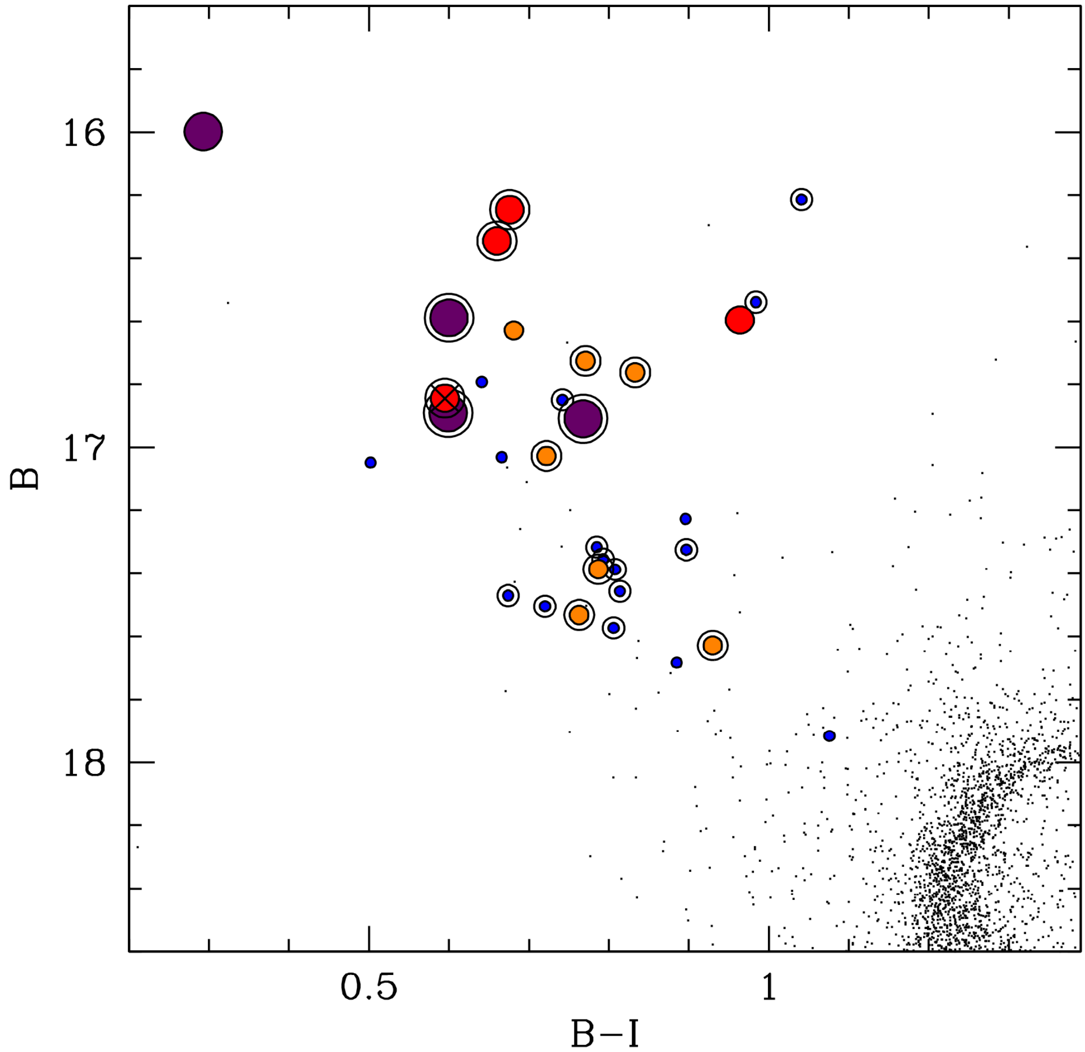

FIGURE 4.8: CMD of M55 zoomed in the BSS region, with the measured BSSs highlighted as large colored circles. The slowly rotating BSSs are marked with small blue circles. The FR-BSSs are plotted as increasingly larger circles for different colors for increasing rotational velocity (in units of km s^{-1}): orange color for $40 \le v\ sin(i) < 80$, red color for $80 \le v\ sin(i) < 180$, and violet for $v\ sin(i) \ge 180$ km s^{-1}. All the BSSs identified as variable stars in the Kaluzny et al. (2010) catalog are highlighted with large open circles. The FR-BSS classified as contact binary is marked with a large black cross.

Figure 4.8 shows the location of the measured BSSs in the CMD, plotted as circles of different sizes and colors depending on their rotational velocity. The slowly rotating BSSs (with *v sin(i)* < 40 km s^{-1}) are plotted as small blue circles, while FR-BSSs are increasingly larger circles with orange color for *v sin(i)* between 40 and 80 km s^{-1}, red color for rotational velocities ranging from 80 to 180 km s^{-1}, and violet color for the high-rotation tail, with *v sin(i)* ≥ 180 km s^{-1}. We also checked our BSS sample for variability, performing a cross-correlation with the catalog of Kaluzny et al. (2010) and finding that 23 (out 32) of the sampled BSSs are indeed variables (see large empty circles in Figure 4.8): 12 of them are FR-BSSs, while the remaining 11 are slow rotators. Almost all the detected variables (22 out of 23) are non binary systems, but pulsating stars classified as SX Phoenicis. The only exception star #2700834 (black cross in the figure), which is cataloged as a contact binary with asymmetric maxima as consequence of mass transfer. This is a FR-BSS with *v sin(i)* $= 104\ km\ s^{-1}$, thus possibly indicating a system where MT is still ongoing, hence a proto-BSS in its way of formation.

The inspection of the Figure 4.8 also suggests that FR-BSSs tend to populate the brightest portion of the BSS sequence: 12 FR-BSSs (out of 18 surveyed stars) are found at B < 17.2, while only 3 FR-BSSs (out of 14) can be counted in the lower portion of the sequence, thus indicating that FR-BSSs tend to be more luminous than slowly rotating BSSs. This is also supported by the cumulative magnitude distribution of the samples of slowly and rapidly rotating BSSs shown in Figure 4.9. By using a KS test, we find that the probability that the two distributions are extracted from the same parent population is of the order of 0.7% (roughly corresponding to a 2.5σ significance level). This is in good agreement with what observed in NGC 3201. Conversely, we found no clear difference between the cumulative color (temperature) distributions of slow and fast rotating BSSs.

The dependence between rotational velocity and cluster-centric distance for the BSSs surveyed in M55 is plotted in Figure 4.10. The trend is less clear here than in NGC 3201 (compare with Figure 3.9), and the KS test detects no significant difference between the radial distributions of fast and slowly rotating BSSs. Nevertheless, we can notice that the BSSs with extremely large rotational velocities (*v sin(i)* > 200 km s^{-1}), which are also the brightest in the surveyed sample (see Figure 4.8), are all concentrated in the inner region of the cluster. As discussed in Chapter 3, this can be explained by assuming that the fastest (and brightest) BSSs are also the most massive ones and, therefore, they suffered the effect of mass segregation that made them sink toward the cluster center. The difference in the radial distributions observed in M55 and NGC 3201 is consistent with their different value of the A^{+}_{rh} parameter, which quantifies the level of dynamical evolution experienced by the host cluster (Alessandrini et al., 2016). According to Ferraro et al. (2023a, see also Lanzoni et al., 2016; Ferraro et al., 2018a), M55 has a value of A^{+}_{rh} significantly smaller than NGC 3201 ($A^{+}_{rh} = 0.10$, compared to 0.19). This clearly indicates that M55 is less dynamical evolved than NGC 3201, consistently with the detected difference in the trend between *v sin(i)* and radial distance between the two clusters.

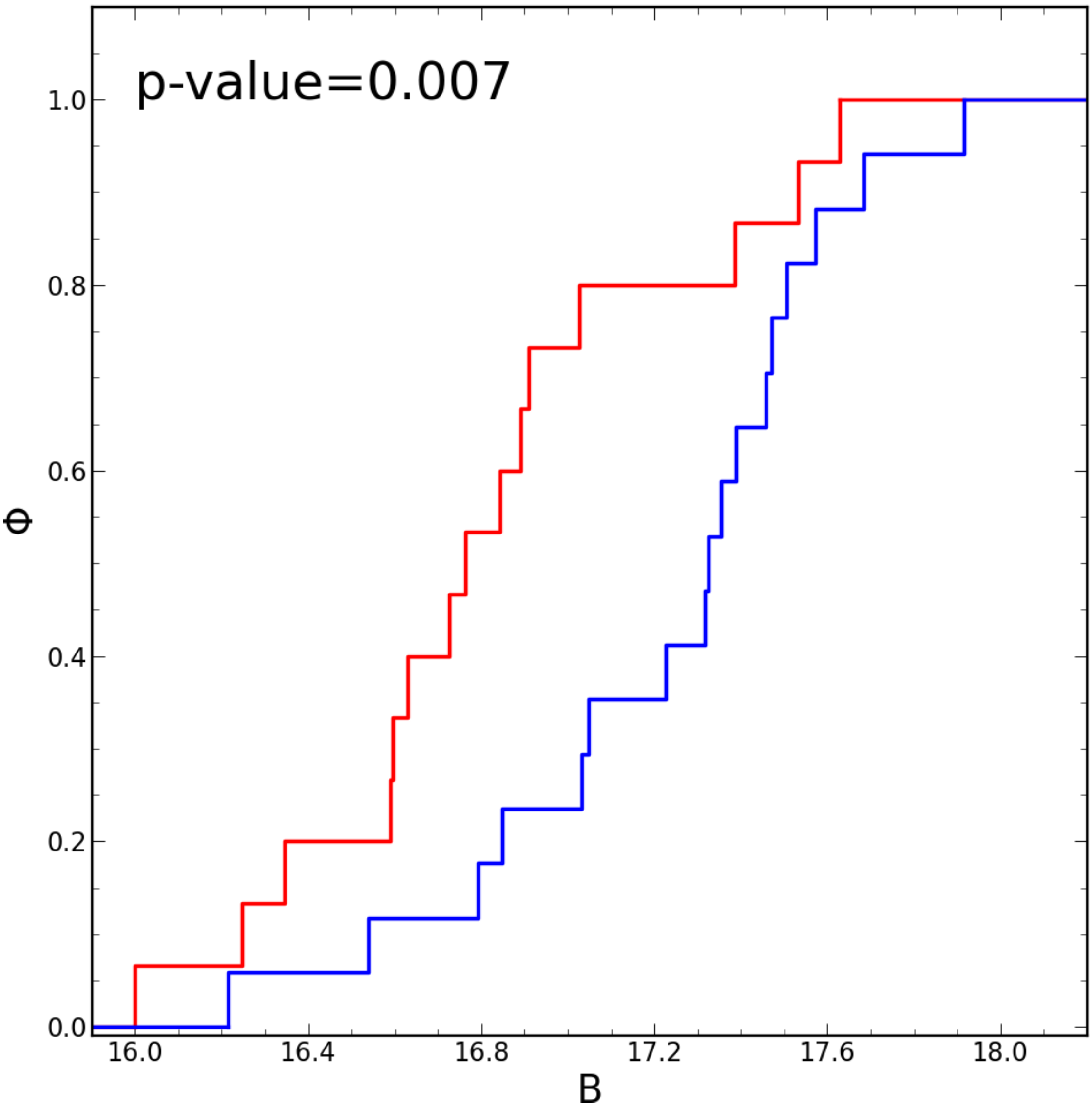

FIGURE 4.9: Cumulative distribution of FR-BSSs (red line) and slowly rotating BSSs (blue line) as a function of the B magnitude.

The comparison of the CMD position of the measured BSSs with theoretical evolutionary tracks can provide some additional insights. We should remind that caution is needed in estimating the mass of BSSs from the comparison with evolutionary tracks computed for normal single stars. However, Raso et al. (2019) found a reasonable agreement between the masses derived from single star evolutionary tracks and those estimated from the fitting of the observed spectral energy distribution, thus suggesting that the former can be used at least as first-guess indication. Figure 4.11 shows the CMD of M55 zoomed in the BSS region, with the dashed lines corresponding to single-mass theoretical tracks extracted from the BASTI database (Pietrinferni et al., 2021) for masses ranging from 0.9 to 1.6 $M_{\odot}$, stepped by

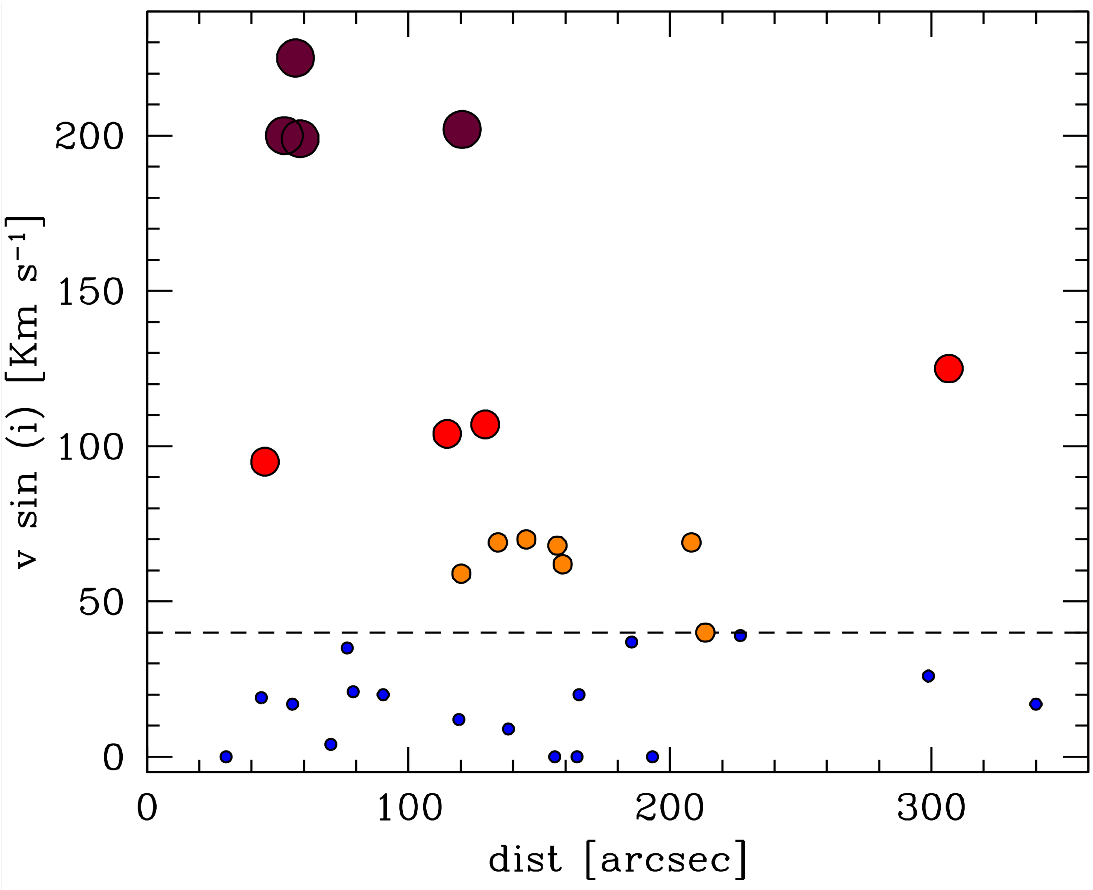

FIGURE 4.10: BSS rotational velocities as a function of the radial distance from the cluster center. The symbols are as in Figure 4.8. The dashed line marks the threshold adopted to distinguish fast-rotating from slowly rotating stars.

0.1 $M_{\odot}$. The position of the fastest rotators in the sample (i.e., the four BSSs with rotational velocity larger than 190 km s^{-1}) suggests that three of them (namely #200196, #200204, #2700733) have masses of the order of 1.1 $M_{\odot}$, and the brightest object (#100108) is as massive as $\sim$ 1.5 $M_{\odot}$, very close to twice the cluster TO-mass.

The latter deserves a few comments. In fact, the Ca II K line is not visible in the spectrum of this very hot ($T_{eff} > 9700$ K) BSS, because its extremely large rotational velocity has spread out the line and made it indistinguishable from the continuum. Hence, the assumed velocity of 200 km s^{-1} is indeed a lower limit. This BSS is located in the innermost region of the cluster, at only 52" from the center, where optical, ground-based observations could be problematic. To confirm its peculiar position in the CMD, we therefore used HST data acquired with the Wide Field Camera 3 (WFC3) in the context of the HST UV Legacy Survey of GGCs (see Piotto et al., 2015; Nardiello et al., 2018). Figure 4.12 shows the CMD of M55 obtained in different HST filter combinations, with the BSSs included in the WFC3 field of view highlighted as large colored circles (same symbols as in Figure 4.11). Clearly, star

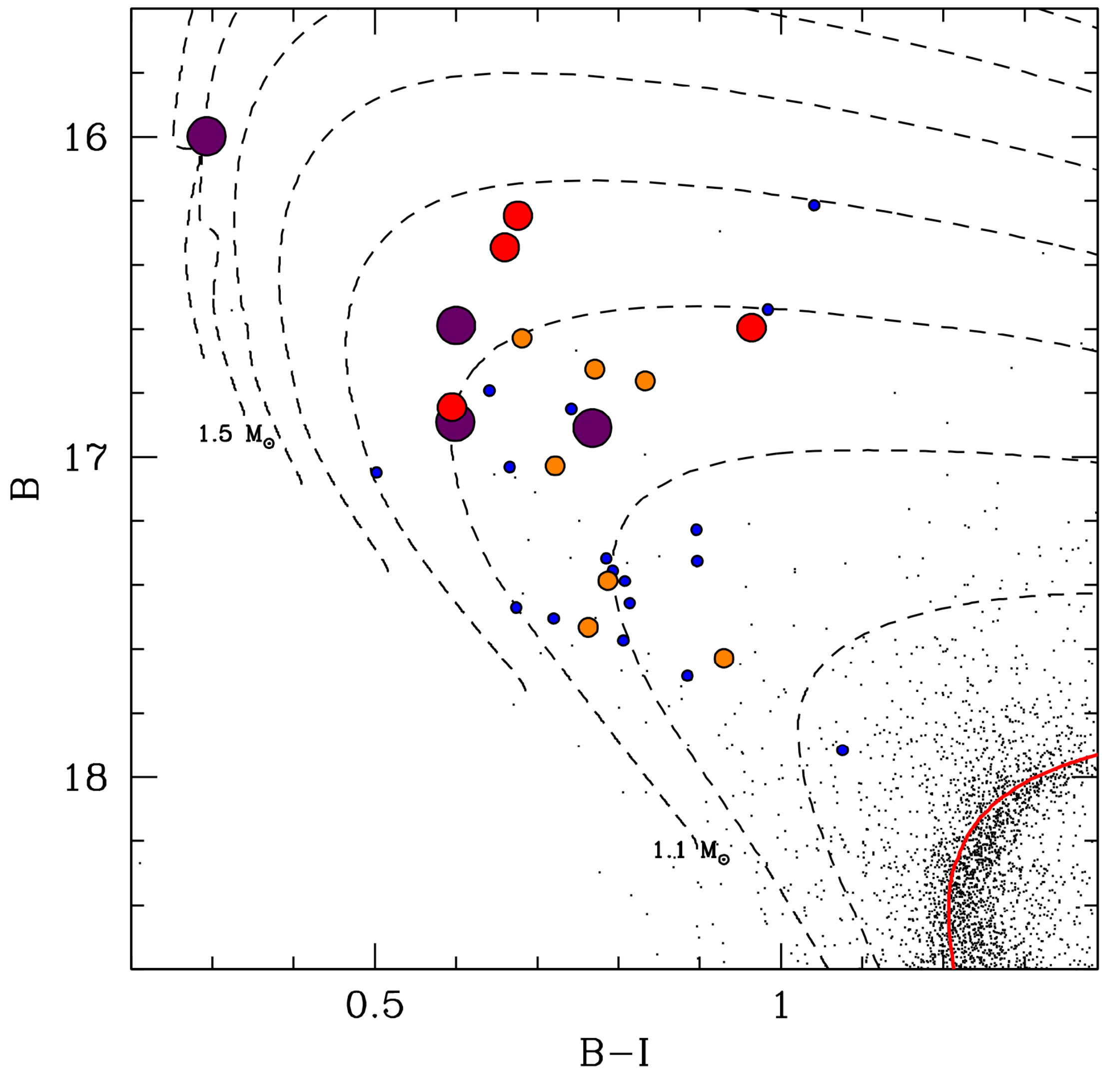

FIGURE 4.11: CMD of M55 zoomed in the BSS region, with the surveyed BSSs highlighted as colored circles (see Figure 4.8). The dashed lines are evolutionary tracks extracted from the BASTI database (Pietrinferni et al., 2021) for stellar masses ranging from 0.9 to 1.6 $M_{\odot}$, stepped by 0.1 $M_{\odot}$. The red solid line is the evolutionary track at 0.8 $M_{\odot}$ reproducing the cluster MS-TO region.

#100108 is the bluest and the brightest BSS, with a position well compatible with a mass of the order of $1.5 - 1.6\ M_{\odot}$, in all filter combinations.
The evolutionary time of such a relatively massive star is expected to be quite fast, thus indicating that the formation of this BSS must have occurred recently. Interestingly, the evolutionary time read along the stellar track indicates that a 1.5 $M_{\odot}$ star needs approximately 1 Gyr to reach the current CMD position of star #100108, from the instant of formation. Thus, this seems to be a BSS that, 1 Gyr after its formation, is spinning at a velocity higher than 200 km s^{-1}. Following this line of reasoning, the other three very FR-BSSs, which have masses significantly smaller ($\sim 1.1\ M_{\odot}$) than BSS #100108, should be still spinning very rapidly after 3

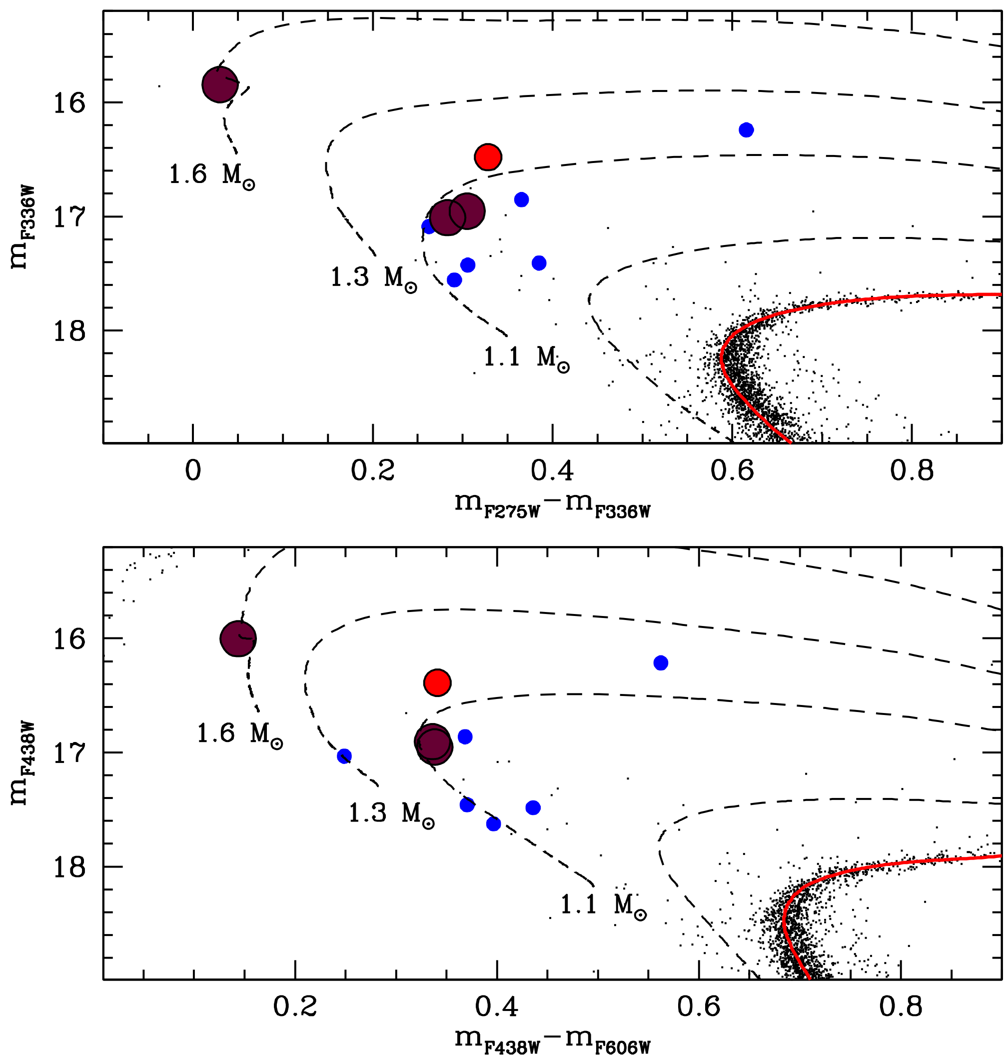

FIGURE 4.12: As in Figure 4.11, but for the BSSs sampled in the HST WFC3 field of view and for different color-magnitude combinations (see x- and y-labels). The four FR-BSSs are #100108 (the brightest and bluest one), #200204 and #200196 (the other large violet circles), and #200142 (red circle).

Gyr from their formation. The reading of the evolutionary time from single star theoretical tracks therefore suggests a not particularly efficient braking mechanism, with newly-formed BSSs being able to maintain a strong rotation for several Gyr. However, we notice that also the FR-BSS #2700834 (classified as a contact binary with ongoing MT activity; see Kaluzny et al., 2010) is located at the same position in the CMD (see Figure 4.8). This suggests that 1-3 Gyr old BSSs, as well as BSSs on the way of their formation, can occupy the same region of the diagram during their evolution. This result is indeed predicted by theoretical MT models specifically designed to describe the BSS population of M30 (see Xin et al., 2015; Jiang et al., 2017). Thus, while a first-guess estimate of BSS masses can be reasonably derived from the comparison with single star evolutionary tracks, extreme caution must be taken in reading the evolutionary timescale from the same models. This emphasizes the urgency of complete grids of MT-BSS models for an appropriate reading of the BSS evolutionary path.

CHAPTER 5

Fast Rotating Blue Straggler Stars in the globular cluster NGC 1851

Based on the results published in:

- *Billi, A., Monaco L., Ferraro, F. R., Mucciarelli, A., Lanzoni B., Cadelano M., and Trangolao I., 2026,* A&A, *705, A36.*

5.1 Introduction

NGC 1851 (see Figure 5.1) is the third GGC analyzed in this Thesis. Table 5.1 reports the main physical properties of this cluster.

Table 5.1: General properties of the GGC NGC 1851

RA J2000	78°.528160	(Baumgardt & Hilker, 2018)
Dec J2000	-40°.046555	(Baumgardt & Hilker, 2018)
Mass M	$2.83 \times 10^5\ M_\odot$	(Baumgardt & Hilker, 2018)
Distance from Sun	12.1 kpc	(Harris, 1996)
Core radius r_c	0.09'	(Harris, 1996)
King concentration c	1.86	(Harris, 1996)
Central luminosity density $log\ \rho_0$	$5.09\ L_\odot\ pc^{-3}$	(Harris, 1996)
$[Fe/H]$	-1.18 dex	(Harris, 1996)
A^+_{rh} parameter	0.48	(Ferraro et al., 2018a)

As shown in the table, its distance from Earth is bigger than other two clusters previously studied. This implies that these stars have fainter observed magnitudes, as can be easily seen from the magnitude of the TO in Figure 5.2.

FIGURE 5.1: Image of the GGC NGC 1851, observed with HST WFC 3. Credits: NASA/ESA, and G. Piotto

Among all the clusters of the survey, NGC 1851 is the only one with an intermediate value of King concentration. This concentration range has been never explored and will add fundamental pieces of information in the understanding of these puzzling stars. This chapter is devoted to the detailed presentation and discussion of the analysis of 15 BSSs and 45 reference stars (e.g. HBs and RGBs) observed in the GGC NGC 1851.

5.2 Observations

This work is based on stellar spectra obtained with the high resolution multi-object spectrograph FLAMES-GIRAFFE (Pasquini et al., 2002) mounted on the VLT at ESO Paranal

Observatory, under programmes 090.D-0487(A) and 092.D-0477(A) (PI: Simunovic). The observations have been performed in different nights between November 2012 and October 2013, using the HR9A setup, covering the wavelength interval $\Delta\lambda$ = 5095 - 5404 Å, which samples the Mgb triplet lines (λ_1 = 5167.4 Å , λ_2 = 5172.7 Å, λ_3 = 5183.6 Å). These three lines are very sensitive to *v sin(i)*, as demonstrated in recent studies on BSS rotational velocities (see Chapter 3, and also see Mucciarelli et al., 2014). A total of 15 exposures are available in the ESO archive, and the acquired spectra belong to stars evolving along different evolutionary stages: BSSs, RGB and HB stars (see Figure 5.2, where the adopted photometric catalog is from Stetson et al., 2019). We took the reduced spectra from the online ESO archive[1]. Then, as described in Section 2.2.2.2, we subtracted the median mastersky from the observed spectra and we corrected for the heliocentric velocity and combined together the individual exposures of the same stars. The resulting SNR ranges between 10 and 30 for the sampled BSSs and RGB stars, while it is between 30 and 50 for the HB stars.

5.3 Atmospheric parameters

Atmospheric parameters (such as effective temperature, T_{eff}, and surface gravity, $log\ g$) are fundamental ingredients for the computation of appropriate synthetic spectra to be compared with the observed ones, from which radial and rotational velocities are then measured. They have been estimated by comparing the position of the surveyed stars in the CMD with evolutionary tracks, isochrones and an HB model, as described in Section 2.2.2.2.
The models have been retrieved from the online BASTI-IAC database (Pietrinferni et al., 2021), adopting an α-enhanced mixture and a metallicity [Fe/H] $= -1.18$ dex (Harris, 1996). A set of evolutionary tracks with mass values ranging from 0.9 to 1.5 $M_\odot$ has been used for BSSs, while the atmospheric parameters of HB and RGB stars have been estimated through the comparison with an HB model including stellar masses of 0.65-0.8 $M_\odot$ and an 11 Gyr old (VandenBerg et al., 2013) isochrone, respectively. To estimate the BSS temperatures and surface gravities we orthogonally projected the observed CMD position of each star onto the closest evolutionary track.[2] The models have been plotted in the observed CMD (see Figure 5.2) by adopting a distance modulus $(m - M)_V = 15.47$ and reddening $E(B - V) = 0.02$ (Harris, 1996).
For BSSs the resulting temperatures and $log\ g$ values range between 5700 and 8600 K, and between 3.4 and 4.2 dex, respectively. For RGB stars we obtained T_{eff} values between 5030

[1] `https://archive.eso.org/cms.html`

[2] Note that the estimation of T_{eff} and $log\ g$ using theoretical isochrones (see Chapter 3 and 4) or evolutionary tracks is completely consistent, since isochrones are constructed based on theoretical evolutionary tracks.

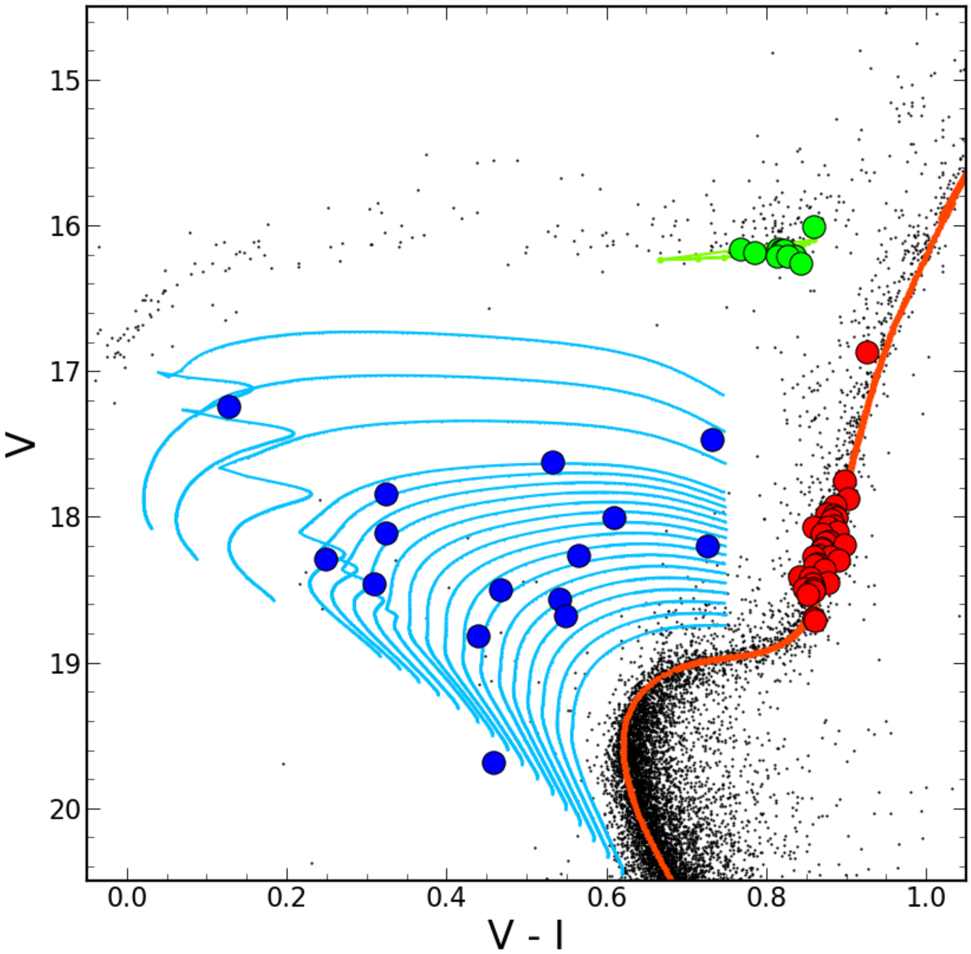

FIGURE 5.2: CMD of NGC 1851 (black dots) with the surveyed BSSs, RGB and HB stars marked, respectively, as blue, red, and green circles. A set of BASTI evolutionary tracks (Pietrinferni et al., 2021) with masses ranging from 0.9 to 1.5 $M_{\odot}$ are overplotted as cyan lines. A BASTI isochrone of 11 Gyr is overplotted as orange line, and a BASTI HB model is overplotted as green line.

and 5350 K, and $\log g$ =[3.3, 3.6] dex. Finally, for HB stars we find T_{eff} = [5300, 5600] K and $\log g$ = [2.4, 2.5] dex. We assumed a microturbolence of 1 km s^{-1} for BSSs and HB stars, whereas for RGB stars we adopted 1.5 km s^{-1}.

5.4 Radial velocities and cluster membership

Radial velocities have been used to assess the cluster membership of the observed stars, following the methodology outlined in Section 2.2.2.4.

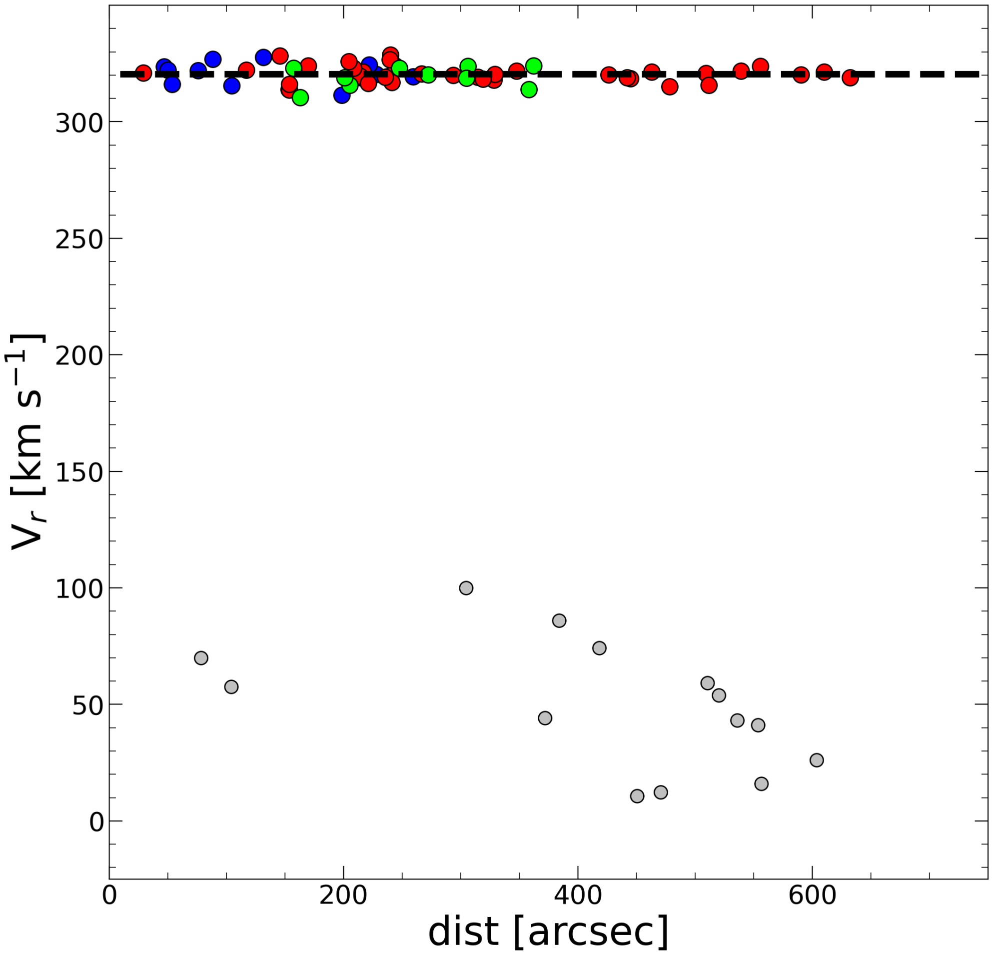

FIGURE 5.3: Radial velocity of the observed stars as a function of their distance from the cluster center. Member BSSs, RGB and HB stars are marked as blue, red and green circles, respectively. The gray circles correspond to Galactic field interlopers. The black dashed line marks the average radial velocity of the member star sample.

Figure 5.3 shows the distribution of the measured radial velocities as a function of the distance from the center. As can be seen, 14 objects have radial velocities inconsistent with that of the bulk population and are clearly Galactic field interlopers. Hence, they have been excluded from the following analysis. The remaining stars tightly align around a mean radial velocity of 320.3 ± 0.5 km s^{-1} (black dashed line in Figure 5.3), a value that is well consistent with the systemic velocity of NGC 1851 quoted in literature: 320.5 ± 0.6 km s^{-1} (Harris, 1996) and 321.4 ± 1.6 km s^{-1} (Baumgardt & Hilker, 2018). They all are within 3σ of the distribution, with $\sigma = 3.9$ km s^{-1}. To further confirm their cluster membership, we took into account the membership probability quoted by Vasiliev & Baumgardt (2021) and estimated from Gaia DR3 proper motions (Gaia Collaboration et al., 2016, 2023), finding that they all have membership probability larger than 90%. For one of the surveyed BSSs we measure V_r = 287.8 km s^{-1}. However, this is a very FR-BSS and, because its spectral lines are extremely broadened, the obtained value is not reliable. However, this star (Gaia ID: *4819197058394790528*) has membership probability > 0.9 in Vasiliev & Baumgardt (2021), and we therefore kept it in the final sample of bona fide members, which includes a total of 15 BSSs, 35 RGB and 10 HB stars.

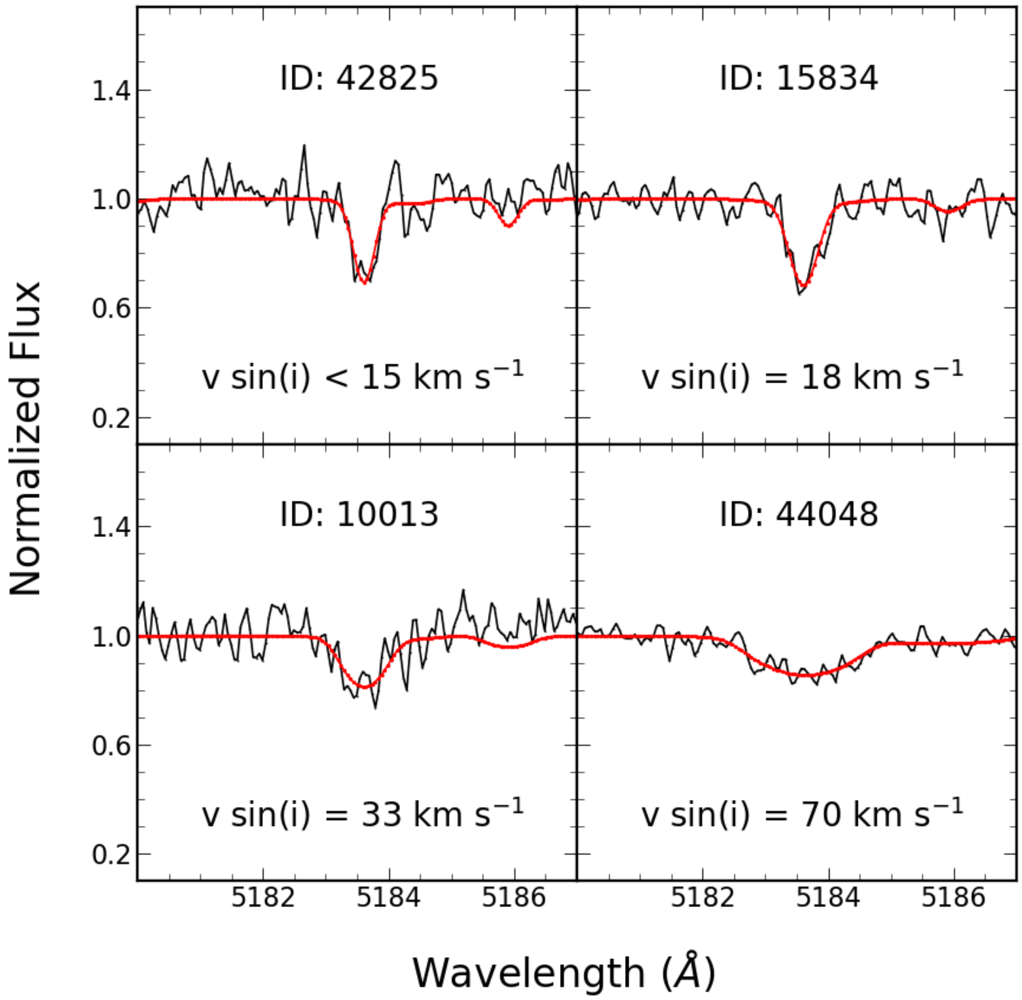

FIGURE 5.4: Comparison between the observed spectrum (black line) and the best-fit synthetic spectrum (red line) of four BSSs with different rotational velocities (see labels).

5.5 Rotational velocities

Rotational velocities have been measured using a χ^2 minimization method as described in Section 2.2.2.5. More specifically, we selected the Mgb triplet lines, in particular we used the third line (λ_3 = 5183.6 Å) that allows the best and cleanest comparison. Figure 5.4 shows the comparison between the observed spectrum and the best-fitted synthetic spectrum for the third line of the Mgb triplet, for a sample of four BSSs with different values of rotational velocities.

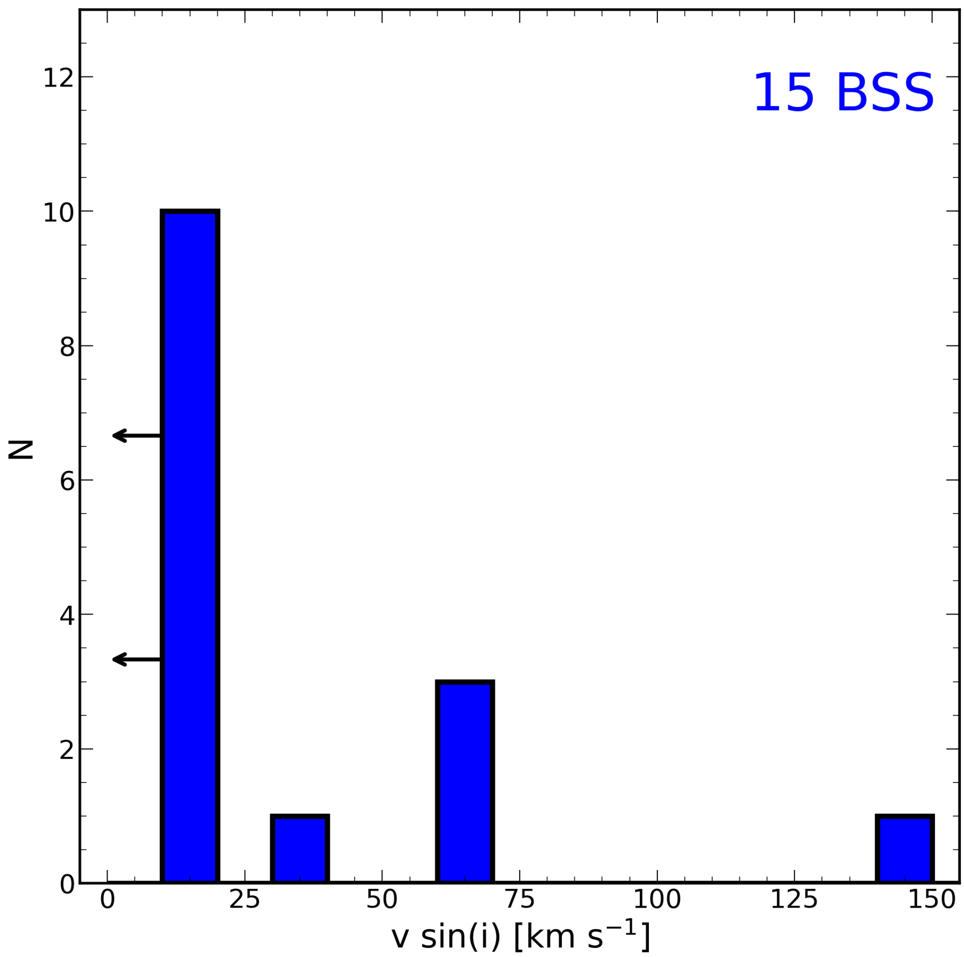

FIGURE 5.5: Rotational velocity distribution of the 15 BSSs analyzed in this study. Left arrows indicate the upper limit of 15 km s^{-1} adopted for very slow rotating BSSs.

Clearly, the broader is the observed line, the higher is the stellar rotational velocity. Table 5.2

lists the values obtained for each member BSS. Due to the moderate resolution and relatively low SNR of the spectra, we are not able to distinguish very slow rotating stars (with *v sin(i)* $< 15\ km\ s^{-1}$). Therefore, we adopt an upper limit for those stars. RGBs and HBs, as expected, show very slow rotation, with *v sin(i)* $< 15\ km\ s^{-1}$. This is consistent with findings showed in Chapter 3 and Chapter 4 and also in previous studies (Ferraro et al., 2023a).
The distribution of *v sin(i)* values obtained for the surveyed sample of BSSs is shown in Figure 5.5. As can be seen, the rotational velocity distribution of BSSs is different from those of "normal" cluster stars. As said before, all RGB and HB stars rotate more slowly than 15 km s^{-1}, whereas some BSSs not only have *v sin(i)* values above this threshold, but even show rotational velocities exceeding 100 km s^{-1}.
In particular, in NGC 1851 we find 4 FR-BSSs out of the 15 BSSs analyzed, which corresponds to a total fraction of $27 \pm 14\%$. The uncertainty on the fraction of FR-BSSs has been calculated using the propagation of uncertainty of a ratio. Rotational velocity uncertainties listed in Table 5.2 have been calculated using a Monte Carlo simulation, as described in Section 2.2.2.5.

Table 5.2. Identification number of the Stetson and Gaia catalogs, J2000 coordinates, V-band magnitude and (V−I) color (from Stetson et al., 2019), radial velocity and rotational velocity of the analyzed BSSs.

ID	ID Gaia	R.A. [deg]	Decl. [deg]	V	(V−I)	V_r [km s^{-1}]	$v\ sin(i)$ [km s^{-1}]
23317	4819197883024929280	78.5151667	-40.0114722	18.50	0.47	327.7 ± 1.0	16 ± 2
42825	4819291547673927808	78.5921250	-39.9938333	18.57	0.54	319.3 ± 1.0	< 15
44048	4819279693564194432	78.6020000	-40.0180556	17.63	0.54	320.3 ± 3.9	69 ± 4
44561	4819279620550033024	78.6068333	-40.0337500	18.68	0.55	324.4 ± 1.4	< 15
34141	4819197608151426304	78.5500417	-40.0338611	18.00	0.61	321.9 ± 0.6	< 15
28789	4819197608151755648	78.5322083	-40.0339444	17.50	0.74	323.7 ± 0.5	15 ± 2
43811	4819279590484996096	78.6000000	-40.0508333	18.20	0.73	311.5 ± 0.7	< 15
32911	4819197539428458112	78.5457917	-40.0433333	17.84	0.32	322.2 ± 0.8	< 15
24367	4819197470712614272	78.5185833	-40.0595556	17.24	0.13	316.1 ± 1.4	65 ± 5
18643	4819197058394790528	78.4984583	-40.0913333	18.11	0.33	287.8 ± 8.8	147 ± 16
14237	4819196955314217600	78.4785417	-40.0931389	19.69	0.46	318.8 ± 1.6	< 15
10013	4819197951749529600	78.4477917	-40.0700278	18.82	0.44	319.4 ± 1.6	33 ± 7
20558	4819197779951454976	78.5057083	-40.0290278	18.26	0.56	326.8 ± 1.0	< 15
17621	4819197745587678592	78.4943333	-40.0335278	18.46	0.31	315.6 ± 2.8	68 ± 3
15834	4819198501500313216	78.4865417	-40.0183333	18.29	0.25	313.9 ± 1.5	19 ± 3

5.6 Results and discussion

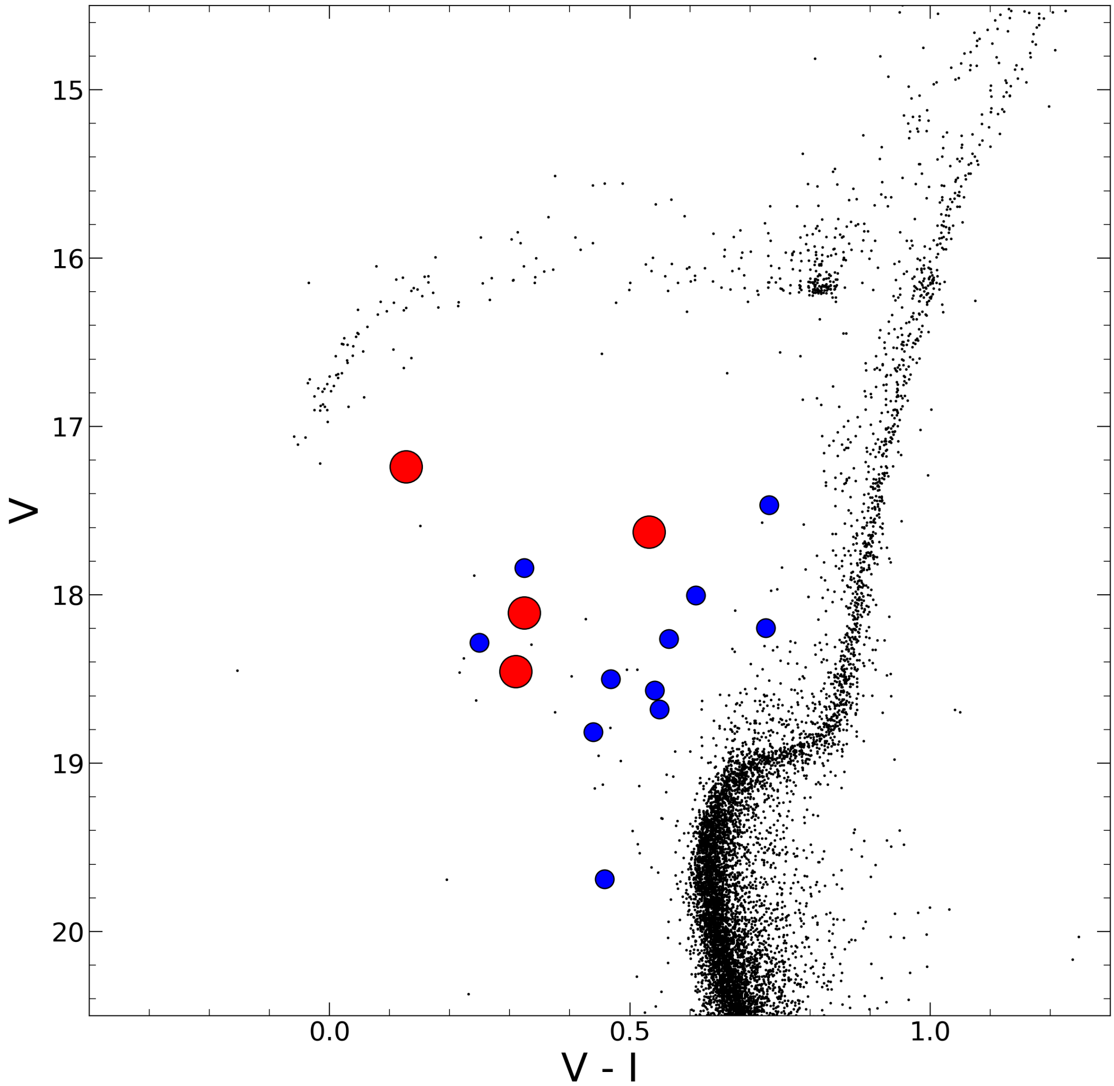

FIGURE 5.6: Optical CMD of NGC 1851 with the position of fast and slowly rotating BSSs analyzed in this work highlighted with red and blue circles, respectively.

As part of a spectroscopic survey of BSS rotational velocities in a sample of Galactic GCs spanning a large range in structural parameters, this work presents the results obtained in NGC 1851. Similar to other clusters, we find that BSSs have a peculiar rotational velocity distribution compared to standard cluster stars, enforcing their "exotic" origin. In particular, BSSs with *v sin(i)* of the order of 100 km s^{-1} or more have been detected in previous works (Lovisi et al., 2010; Mucciarelli et al., 2014; see also Chapters 3 and 4) and one BSS with an extremely high rotational velocity (almost 150 km s^{-1}) is also found in NGC 1851.

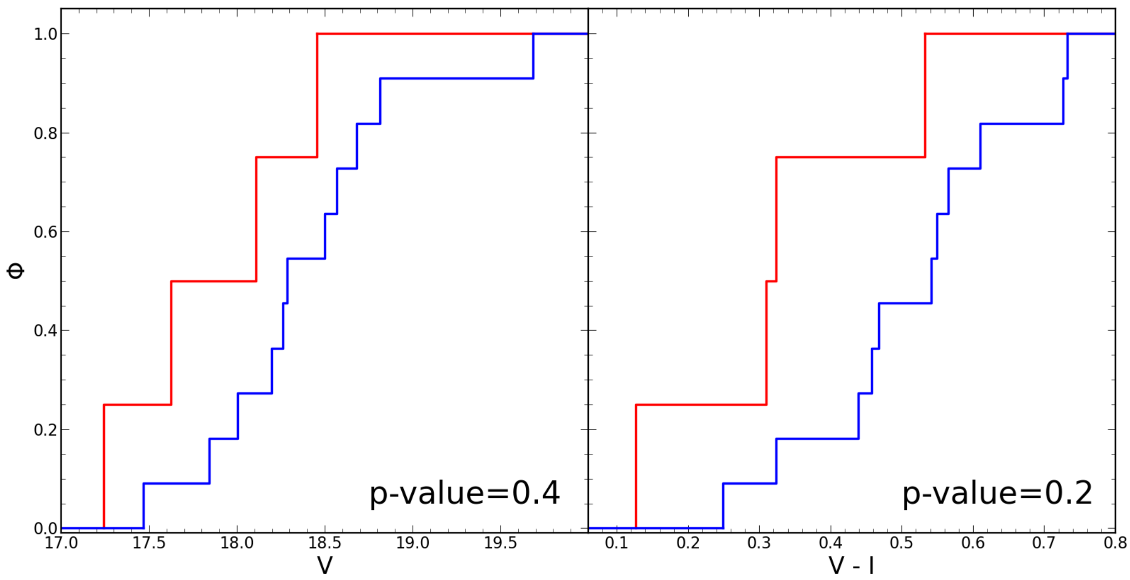

FIGURE 5.7: Cumulative distributions of the V-band magnitude (left panel) and (V−I) color (right panel) for the sample of FR-BSSs (red lines) and slowly rotating BSSs (blue lines). The p-values of the KS test against the null hypothesis that the two samples are extracted from the same parent distribution are marked in each panel.

Figure 5.6 shows the position in the CMD of slowly and fast rotating BSSs, while in Figure 5.7 we plot the cumulative distributions of the two sub-samples as a function of the observed magnitude and color (left and right panels, respectively). Figure 5.7 also provides the p-values of the KS test against the null hypothesis that the two samples are extracted from the same parent distribution. Unfortunately, the small size of the available samples does not allow us to obtain conclusive answers about the possible difference in the color and magnitude distributions of FR and slow-rotating BSSs.

Since a high rotational velocity is interpreted as the evidence of recent BSS formation, with braking mechanisms that had not enough time to intervene and slow down the stars, this piece of evidence might suggest that brighter and bluer BSSs tend to be younger than the others, or that braking mechanisms tends to be less efficient in the former.

We looked also for a possible correlation between the fraction of FR and the distance of the BSSs from the center of the cluster (see Figure 5.8), as done in previous works (see Chapters 3 and 4). In this case we do not find a clear relation between these two parameters. Fast and slow rotating BSSs do not have two distinct radial distributions.

An intriguing relation between fraction of FR-BSSs and the host cluster King concentration is appearing, showing that low-concentration systems are populated by a larger fraction of

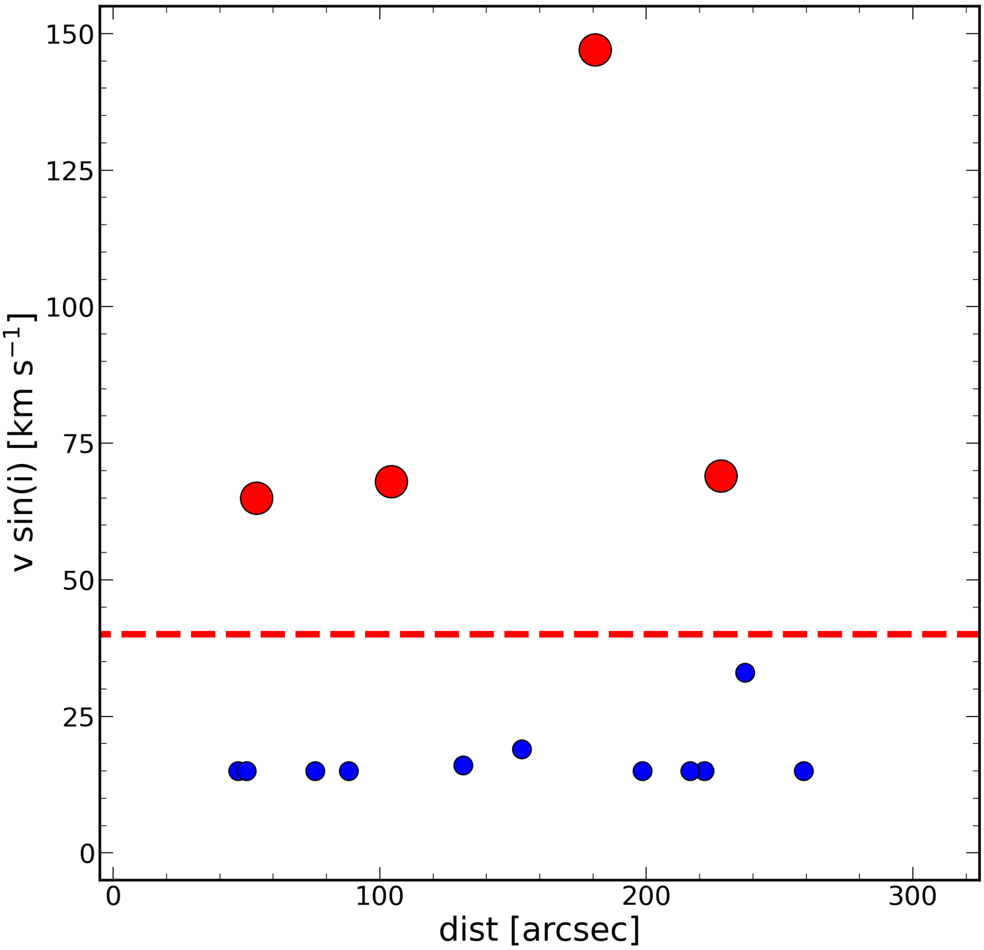

FIGURE 5.8: Fast and slow rotating BSSs represented as red and blue dots, respectively, as a function of the radial distance from the cluster center. The dashed line marks the threshold adopted to distinguish fast-rotating from slowly rotating stars, namely $v\ sin(i) = 40\ km\ s^{-1}$.

fast spinning BSSs (see gray symbols in Figure 5.9). It remained unclear, however, whether such a dependence was either a sort of step function (with $\sim$ 40% FR-BSSs for concentration parameters below $\sim$ 2 and $\sim$ 10% FR-BSSs above this limit), or a monotonically decreasing trend. The finding presented in this work (blue circle in the figure) is an important addition to that result, indicating a continuous drop of the fraction of fast spinning BSSs for increasing King concentration.

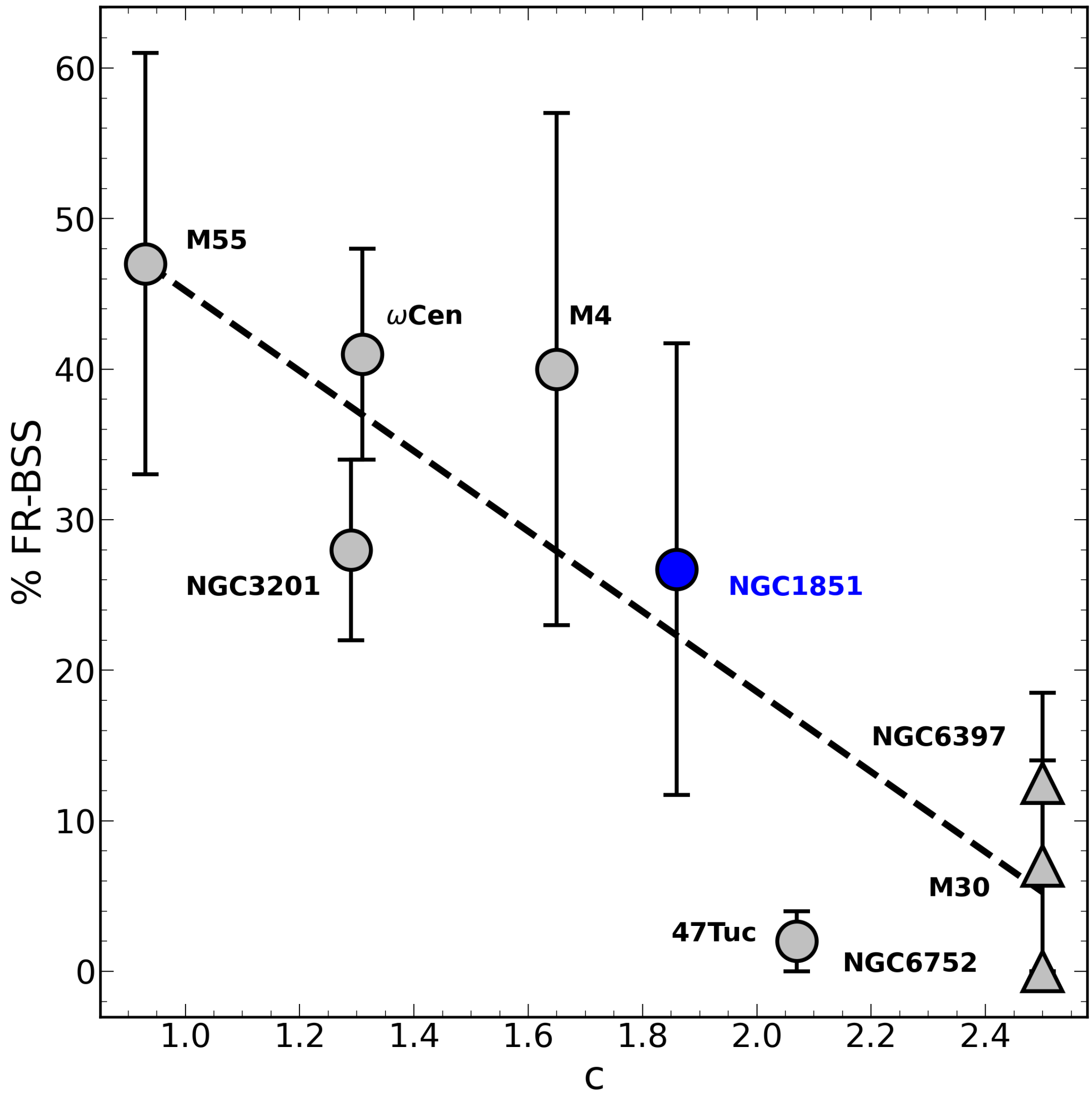

FIGURE 5.9: Percentage of FR-BSSs as a function of the King concentration of the parent cluster. The gray symbols correspond to the GCs investigated in Ferraro et al. (2023a), while the blue circle corresponds to NGC 1851. Triangles represent PCC GCs.

CHAPTER 6

General discussion and conclusions

The three GCs studied in this PhD Thesis were part of a survey of chemical and rotational properties of BSSs in GGCs started two decades ago with the aim to provide new insights into this exotic, and still poorly explored population. The observed sample covers nearly the entire range of values expected for GCs in terms of structural parameters (for instance, the King concentration parameter c varies from 0.8 to 2.5, and the central luminosity density spans $\sim$ 4 orders of magnitude, from $log\ \rho_0 = 2$ to 6 in units of $L_\odot\ pc^{-3}$). Hence, it provides an ideal dataset for exploring possible links between the chemical and rotational properties of BSSs, and the characteristics of their host clusters. For what concerns the rotational velocities, the results obtained for NGC 3201 and M55 (which are fully described in Chapter 3 and Chapter 4) were anticipated in the paper *"Fast rotating blue stragglers prefer loose clusters"* (Ferraro et al., 2023a), where we summarize the overall conclusions of the survey. In this chapter we describe the major findings of that paper, also adding the results obtained for NGC 1851 (which are discussed in detail in Chapter 5).

In Ferraro et al. (2023a) we analyzed the sample of the 320 BSSs measured in 8 GCs. Their rotational velocity distribution is plotted in the top panel of Figure 6.1. As discussed in Chapter 2, in each cluster the spectra of a few normal stars have also been secured with the same observational setups and analyzed with the same procedures. The control sample is made of a few MS-TO stars (about 10% of the total) and, mainly, RGB and SGB stars that are known to show negligible rotation. The distribution of their rotational velocities is plotted in the bottom panel of Figure 6.1: as expected, all the measured values are smaller than 20 $km\ s^{-1}$. The difference between the distributions shown in the two panels is evident: 100% of the reference stars show negligible rotation, while only 54% of the surveyed BSSs have rotation velocities smaller than this value and the remaining 46% of the sample is distributed over a long tail extending toward much larger values, reaching (and, in a few cases even exceeding) 200 $km\ s^{-1}$. The BSS distribution decreases rather smoothly from 20 to 40–50 $km\ s^{-1}$,

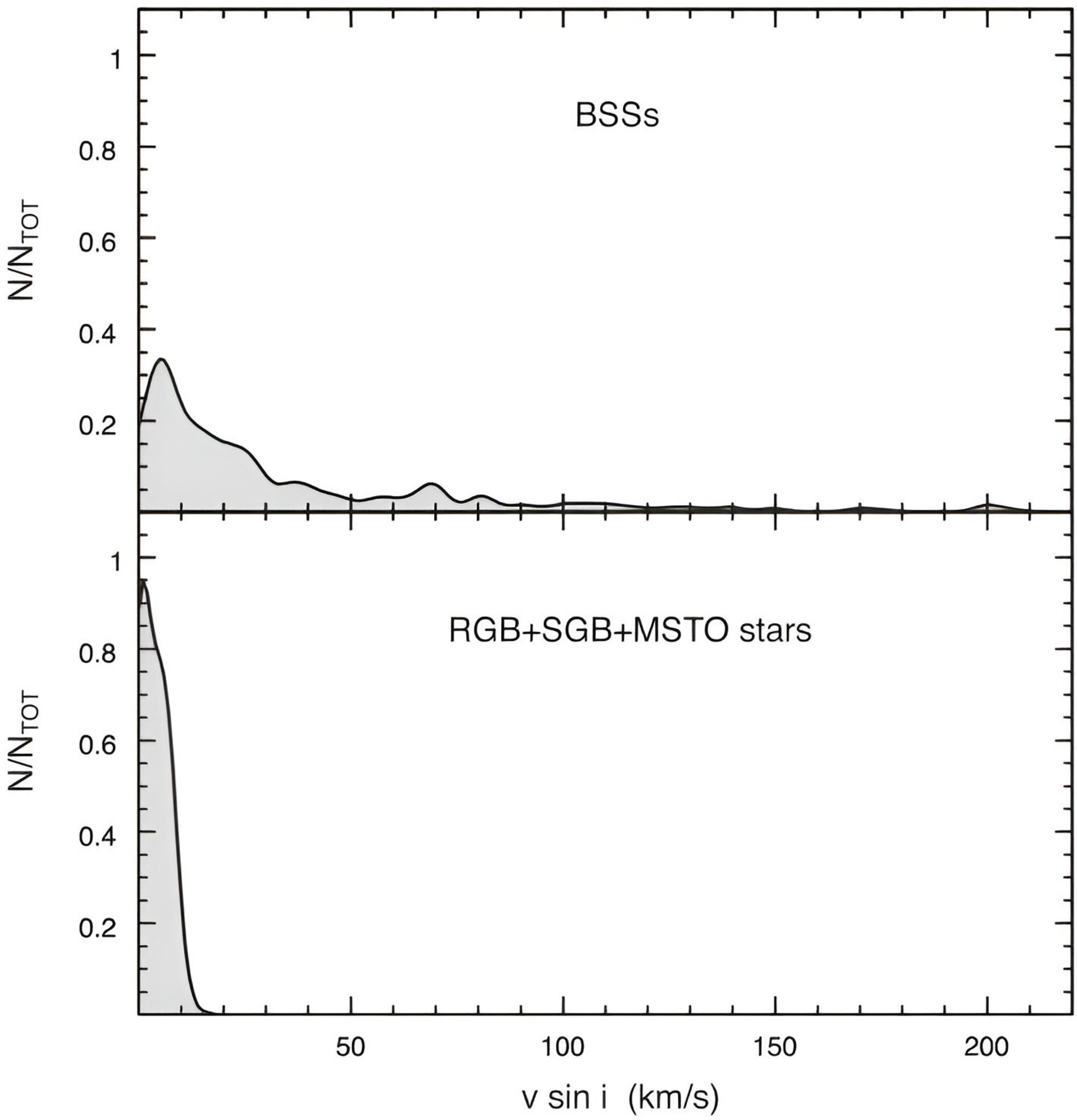

FIGURE 6.1: Kernel-density distributions of the rotational velocities measured for 320 BSSs in the eight surveyed GCs (top panel), compared with that obtained for a sample of 216 RGB, SGB and MS-TO stars (bottom panel). Both distributions are normalized to the total number of stars observed in each sample. Figure taken from Ferraro et al. (2023a).

and a substantial portion of the population, $\sim$ 28%, has rotational velocities larger than 40 $km\ s^{-1}$.

This result confirms, once more, that BSSs are a peculiar sub-population, with properties that deviate from those observed in normal cluster stars. To investigate whether this is the typical distribution of BSS rotational velocities, in Figure 6.2 we plot the results obtained in each surveyed cluster, separately. Although the relatively small number of BSSs observed in each system prevents statistically significant comparisons on a cluster-to-cluster basis, the figure

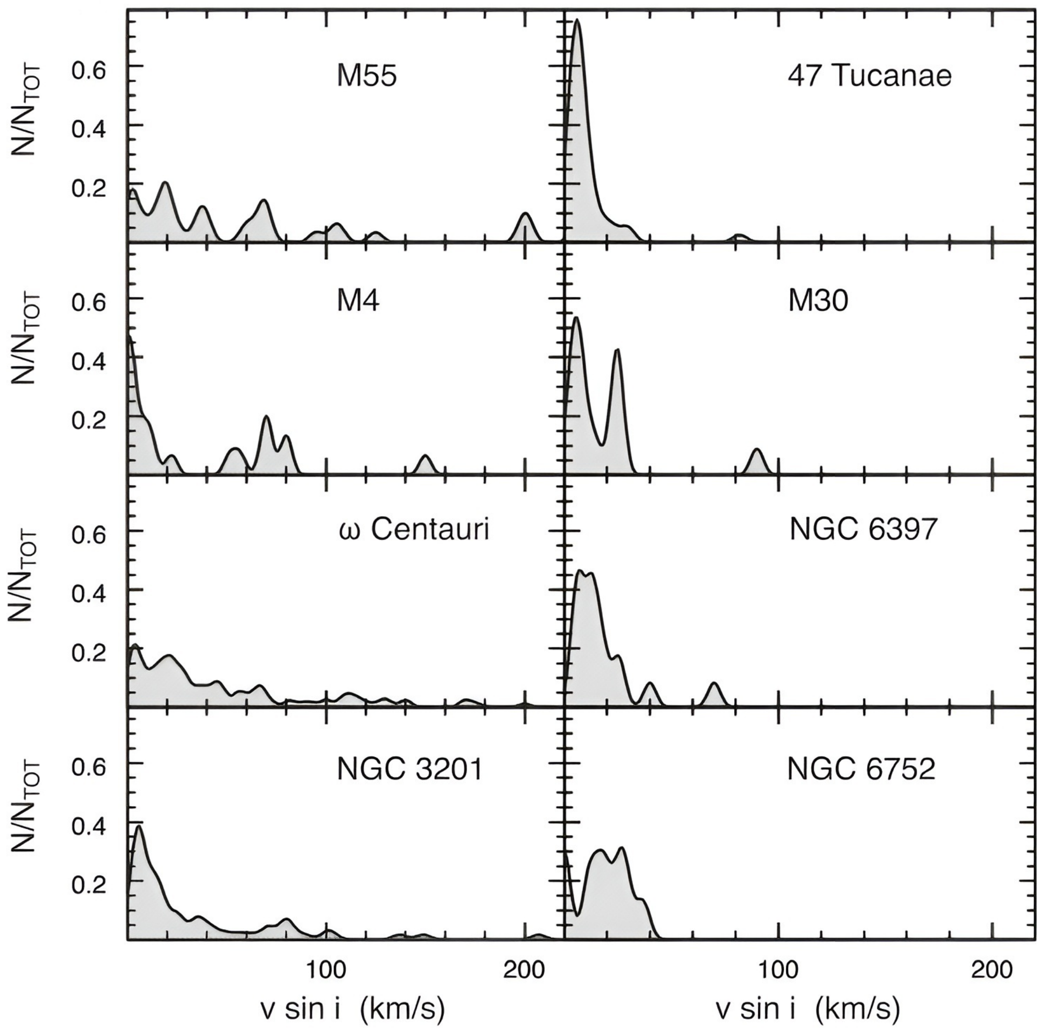

FIGURE 6.2: Kernel-density distributions of the BSS rotational velocities observed in each of the loose and dense clusters, normalized to the total number of BSSs observed in every system. Figure taken from Ferraro et al. (2023a).

shows clear differences in the fraction of FR-BSSs, and it reveals an unexpected, intriguing feature: two separated groups of GCs can be distinguished, one that harbours a modest fraction of FR-BSSs (namely, 47 Tucanae, M30, NGC 6397 and NGC 6752), and another group with a rotational velocity distribution more extended toward large values (including, M55, M4, ω Centauri and NGC 3201), with a few objects spinning even faster than 200 $km\ s^{-1}$. Surprisingly, this cluster classification, based on the distribution of BSS rotational velocities, mirrors the grouping in terms of structural parameters: only low-density (log $\rho_0 < 4$ in units of $L_\odot\ pc^{-3}$) and low concentration ($c < 1.8$) systems show a relevant fraction of FR-BSSs. The effect is even more evident when the rotational velocity distributions of the two groups are directly compared (see top and bottom panels of Figure 6.3a). Undoubtedly, the long tail of the BSS rotational velocity distribution shown in Figure 6.1 is due to loose clusters, while almost the entire (96%) BSS population of high-density systems show rotational velocities smaller than 40 $km\ s^{-1}$. The comparison between the normalized cumulative distributions of rotational velocities shown in the right panel of Figure 6.3 highlights the difference even more: while in high-density clusters, only 4% (4 out of 92) of BSSs spin faster than 40 $km\ s^{-1}$, more than one-third of the population (38%, i.e. 87 out of 228) rotates faster than this value in low-density environments. A KS test quantifies the statistical significance of the difference: the probability that the two distributions are extracted from the same parent family is essentially zero ($\sim 10^{-8}$), which corresponds to a significance level well above 5σ. Thus, the main evidence emerging from this analysis is that the fraction of FR-BSSs appears to be larger in low-density, than in high-density GCs.

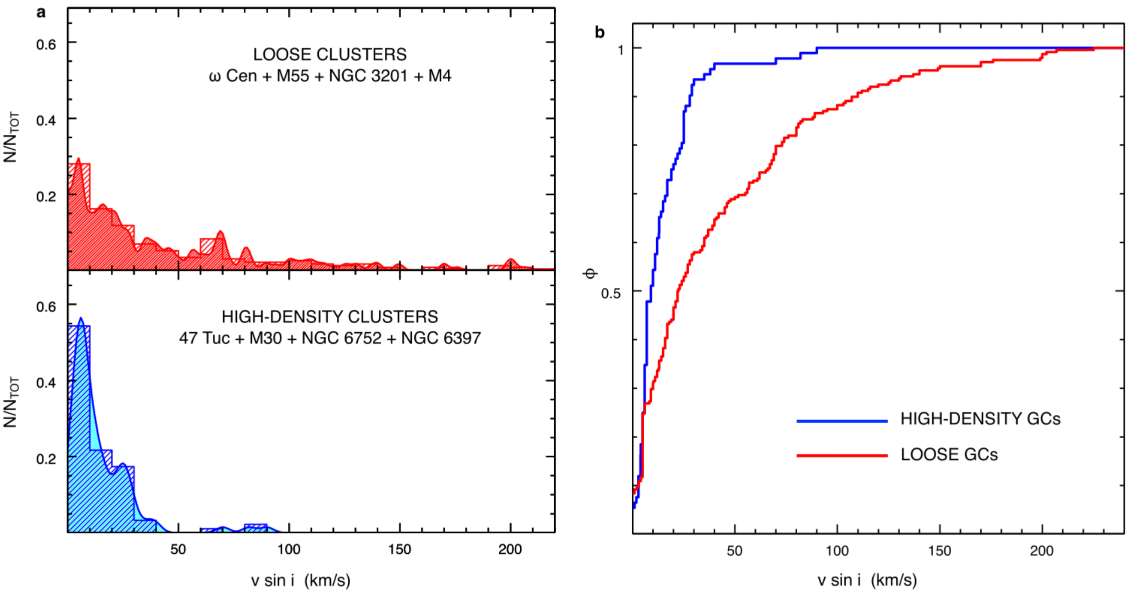

FIGURE 6.3: **a.** BSS rotational velocity distribution for loose clusters, compared to that of high-density clusters, in the top panel (red histogram) and in the bottom panel (blue histogram), respectively. **b.** Comparison between the normalized cumulative distributions of the BSS rotational velocities in low-density (red line) and high-density (blue line) clusters. Figure taken from Ferraro et al. (2023a).

In this respect, NGC 1851, which has an intermediate value of concentration, shows an intermediate distribution (see Figure 5.5): it has a broader distribution with respect to high-concentrated clusters, with four FR-BSSs, but it has also a smaller number of FR-BSSs than low-concentrated clusters.

Figure 6.4 shows the fraction of FR-BSSs as a function of the King concentration and central luminosity density, with the three clusters presented in this Thesis highlighted in blue. As can be seen, there is a strong correlation with the environment: the fraction of FR-BSSs steadily decreases from about 50% to zero for increasing values of both c and $\log \rho_0$. It is

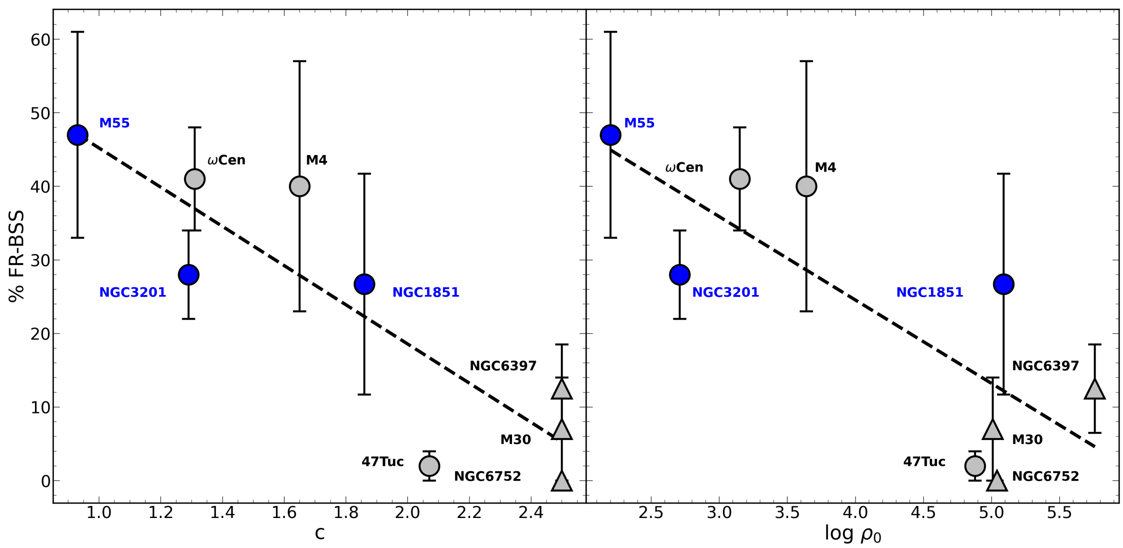

FIGURE 6.4: Percentage of FR-BSSs as a function of the King concentration (left panel) and the central luminosity density (right panel) of the parent clusters. The gray symbols correspond to previously studied clusters, while the blue circles correspond to GCs studied in this Thesis. Triangles represent PCC GCs.

important to emphasize that the assumption of slightly different thresholds for the definition of FR-BSSs has no impact on the results, and similar relations can be obtained even by setting the threshold at 30 or 50 $km\ s^{-1}$. As mentioned in Chapter 1, King models are not a good physical representation of PCC clusters, and a large King concentration parameter ($c = 2.5$) is arbitrarily assumed for these systems (see the gray triangles aligned at $c = 2.5$ in Figure 6.4). However, the conclusion that highly concentrated clusters host a smaller fraction of FR-BSSs is still confirmed by the correlation with ρ_0 (right panel).

From a theoretical point of view, high rotational velocities are expected to be a characteristic feature of recently born BSSs in both the proposed formation scenarios, as the natural effect of angular momentum accretion during mass transfer (Packet, 1981; de Mink et al., 2013), and angular momentum conservation during the contraction phase in the post-collision evolution (e.g., Benz & Hills, 1987; Sarna & De Greve, 1996). Then, a progressive slow down of these stars due to the occurrence of some braking mechanisms (like magnetic braking or disk locking) is predicted, but the efficiencies of these processes are still unknown (Leonard & Livio, 1995; Sills et al., 2005). Following this scenario, a large rotational velocity can be considered as the signature of the early phase of BSS evolution, and the percentage of FRs therefore provides information about the recent BSS formation activity in the host cluster. Therefore, the anti-correlation between the fraction of FR-BSSs (a proxy of new-born BSSs) and the cluster parameters suggests that loose environments are the ideal habitat for newborn highly rotating BSSs.

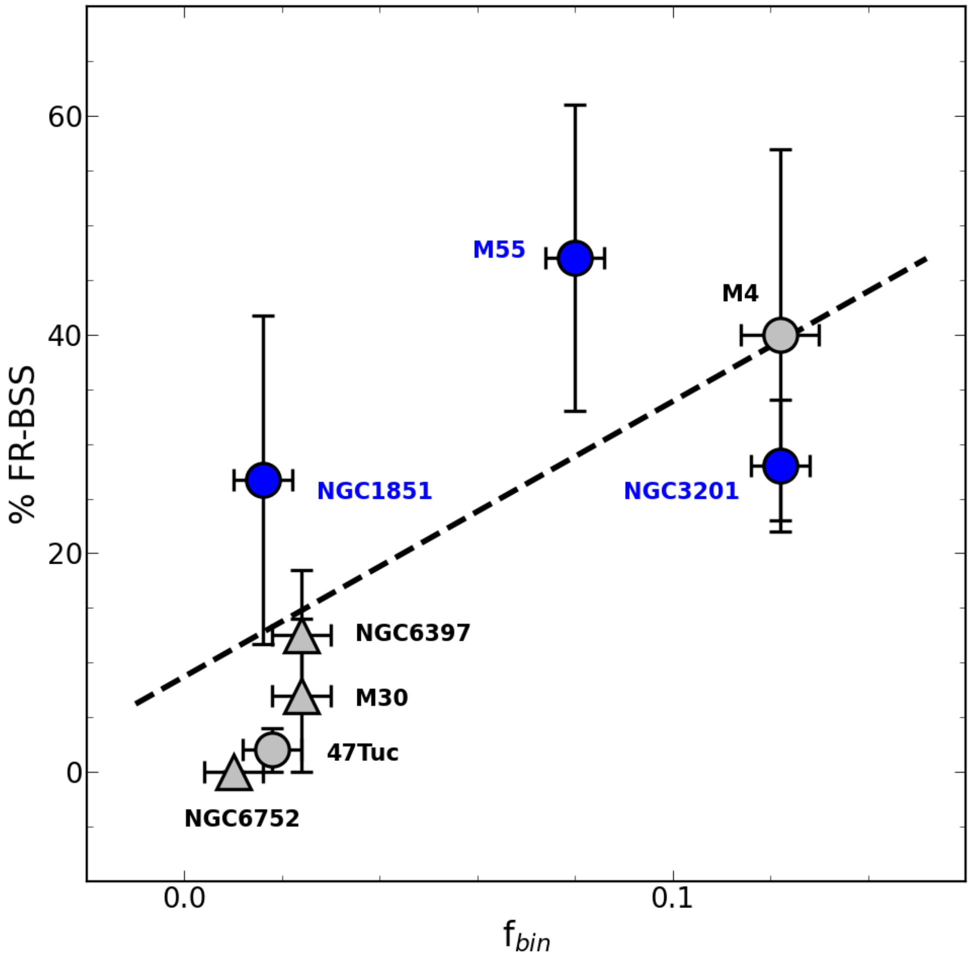

FIGURE 6.5: Percentage of FR-BSSs plotted as a function of the global binary fraction, f_{bin}. ω Centauri is lacking because no reliable estimates of its binary fraction are available in the literature. Errors computed following the Poisson statistics are also reported. The dashed line is the best fit to the data.

The fraction of FR-BSSs has been found to also correlate with the fraction of binaries (see Figure 6.5) that, in turn, decreases for increasing cluster density (see the top panel of Figure 6.6). Intriguingly, the combination of best-fit lines to the $f_{\rm BIN}$ versus $\log \rho_0$ relation and to the $f_{\rm FR} - \log \rho_0$ relation (bottom panel of Figure 6.6) nicely agrees with the best-fit line to $f_{\rm FR}$ versus $f_{\rm BIN}$ (Figure 6.5). Hence, the fact that most of the observed FR-BSSs are found in low-density clusters, where binaries are more abundant, probably is the manifestation of a generation of BSSs originated via MT activity during the secular evolution of primordial binary systems and formed less than 1 Gyr ago (according to tentative estimates of the braking mechanism timescale for MT objects; Leiner et al., 2018).

The paucity of FR-BSSs in high-density clusters, instead, indicates that no relevant recent BSS formation occurred (neither from the mass-transfer, nor from the collisional channel), and/or very effective braking mechanisms are at work.
A lack of newly born MT-BSSs in high-density conditions is somehow surprising, because the MT scenario is expected to be active also in those environments. The explanation likely is in the fact that the fraction of binaries (hence, of their by-products as well) is smaller in high-density clusters, maybe because of a destructive action of stellar interactions. Indeed, a clear anti-correlation has been found also between the fraction of FR-BSSs and the collisional parameter Γ_{coll} (see Figure 6.7), that measures the overall level of collisionality of the system. The collisional parameter is defined as follows:

$$\Gamma_{coll} \propto \frac{\rho_0^2 r_c^3}{\sigma} \tag{6.1}$$

where ρ_0 is the central mass density, r_c is the core radius, and σ is the velocity dispersion. For virialized systems that follow the King model the expression of this parameter simplifies in:

$$\Gamma_{coll} \propto \rho_0^{1.5} r_c^2 \tag{6.2}$$

This is consistent with what showed before in terms of density. This parameter is directly proportional to the density of the clusters. Hence, high-density clusters have a higher value of the collisional parameter. This tells us that in high-density systems there are a lot more collisions between stars than in low-density environments. In turn, this might produce a destructive action of binary systems, which could explain the trend between $f_{\rm BIN}$ and $\log \rho_0$ observed in Figure 6.6 and, therefore, a paucity of newly born (fast spinning) MT-BSSs in these systems. However, in high-density conditions the COL channel should be much more efficient than MT, with tens of BSSs expected to form during the last Gyr in the clusters with the highest collision rates (Davies et al., 2004). The observed paucity of FR-BSSs, therefore, indicates that braking mechanisms should be highly efficient in these environments. Such an unknown spin-down mechanism might be linked to the intrinsic nature and structure of these objects (formed through collisions instead of mass-transfer) or depend on the local density.
An anti-correlation has been also found between the fraction of FR-BSSs and the A^+ parameter (see Figure 6.8), which quantifies the level of BSS central segregation due to the dynamical aging of the host stellar system (see Section 1.2.5). This relation suggests that the fraction of FR-BSSs also depends on the internal dynamics of the host cluster. In particular two trends are observed. The first one, consistently with what discussed above, suggests that the fraction of FR-BSSs decreases with the increasing internal dynamical activity (traced by increasing

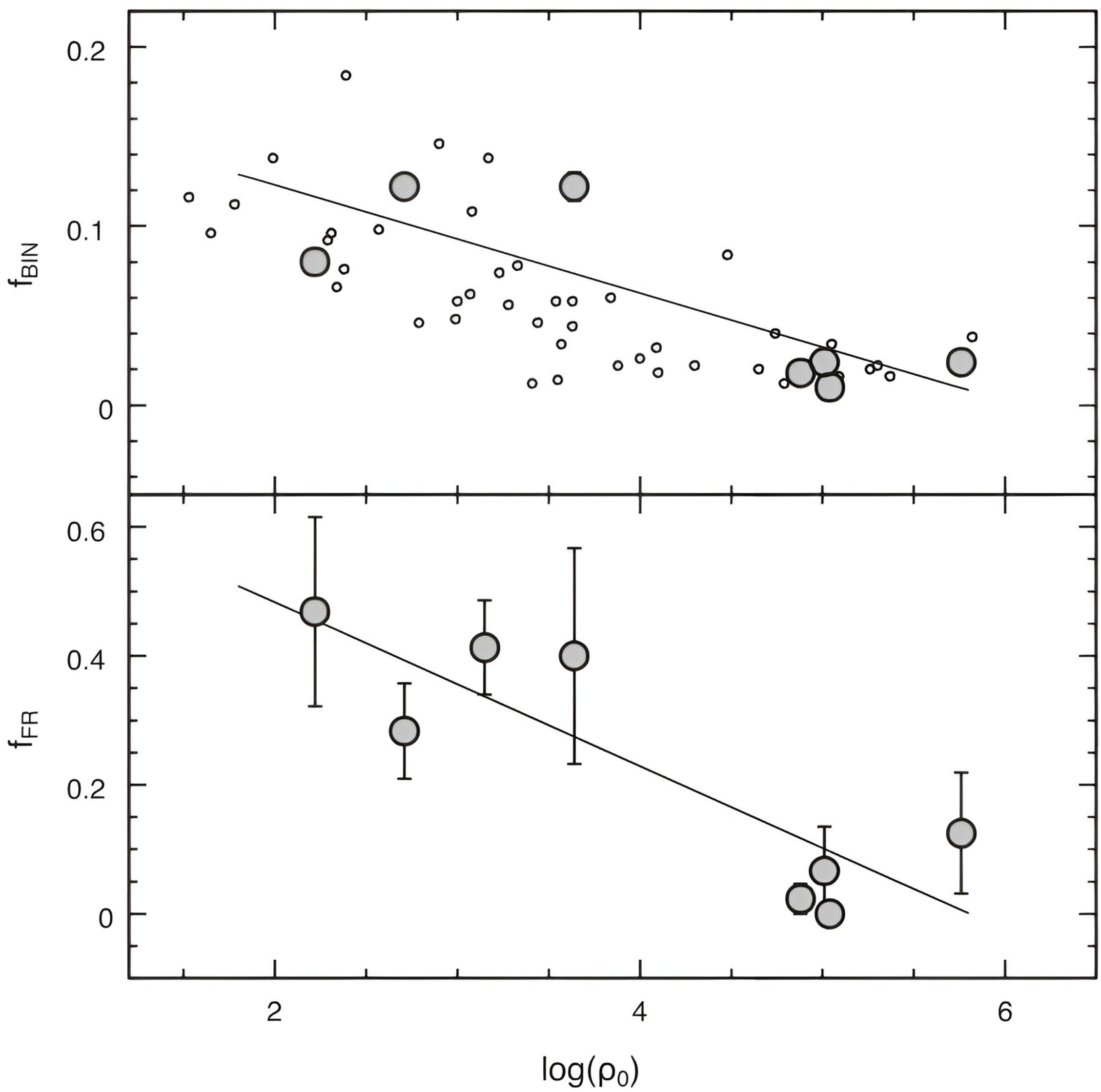

FIGURE 6.6: The relations linking the fraction of binaries f_{bin} (gray circles in the top panel) and the fraction of FR-BSSs f_{FR} (gray circles in the bottom panel) to the cluster central density. The small empty circles in the top panel are the data for a sample of 59 GGCs. The solid lines are the best linear fits to the data. Figure taken from Ferraro et al. (2023a).

values of A^+_{rh}). In particular, dynamically younger clusters (low values of A^+_{rh}) have a higher fraction of FR-BSSs. This is consistent with the hypothesis that low-density environments favor the birth of (highly spinning) BSSs through the evolution of primordial binary systems. With increasing values of the A^+_{rh} parameter a second trend emerges. For $A^+_{rh} > 0.3$ the fraction of FR-BSSs slightly increases with this parameter. This modest increase might testify the presence of recently formed COL-BSSs, generated by the strong density enhancement (hence, the growth in the stellar collision probability) occurred during CC (in fact, $A^+_{rh} = 0.3$ has been suggested to be the threshold between pre- and post-core collapse systems; see Ferraro

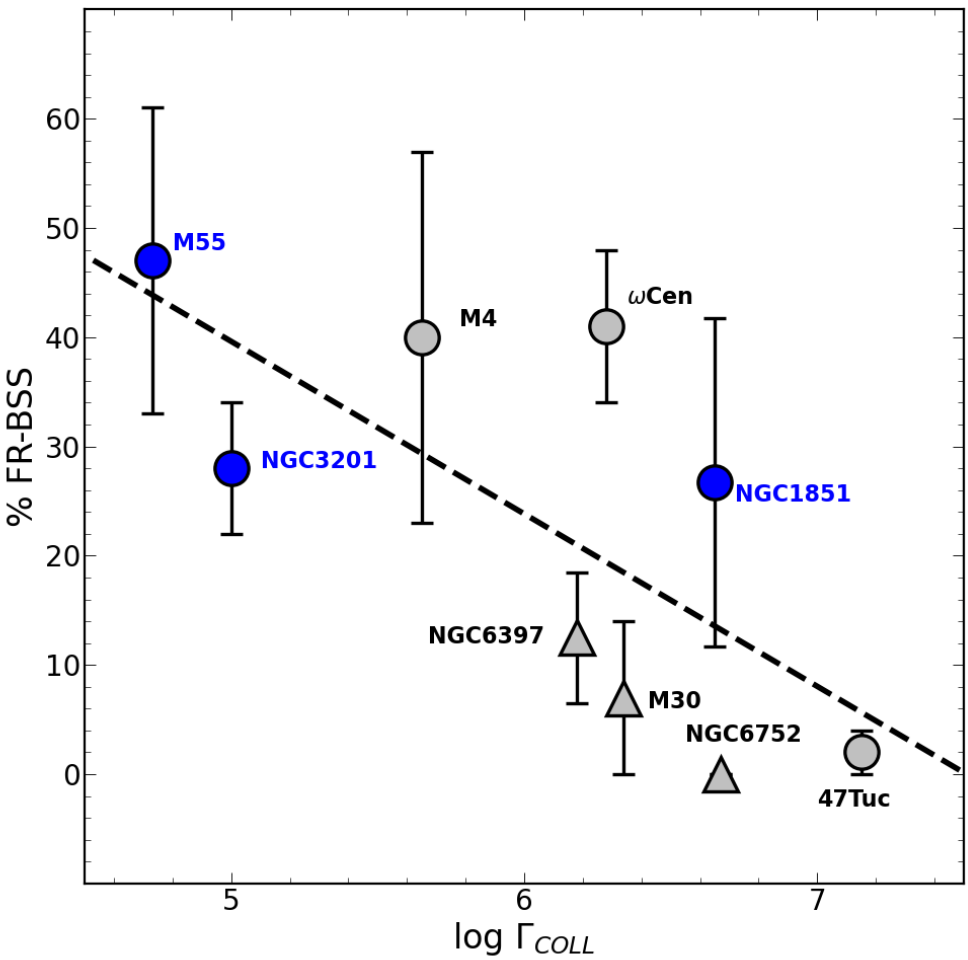

FIGURE 6.7: Percentage of FR-BSSs plotted as a function of the collisional parameter (Γ_{coll}) in arbitrary units.

et al., 2023a). For NGC 1851 the fraction is a bit higher than what expected. The large error bar, however, leaves open the possibility that the fraction of FR-BSSs increases as a function of A^+_{rh} in highly dynamically evolved systems. It is also worth mentioning that, in spite of its large value of the A^+_{rh} parameter ($A^+_{rh} = 0.48$, Ferraro et al., 2018a), NGC 1851 is not classified as a PCC system. We thus speculate that the observed large percentage of FR-BSSs might testify recent BSS formation due to a large rate of binary interactions, which are also delaying the CC phase. Indeed, another possible clue of high rate of binary interactions in NGC 1851 is suggested by the presence of a relevant number of isolated millisecond pulsars and binaries that were likely formed via exchange interactions (Ridolfi et al., 2022; Barr et al., 2024; Dutta

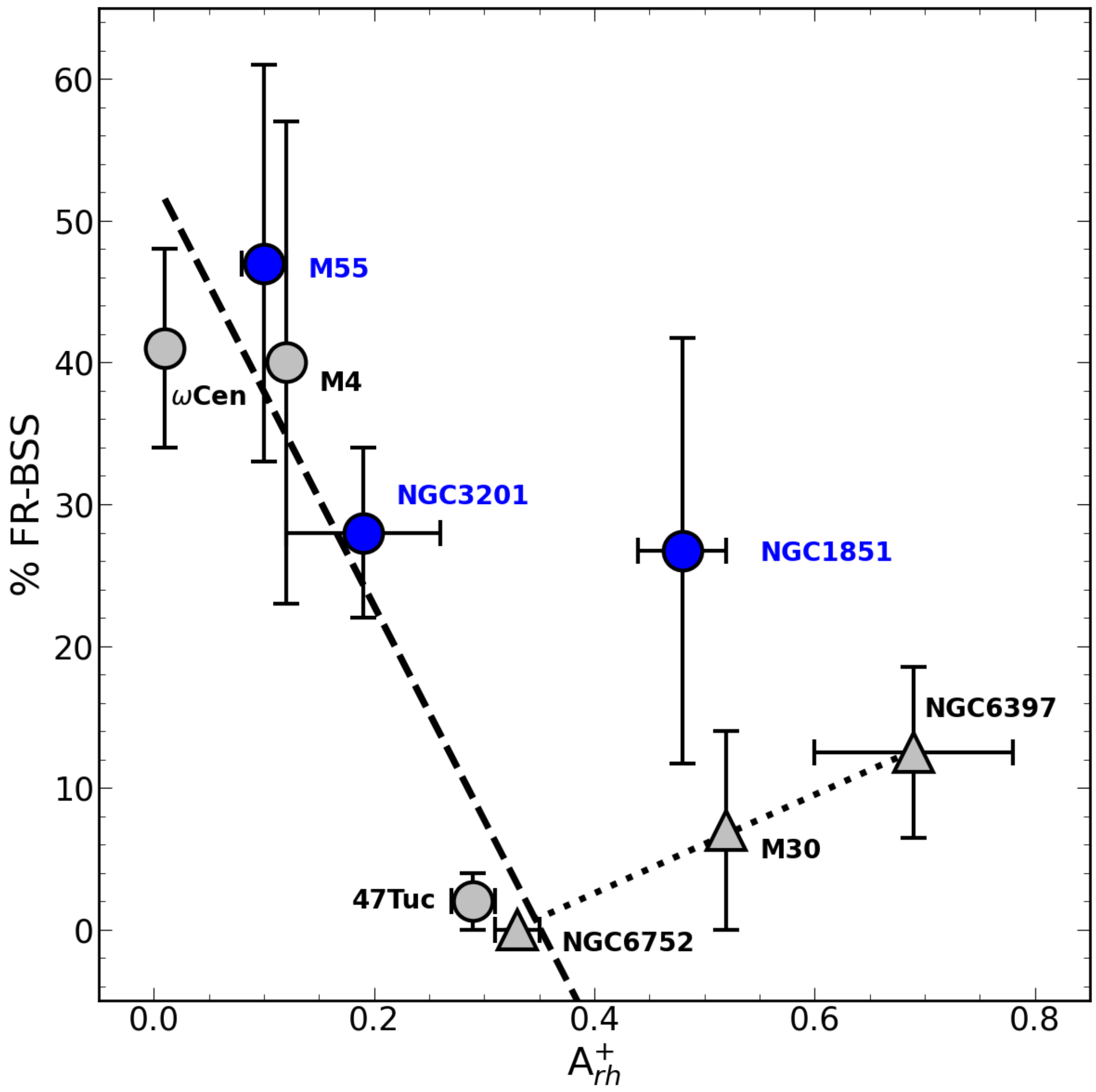

FIGURE 6.8: Percentage of FR-BSSs as a function of the A^+_{rh} parameter, which is a tracer of internal dynamical evolution of the host cluster.

et al., 2025).

In conclusion, despite the need of more data, the observed trends, especially those between the percentage of FR-BSSs and the King concentration and central density of the parent cluster, are quite solid and, therefore, suggest the necessity of renewed theoretical modeling of BSS formation through both collisions and MT in different environmental conditions. In fact, this would finally provide a physical explanation to these intriguing observational results and shed new light on the role of environment and internal dynamics in setting the BSS properties.

6.1 Future perspectives

Unfortunately, the conclusions obtained so far need for further observational studies of large sample of BSSs in clusters with different characteristics. In particular, extending this study to extremely low-density systems, such as OCs, will be crucial. Thanks to their relatively small distances and bright TO magnitudes, BSSs in OCs represent ideal targets for detailed future investigations. Additionally, in such low-density environments the role of collisions is totally negligible, and essentially pure samples of MT-BSSs are expected. Moreover, stellar densities are so small that Gaia photometry is 100% complete in the magnitude range spanned by BSSs, thus allowing a solid assessment of BSS cluster membership through proper motions. If the picture designed above is correct, we expect a fraction of FR-BSSs larger than 50% in OCs. Hence, such data would provide the ideal platform to perform the empirical calibration of MT-BSS gyro-chronology, by combining the formation age of each BSS with its rotational velocity. In fact, theoretical MT models (Jiang et al., 2017) show that newly formed MT-BSSs start their evolution very close to the zero-age MS of the cluster. Thus, the comparison between the CMD position of the observed BSSs and theoretical evolutionary tracks can provide a first-guess measure of the time elapsed since the BSS formation. The formation age combined with the measured rotational velocity would finally provide an empirical measure of the braking timescale for MT-BSSs.

Bibliography

Alessandrini E., Lanzoni B., Ferraro F. R., Miocchi P., Vesperini E., 2016, "Investigating the Mass Segregation Process in Globular Clusters with Blue Straggler Stars: The Impact of Dark Remnants" ApJ, 833, 252 (arXiv:1610.04562)

Andronov N., Pinsonneault M. H., Terndrup D. M., 2006, "Mergers of Close Primordial Binaries" ApJ, 646, 1160 (arXiv:astro-ph/0509309)

Barr E. D., et al., 2024, "A pulsar in a binary with a compact object in the mass gap between neutron stars and black holes" Science, 383, 275 (arXiv:2401.09872)

Baumgardt H., Hilker M., 2018, "A catalogue of masses, structural parameters, and velocity dispersion profiles of 112 Milky Way globular clusters" MNRAS, 478, 1520 (arXiv:1804.08359)

Baumgardt H., Heggie D. C., Hut P., Makino J., 2003, "Parameters of core collapse" MNRAS, 341, 247 (arXiv:astro-ph/0301166)

Beccari G., et al., 2019, "Discovery of a Double Blue Straggler Sequence in M15: New Insight into the Core-collapse Process" ApJ, 876, 87 (arXiv:1903.11113)

Behr B. B., 2003, "Chemical Abundances and Rotation Velocities of Blue Horizontal-Branch Stars in Six Globular Clusters" ApJS, 149, 67 (arXiv:astro-ph/0307178)

Behr B. B., Djorgovski S. G., Cohen J. G., McCarthy J. K., Côté P., Piotto G., Zoccali M., 2000a, "A New Spin on the Problem of Horizontal-Branch Gaps: Stellar Rotation along the Blue Horizontal Branch of Globular Cluster M13" ApJ, 528, 849 (arXiv:astro-ph/9907211)

Behr B. B., Cohen J. G., McCarthy J. K., 2000b, "Rotations and Abundances of Blue Horizontal-Branch Stars in Globular Cluster M15" ApJ, 531, L37 (arXiv:astro-ph/0002119)

Bekki K., Freeman K. C., 2003, "Formation of ω Centauri from an ancient nucleated dwarf galaxy in the young Galactic disc" MNRAS, 346, L11 (arXiv:astro-ph/0310348)

Benz W., Hills J. G., 1987, "Three-dimensional Hydrodynamical Simulations of Stellar Collisions. I. Equal-Mass Main-Sequence Stars" ApJ, 323, 614

Billi A., et al., 2023, "Fast-rotating Blue Straggler Stars in the Globular Cluster NGC 3201" ApJ, 956, 124 (arXiv:2309.01442)

Billi A., Ferraro F. R., Mucciarelli A., Lanzoni B., Cadelano M., Monaco L., 2024, "Rotational velocities of blue straggler stars in the globular cluster M 55" A&A, 690, A156 (arXiv:2408.07620)

Billi A., Monaco L., Ferraro F. R., Mucciarelli A., Lanzoni B., Cadelano M., Trangolao I., 2026, "Fast-rotating blue straggler stars in the globular cluster NGC 1851" A&A, 705, A36

Burbidge E. M., Sandage A., 1958, "The Color-Magnitude Diagram for the Galactic NGC 7789." ApJ, 128, 174

Busso M., Gallino R., Wasserburg G. J., 1999, "Nucleosynthesis in Asymptotic Giant Branch Stars: Relevance for Galactic Enrichment and Solar System Formation" ARA&A, 37, 239

Cadelano M., Saracino S., Dalessandro E., Ferraro F. R., Lanzoni B., Massari D., Pallanca C., Salaris M., 2020, "Digging for Relics of the Past: The Ancient and Obscured Bulge Globular Cluster NGC 6256" ApJ, 895, 54 (arXiv:2004.06131)

Cadelano M., Ferraro F. R., Dalessandro E., Lanzoni B., Pallanca C., Saracino S., 2022, "Discovery of a Double Sequence of Blue Straggler Stars in the Core-collapsed Globular Cluster NGC 6256" ApJ, 941, 69 (arXiv:2211.02671)

Cadelano M., Dalessandro E., Vesperini E., 2024, "The structural properties of multiple populations in globular clusters: The instructive case of NGC 3201" A&A, 685, A158 (arXiv:2402.09514)

Carney B. W., Latham D. W., Laird J. B., Grant C. E., Morse J. A., 2001, "A Survey of Proper-Motion Stars. XIV. Spectroscopic Binaries among Metal-poor Field Blue Stragglers" AJ, 122, 3419

Carraro G., Vázquez R. A., Moitinho A., 2008, "Blue straggler stars in Galactic open clusters and the effect of field star contamination" A&A, 482, 777 (arXiv:0802.3557)

Carretta E., et al., 2009a, "Na-O anticorrelation and HB. VII. The chemical composition of first and second-generation stars in 15 globular clusters from GIRAFFE spectra" A&A, 505, 117 (arXiv:0909.2938)

Carretta E., Bragaglia A., Gratton R., Lucatello S., 2009b, "Na-O anticorrelation and HB. VIII. Proton-capture elements and metallicities in 17 globular clusters from UVES spectra" A&A, 505, 139 (arXiv:0909.2941)

Castelli F., Kurucz R. L., 2003, in Piskunov N., Weiss W. W., Gray D. F., eds, IAU Symposium Vol. 210, Modelling of Stellar Atmospheres. p. A20 (arXiv:astro-ph/0405087), doi:10.48550/arXiv.astro-ph/0405087

Castelli F., Gratton R. G., Kurucz R. L., 1997, "Notes on the convection in the ATLAS9 model atmospheres." A&A, 318, 841

Chaboyer B., Demarque P., Kernan P. J., Krauss L. M., 1998, "The Age of Globular Clusters in Light of Hipparcos: Resolving the Age Problem?" ApJ, 494, 96 (arXiv:astro-ph/9706128)

Chatterjee S., Rasio F. A., Sills A., Glebbeek E., 2013, "Stellar Collisions and Blue Straggler Stars in Dense Globular Clusters" ApJ, 777, 106 (arXiv:1302.7284)

Clarkson W. I., et al., 2011, "The First Detection of Blue Straggler Stars in the Milky Way Bulge" ApJ, 735, 37 (arXiv:1105.4176)

Contreras Ramos R., Ferraro F. R., Dalessandro E., Lanzoni B., Rood R. T., 2012, "The Unimodal Distribution of Blue Straggler Stars in M75 (NGC 6864)" ApJ, 748, 91 (arXiv:1201.4959)

Cordoni G., et al., 2023, "Photometric binaries, mass functions, and structural parameters of 78 Galactic open clusters" A&A, 672, A29 (arXiv:2302.03685)

Cortés C., Silva J. R. P., Recio-Blanco A., Catelan M., Do Nascimento Jr. J. D., De Medeiros J. R., 2009, "An Overview of the Rotational Behavior of Metal-poor Stars" ApJ, 704, 750 (arXiv:1009.4951)

Crociati C., et al., 2023, "First Evidence of Multi-iron Subpopulations in the Bulge Fossil Fragment Candidate Liller 1" ApJ, 951, 17 (arXiv:2305.04595)

Dalessandro E., Lanzoni B., Ferraro F. R., Vespe F., Bellazzini M., Rood R. T., 2008, "Another Nonsegregated Blue Straggler Population in a Globular Cluster: the Case of NGC 2419" ApJ, 681, 311 (arXiv:0803.2149)

Dalessandro E., et al., 2013, "Double Blue Straggler Sequences in Globular Clusters: The Case of NGC 362" ApJ, 778, 135 (arXiv:1310.2389)

Davies M. B., Piotto G., de Angeli F., 2004, "Blue straggler production in globular clusters" MNRAS, 349, 129 (arXiv:astro-ph/0401502)

De Medeiros J. R., Alves S., Udry S., Andersen J., Nordström B., Mayor M., 2014, "A catalog of rotational and radial velocities for evolved stars. V. Southern stars" A&A, 561, A126 (arXiv:1312.3474)

Deras D., Cadelano M., Ferraro F. R., Lanzoni B., Pallanca C., 2023, "Digging into the Galactic Bulge: Stellar Population and Structure of the Poorly Studied Cluster NGC 6316" ApJ, 942, 104 (arXiv:2212.03649)

Djorgovski S., King I. R., 1984, "Surface photometry in cores of globular clusters." ApJ, 277, L49

Dresbach F., Massari D., Lanzoni B., Ferraro F. R., Dalessandro E., Raso S., Bellini A., Libralato M., 2022, "Blue Stragglers as Tracers of the Dynamical State of Two Clusters in the Small Magellanic Cloud: NGC 339 and NGC 419" ApJ, 928, 47 (arXiv:2202.07677)

Dutta A., et al., 2025, "NGC 1851A: Revealing an ongoing three-body encounter in a dense globular cluster" A&A, 697, A166 (arXiv:2503.05466)

Ferraro F. R., Pecci F. F., Cacciari C., Corsi C., Buonanno R., Fahlman G. G., Richer H. B., 1993, "Blue Stragglers in the Galactic Globular Cluster M3: Evidence for two Populations" AJ, 106, 2324

Ferraro F. R., Carretta E., Corsi C. E., Fusi Pecci F., Cacciari C., Buonanno R., Paltrinieri B., Hamilton D., 1997, "The stellar population of the globular cluster M 3. II. CCD photometry of additional 10,000 stars." A&A, 320, 757 (arXiv:astro-ph/9611016)

Ferraro F. R., Paltrinieri B., Rood R. T., Dorman B., 1999, "Blue Straggler Stars: The Spectacular Population in M80" ApJ, 522, 983 (arXiv:astro-ph/9904196)

Ferraro F. R., Sills A., Rood R. T., Paltrinieri B., Buonanno R., 2003, "Blue Straggler Stars: A Direct Comparison of

Star Counts and Population Ratios in Six Galactic Globular Clusters" ApJ, 588, 464 (arXiv:astro-ph/0301261)
Ferraro F. R., Beccari G., Rood R. T., Bellazzini M., Sills A., Sabbi E., 2004, "Discovery of Another Peculiar Radial Distribution of Blue Stragglers in Globular Clusters: The Case of 47 Tucanae" ApJ, 603, 127 (arXiv:astro-ph/0311317)
Ferraro F. R., Sollima A., Rood R. T., Origlia L., Pancino E., Bellazzini M., 2006a, "The Pure Noncollisional Blue Straggler Population in the Giant Stellar System ω Centauri" ApJ, 638, 433 (arXiv:astro-ph/0510280)
Ferraro F. R., et al., 2006b, "Discovery of Carbon/Oxygen-depleted Blue Straggler Stars in 47 Tucanae: The Chemical Signature of a Mass Transfer Formation Process" ApJ, 647, L53 (arXiv:astro-ph/0610081)
Ferraro F. R., et al., 2009, "Two distinct sequences of blue straggler stars in the globular cluster M 30" Nature, 462, 1028 (arXiv:1001.1096)
Ferraro F. R., et al., 2012, "Dynamical age differences among coeval star clusters as revealed by blue stragglers" Nature, 492, 393 (arXiv:1212.5071)
Ferraro F. R., Lanzoni B., Dalessandro E., Mucciarelli A., Lovisi L., 2015, in Boffin H. M. J., Carraro G., Beccari G., eds, Astrophysics and Space Science Library Vol. 413, Astrophysics and Space Science Library. p. 99 (arXiv:1406.3471), doi:10.1007/978-3-662-44434-4_5
Ferraro F. R., et al., 2018a, "The Hubble Space Telescope UV Legacy Survey of Galactic Globular Clusters. XV. The Dynamical Clock: Reading Cluster Dynamical Evolution from the Segregation Level of Blue Straggler Stars" ApJ, 860, 36 (arXiv:1805.00968)
Ferraro F. R., et al., 2018b, "MIKiS: The Multi-instrument Kinematic Survey of Galactic Globular Clusters. I. Velocity Dispersion Profiles and Rotation Signals of 11 Globular Clusters" ApJ, 860, 50 (arXiv:1804.08618)
Ferraro F. R., Lanzoni B., Dalessandro E., Cadelano M., Raso S., Mucciarelli A., Beccari G., Pallanca C., 2019, "Size diversity of old Large Magellanic Cloud clusters as determined by internal dynamical evolution" Nature Astronomy, 3, 1149 (arXiv:1909.02049)
Ferraro F. R., Lanzoni B., Dalessandro E., 2020, "The "dynamical clock": dating the internal dynamical evolution of star clusters with Blue Straggler Stars" Rendiconti Lincei. Scienze Fisiche e Naturali, 31, 19 (arXiv:2001.07435)
Ferraro F. R., et al., 2023a, "Fast rotating blue stragglers prefer loose clusters" Nature Communications, 14, 2584 (arXiv:2305.08478)
Ferraro F. R., Lanzoni B., Vesperini E., Cadelano M., Deras D., Pallanca C., 2023b, "Empirical Measurement of the Dynamical Ages of Three Globular Clusters and Some Considerations on the Use of the Dynamical Clock" ApJ, 950, 145 (arXiv:2304.08140)
Ferraro F. R., et al., 2025, "The Bulge Cluster Origin (BulCO) survey at the ESO-VLT: Probing the early history of the Milky Way assembly. Design and first results in Liller 1" A&A, 696, A179 (arXiv:2503.14642)
Ferraro F. R., et al., 2026, "A binary-related origin mediated by environmental conditions for blue straggler stars" Nature Communications, 17, 768
Fiorentino G., Lanzoni B., Dalessandro E., Ferraro F. R., Bono G., Marconi M., 2014, "Blue Straggler Masses from Pulsation Properties. I. The Case of NGC 6541" ApJ, 783, 34 (arXiv:1312.0388)
Gaia Collaboration et al., 2016, "Gaia Data Release 1. Summary of the astrometric, photometric, and survey properties" A&A, 595, A2 (arXiv:1609.04172)
Gaia Collaboration et al., 2023, "Gaia Data Release 3. Summary of the content and survey properties" A&A, 674, A1 (arXiv:2208.00211)
Gallet F., Bouvier J., 2015, "Improved angular momentum evolution model for solar-like stars. II. Exploring the mass dependence" A&A, 577, A98 (arXiv:1502.05801)
Geller A. M., Mathieu R. D., 2011, "A mass transfer origin for blue stragglers in NGC 188 as revealed by half-solar-mass companions" Nature, 478, 356 (arXiv:1110.3793)
Geller A. M., Mathieu R. D., 2012, "WIYN Open Cluster Study. XLVIII. The Hard-binary Population of NGC 188" AJ, 144, 54 (arXiv:1111.3950)
Geller A. M., Latham D. W., Mathieu R. D., 2015, "Stellar Radial Velocities in the Old Open Cluster M67 (NGC 2682). I. Memberships, Binaries, and Kinematics" AJ, 150, 97 (arXiv:1507.01949)
Gosnell N. M., Mathieu R. D., Geller A. M., Sills A., Leigh N., Knigge C., 2014, "Detection of White Dwarf Companions to Blue Stragglers in the Open Cluster NGC 188: Direct Evidence for Recent Mass Transfer" ApJ, 783, L8 (arXiv:1401.7670)
Gosnell N. M., Mathieu R. D., Geller A. M., Sills A., Leigh N., Knigge C., 2015, "Implications for the Formation of

Blue Straggler Stars from HST Ultraviolet Observations of NGC 188" ApJ, 814, 163 (arXiv:1510.04290)
Gratton R. G., Fusi Pecci F., Carretta E., Clementini G., Corsi C. E., Lattanzi M., 1997, "Ages of Globular Clusters from HIPPARCOS Parallaxes of Local Subdwarfs" ApJ, 491, 749 (arXiv:astro-ph/9704150)
Gratton R., Sneden C., Carretta E., 2004, "Abundance Variations Within Globular Clusters" ARA&A, 42, 385
Gratton R. G., Carretta E., Bragaglia A., 2012, "Multiple populations in globular clusters. Lessons learned from the Milky Way globular clusters" A&A Rev., 20, 50 (arXiv:1201.6526)
Harris W. E., 1996, "A Catalog of Parameters for Globular Clusters in the Milky Way" AJ, 112, 1487
Hénon M., 1961, "Sur l'évolution dynamique des amas globulaires" Annales d'Astrophysique, 24, 369
Hills J. G., Day C. A., 1976, "Stellar Collisions in Globular Clusters" Astrophys. Lett., 17, 87
Hubrig S., Castelli F., de Silva G., González J. F., Momany Y., Netopil M., Moehler S., 2009, "A high-resolution study of isotopic composition and chemical abundances of blue horizontal branch stars in the globular clusters NGC 6397 and NGC 6752" A&A, 499, 865 (arXiv:0903.5182)
Hut P., 1981, "Tidal evolution in close binary systems." A&A, 99, 126
Iben Jr. I., Renzini A., 1983, "Asymptotic giant branch evolution and beyond." ARA&A, 21, 271
Jiang D., 2022, "Binary Evolution and Blue Stragglers in Different Regions of the Color-Magnitude Diagrams of Globular Clusters with Different Ages" ApJ, 940, 97
Jiang D., Chen X., Li L., Han Z., 2017, "Contribution of Primordial Binary Evolution to the Two Blue-straggler Sequences in Globular Cluster M30" ApJ, 849, 100 (arXiv:1709.09643)
Johnson C. I., Pilachowski C. A., 2010, "Chemical Abundances for 855 Giants in the Globular Cluster Omega Centauri (NGC 5139)" ApJ, 722, 1373 (arXiv:1008.2232)
Kaluzny J., Thompson I. B., Krzeminski W., Zloczewski K., 2010, "The Cluster AgeS Experiment (CASE). Variable Stars in the Globular Cluster M55" Acta Astron., 60, 245 (arXiv:1011.0831)
King I. R., 1966, "The structure of star clusters. III. Some simple dynamical models" AJ, 71, 64
Kozai Y., 1962, "Secular perturbations of asteroids with high inclination and eccentricity" AJ, 67, 591
Kraft R. P., 1967, "Studies of Stellar Rotation. V. The Dependence of Rotation on Age among Solar-Type Stars" ApJ, 150, 551
Kraft R. P., 1994, "Abundance Differences among Globular Cluster Giants: Primordial vs. Evolutionary Scenarios" PASP, 106, 553
Kurucz R., 1993, "ATLAS9 Stellar Atmosphere Programs and 2 km/s grid." ATLAS9 Stellar Atmosphere Programs and 2 km/s grid. Kurucz CD-ROM No. 13. Cambridge, 13
Kurucz R. L., 2005, "ATLAS12, SYNTHE, ATLAS9, WIDTH9, et cetera" Memorie della Societa Astronomica Italiana Supplementi, 8, 14
Lanzoni B., Dalessandro E., Ferraro F. R., Mancini C., Beccari G., Rood R. T., Mapelli M., Sigurdsson S., 2007a, "The Blue Straggler Population of the Globular Cluster M5" ApJ, 663, 267 (arXiv:0704.0139)
Lanzoni B., et al., 2007b, "A Panchromatic Study of the Globular Cluster NGC 1904. I. The Blue Straggler Population" ApJ, 663, 1040 (arXiv:0704.1393)
Lanzoni B., Dalessandro E., Perina S., Ferraro F. R., Rood R. T., Sollima A., 2007c, "The Surprising External Upturn of the Blue Straggler Radial Distribution in M55" ApJ, 670, 1065 (arXiv:0709.1609)
Lanzoni B., Ferraro F. R., Alessandrini E., Dalessandro E., Vesperini E., Raso S., 2016, "Refining the Dynamical Clock for Star Clusters" ApJ, 833, L29
Lardo C., Bellazzini M., Pancino E., Carretta E., Bragaglia A., Dalessandro E., 2011, "Mining SDSS in search of multiple populations in globular clusters" A&A, 525, A114 (arXiv:1010.4697)
Lardo C., et al., 2012, "C and N abundances of main sequence and subgiant branch stars in NGC 1851" A&A, 541, A141 (arXiv:1202.6176)
Leigh N., Sills A., Knigge C., 2007, "Where the Blue Stragglers Roam: Searching for a Link between Formation and Environment" ApJ, 661, 210 (arXiv:astro-ph/0702349)
Leiner E. M., Geller A., 2021, "A Census of Blue Stragglers in Gaia DR2 Open Clusters as a Test of Population Synthesis and Mass Transfer Physics" ApJ, 908, 229 (arXiv:2101.11047)
Leiner E., Mathieu R. D., Gosnell N. M., Sills A., 2018, "Observations of Spin-down in Post-mass-transfer Stars and the Possibility for Blue Straggler Gyrochronology" ApJ, 869, L29 (arXiv:1812.02181)
Leiner E., Mathieu R. D., Vanderburg A., Gosnell N. M., Smith J. C., 2019, "Blue Lurkers: Hidden Blue Stragglers on the M67 Main Sequence Identified from Their Kepler/K2 Rotation Periods" ApJ, 881, 47 (arXiv:1904.02169)

Leonard P. J. T., Livio M., 1995, "The Rotational Rates of Blue Stragglers Produced by Physical Stellar Collisions" ApJ, 447, L121

Lidov M. L., 1962, "The evolution of orbits of artificial satellites of planets under the action of gravitational perturbations of external bodies" Planet. Space Sci., 9, 719

Lombardi J. C. J., Rasio F. A., Shapiro S. L., 1995, "On Blue Straggler Formation by Direct Collisions of Main-Sequence Stars" ApJ, 445, L117 (`arXiv:astro-ph/9502106`)

Lovisi L., et al., 2010, "Fast Rotating Blue Stragglers in the Globular Cluster M4" ApJ, 719, L121 (`arXiv:1007.2343`)

Lovisi L., Mucciarelli A., Lanzoni B., Ferraro F. R., Gratton R., Dalessandro E., Contreras Ramos R., 2012, "Chemical and Kinematical Properties of Blue Straggler Stars and Horizontal Branch Stars in NGC 6397" ApJ, 754, 91 (`arXiv:1205.5561`)

Lovisi L., Mucciarelli A., Lanzoni B., Ferraro F. R., Dalessandro E., Monaco L., 2013a, "Flames and XSHOOTER Spectroscopy along the Two Blue Straggler Star Sequences of M30" ApJ, 772, 148 (`arXiv:1306.0839`)

Lovisi L., Mucciarelli A., Dalessandro E., Ferraro F. R., Lanzoni B., 2013b, "Another Brick in Understanding Chemical and Kinematical Properties of BSSs: NGC 6752" ApJ, 778, 64 (`arXiv:1309.5234`)

Lucatello S., Gratton R. G., 2003, "Rotation in Globular Cluster stars. Turn-off and subgiant stars in NGC 104, NGC 6397 and NGC 6752" A&A, 406, 691

Lugger P. M., Cohn H. N., Grindlay J. E., 1995, "CCD Photometry of Globular Cluster Core Structure. II. U-Band Profiles for 15 Candidate Collapsed-Core Clusters" ApJ, 439, 191

Lurie J. C., et al., 2017, "Tidal Synchronization and Differential Rotation of Kepler Eclipsing Binaries" AJ, 154, 250 (`arXiv:1710.07339`)

Mackey A. D., Gilmore G. F., 2003, "Surface brightness profiles and structural parameters for 53 rich stellar clusters in the Large Magellanic Cloud" MNRAS, 338, 85 (`arXiv:astro-ph/0209031`)

Mapelli M., Sigurdsson S., Ferraro F. R., Colpi M., Possenti A., Lanzoni B., 2006, "The radial distribution of blue straggler stars and the nature of their progenitors" MNRAS, 373, 361 (`arXiv:astro-ph/0609220`)

Mapelli M., Ripamonti E., Battaglia G., Tolstoy E., Irwin M. J., Moore B., Sigurdsson S., 2009, "Blue straggler stars in dwarf spheroidal galaxies - II. Sculptor and Fornax" MNRAS, 396, 1771 (`arXiv:0904.0530`)

Marín-Franch A., et al., 2009, "The ACS Survey of Galactic Globular Clusters. VII. Relative Ages" ApJ, 694, 1498 (`arXiv:0812.4541`)

Marino A. F., Villanova S., Milone A. P., Piotto G., Lind K., Geisler D., Stetson P. B., 2011, "Sodium-Oxygen Anticorrelation Among Horizontal Branch Stars in the Globular Cluster M4" ApJ, 730, L16 (`arXiv:1012.4931`)

Marino A. F., et al., 2014, "Helium enhanced stars and multiple populations along the horizontal branch of NGC 2808: direct spectroscopic measurements" MNRAS, 437, 1609 (`arXiv:1310.4527`)

Massari D., et al., 2014, "Ceci N'est Pas a Globular Cluster: The Metallicity Distribution of the Stellar System Terzan 5" ApJ, 795, 22 (`arXiv:1409.1682`)

Mateo M., Bailey J. I., Crane J., Shectman S., Thompson I., Roederer I., Bigelow B., Gunnels S., 2012, in McLean I. S., Ramsay S. K., Takami H., eds, Society of Photo-Optical Instrumentation Engineers (SPIE) Conference Series Vol. 8446, Ground-based and Airborne Instrumentation for Astronomy IV. p. 84464Y, doi:10.1117/12.926448

Mathieu R. D., Geller A. M., 2009, "A binary star fraction of 76 per cent and unusual orbit parameters for the blue stragglers of NGC 188" Nature, 462, 1032

McCrea W. H., 1964, "Extended main-sequence of some stellar clusters" MNRAS, 128, 147

Meibom S., Mathieu R. D., Stassun K. G., 2006, "An Observational Study of Tidal Synchronization in Solar-Type Binary Stars in the Open Clusters M35 and M34" ApJ, 653, 621 (`arXiv:astro-ph/0608154`)

Mészáros S., et al., 2015, "Exploring Anticorrelations and Light Element Variations in Northern Globular Clusters Observed by the APOGEE Survey" AJ, 149, 153 (`arXiv:1501.05127`)

Mészáros S., et al., 2021, "Homogeneous analysis of globular clusters from the APOGEE survey with the BACCHUS code - III. ω Cen" MNRAS, 505, 1645 (`arXiv:2104.12075`)

Meylan G., Heggie D. C., 1997, "Internal dynamics of globular clusters" A&A Rev., 8, 1 (`arXiv:astro-ph/9610076`)

Milliman K. E., Mathieu R. D., Schuler S. C., 2015, "Barium Surface Abundances of Blue Stragglers in the Open Cluster NGC 6819" AJ, 150, 84 (`arXiv:1508.01236`)

Milone A. P., et al., 2015, "The Hubble Space Telescope UV Legacy Survey of Galactic Globular Clusters. III. A Quintuple Stellar Population in NGC 2808" ApJ, 808, 51 (`arXiv:1505.05934`)

Milone A. P., et al., 2017, "The Hubble Space Telescope UV Legacy Survey of Galactic globular clusters - IX. The

Atlas of multiple stellar populations" MNRAS, 464, 3636 (arXiv:1610.00451)
Milone A. P., et al., 2018, "The Hubble Space Telescope UV legacy survey of galactic globular clusters - XVI. The helium abundance of multiple populations" MNRAS, 481, 5098 (arXiv:1809.05006)
Milone A. P., et al., 2019, "The HST Large Programme on NGC 6752 - II. Multiple populations at the bottom of the main sequence probed in NIR" MNRAS, 484, 4046 (arXiv:1901.07230)
Milone A. P., et al., 2023, "Multiple stellar populations in globular clusters with JWST: an NIRCam view of 47 Tucanae" MNRAS, 522, 2429 (arXiv:2301.10889)
Momany Y., Held E. V., Saviane I., Zaggia S., Rizzi L., Gullieuszik M., 2007, "The blue plume population in dwarf spheroidal galaxies. Genuine blue stragglers or young stellar population?" A&A, 468, 973 (arXiv:0704.1430)
Monelli M., et al., 2013, "The SUMO project I. A survey of multiple populations in globular clusters" MNRAS, 431, 2126 (arXiv:1303.5187)
Moretti A., de Angeli F., Piotto G., 2008, "Environmental effects on the globular cluster blue straggler population: a statistical approach" A&A, 483, 183
Mucciarelli A., Lovisi L., Ferraro F. R., Dalessandro E., Lanzoni B., Monaco L., 2014, "Spinning Like a Blue Straggler: The Population of Fast Rotating Blue Straggler Stars in ω Centauri" ApJ, 797, 43 (arXiv:1410.2275)
Nardiello D., Milone A. P., Piotto G., Marino A. F., Bellini A., Cassisi S., 2015, "Observing multiple stellar populations with VLT/FORS2. Main sequence photometry in outer regions of NGC 6752, NGC 6397, and NGC 6121 (M 4)" A&A, 573, A70 (arXiv:1410.7503)
Nardiello D., et al., 2018, "The Hubble Space Telescope UV Legacy Survey of Galactic Globular Clusters - XVII. Public Catalogue Release" MNRAS, 481, 3382 (arXiv:1809.04300)
Nine A. C., Mathieu R. D., Schuler S. C., Milliman K. E., 2024, "WIYN Open Cluster Study. XC. Barium Surface Abundances of Blue Straggler Stars in the Open Clusters NGC 7789 and M67" ApJ, 970, 187 (arXiv:2405.20242)
Packet W., 1981, "On the spin-up of the mass accreting component in a close binary system" A&A, 102, 17
Pandey S., Subramaniam A., Jadhav V. V., 2021, "UOCS - VI. UVIT/AstroSat detection of low-mass white dwarf companions to four more blue stragglers in M67" MNRAS, 507, 2373 (arXiv:2108.03371)
Pasquini L., et al., 2002, "Installation and commissioning of FLAMES, the VLT Multifibre Facility" The Messenger, 110, 1
Perets H. B., Fabrycky D. C., 2009, "On the Triple Origin of Blue Stragglers" ApJ, 697, 1048 (arXiv:0901.4328)
Pietrinferni A., et al., 2021, "Updated BaSTI Stellar Evolution Models and Isochrones. II. α-enhanced Calculations" ApJ, 908, 102 (arXiv:2012.10085)
Piotto G., 2009, in Mamajek E. E., Soderblom D. R., Wyse R. F. G., eds, IAU Symposium Vol. 258, The Ages of Stars. pp 233–244, doi:10.1017/S1743921309031883
Piotto G., et al., 2004, "Relative Frequencies of Blue Stragglers in Galactic Globular Clusters: Constraints for the Formation Mechanisms" ApJ, 604, L109 (arXiv:astro-ph/0402592)
Piotto G., et al., 2007, "A Triple Main Sequence in the Globular Cluster NGC 2808" ApJ, 661, L53 (arXiv:astro-ph/0703767)
Piotto G., et al., 2012, "Hubble Space Telescope Reveals Multiple Sub-giant Branch in Eight Globular Clusters" ApJ, 760, 39 (arXiv:1208.1873)
Piotto G., et al., 2015, "The Hubble Space Telescope UV Legacy Survey of Galactic Globular Clusters. I. Overview of the Project and Detection of Multiple Stellar Populations" AJ, 149, 91 (arXiv:1410.4564)
Preston G. W., Sneden C., 2000, "What Are These Blue Metal-Poor Stars?" AJ, 120, 1014
Rain M. J., Carraro G., Ahumada J. A., Villanova S., Boffin H., Monaco L., Beccari G., 2020, "A Study of the Blue Straggler Population of the Old Open Cluster Collinder 261" AJ, 159, 59 (arXiv:1912.04589)
Rain M. J., Carraro G., Ahumada J. A., Villanova S., Boffin H., Monaco L., 2021a, "The Blue Straggler Population of the Open Clusters Trumpler 5, Trumpler 20, and NGC 2477" AJ, 161, 37 (arXiv:2010.06884)
Rain M. J., Ahumada J. A., Carraro G., 2021b, "A new, Gaia-based, catalogue of blue straggler stars in open clusters" A&A, 650, A67 (arXiv:2103.06004)
Raso S., et al., 2019, "Spectral Energy Distribution of Blue Stragglers in the Core of 47 Tucanae" ApJ, 879, 56 (arXiv:1906.01002)
Recio-Blanco A., Piotto G., Aparicio A., Renzini A., 2002, "Rotation of Hot Horizontal-Branch Stars in the Globular Clusters NGC 1904, NGC 2808, NGC 6093, and NGC 7078" ApJ, 572, L71 (arXiv:astro-ph/0204403)
Reggiani E., Cadelano M., Lanzoni B., Ferraro F. R., Salaris M., Mucciarelli A., 2025, "Detection of a white

dwarf orbiting a Carbon-Oxygen depleted blue straggler in 47 Tucanae" arXiv e-prints, p. arXiv:2508.21118 (arXiv:2508.21118)

Reinoso B., Leigh N. W. C., Barrera-Retamal C. M., Schleicher D., Klessen R. S., Stutz A. M., 2022, "The mean free path approximation and stellar collisions in star clusters: numerical exploration of the analytic rates and the role of perturbations on binary star mergers" MNRAS, 509, 3724 (arXiv:2111.03119)

Ridolfi A., et al., 2022, "TRAPUM discovery of 13 new pulsars in NGC 1851 using MeerKAT" A&A, 664, A27 (arXiv:2203.12302)

Sandage A. R., 1953, "The color-magnitude diagram for the globular cluster M 3." AJ, 58, 61

Sarna M. J., De Greve J. P., 1996, "Chemical Evolution of Algols" QJRAS, 37, 11

Sbordone L., Bonifacio P., Castelli F., Kurucz R. L., 2004, "ATLAS and SYNTHE under Linux" Memorie della Societa Astronomica Italiana Supplementi, 5, 93 (arXiv:astro-ph/0406268)

Shara M. M., Saffer R. A., Livio M., 1997, "The First Direct Measurement of the Mass of a Blue Straggler in the Core of a Globular Cluster: BSS 19 in 47 Tucanae" ApJ, 489, L59

Sills A., Pinsonneault M. H., 2000, "Rotation of Horizontal-Branch Stars in Globular Clusters" ApJ, 540, 489 (arXiv:astro-ph/9911024)

Sills A., Adams T., Davies M. B., 2005, "Blue stragglers as stellar collision products: the angular momentum question" MNRAS, 358, 716 (arXiv:astro-ph/0501142)

Sills A., Karakas A., Lattanzio J., 2009, "Blue Stragglers After the Main Sequence" ApJ, 692, 1411 (arXiv:0811.2974)

Simunovic M., Puzia T. H., 2014, "Blue Straggler Star Populations in Globular Clusters. I. Dynamical Properties of Blue Straggler Stars in NGC 3201, NGC 6218, and ω Centauri" ApJ, 782, 49 (arXiv:1312.2545)

Sollima A., Lanzoni B., Beccari G., Ferraro F. R., Fusi Pecci F., 2008, "The correlation between blue straggler and binary fractions in the core of Galactic globular clusters" A&A, 481, 701 (arXiv:0801.4511)

Spitzer L., 1987, Dynamical evolution of globular clusters

Stetson P. B., Pancino E., Zocchi A., Sanna N., Monelli M., 2019, "Homogeneous photometry - VII. Globular clusters in the Gaia era" MNRAS, 485, 3042 (arXiv:1902.09925)

Tonry J., Davis M., 1979, "A survey of galaxy redshifts. I. Data reduction techniques." AJ, 84, 1511

Vaidya K., Panthi A., Agarwal M., Pandey S., Rao K. K., Jadhav V., Subramaniam A., 2022, "UOCS - VII. Blue straggler populations of open cluster NGC 7789 with UVIT/AstroSat" MNRAS, 511, 2274 (arXiv:2201.08773)

VandenBerg D. A., Brogaard K., Leaman R., Casagrande L., 2013, "The Ages of 55 Globular Clusters as Determined Using an Improved $\hat{V}$HB_TO Method along with Color-Magnitude Diagram Constraints, and Their Implications for Broader Issues" ApJ, 775, 134 (arXiv:1308.2257)

Vasiliev E., Baumgardt H., 2021, "Gaia EDR3 view on galactic globular clusters" MNRAS, 505, 5978 (arXiv:2102.09568)

Vink J. S., Cassisi S., 2002, "Hot horizontal branch stars: Predictions for mass loss. Winds, rotation, and the low gravity problem" A&A, 392, 553 (arXiv:astro-ph/0207037)

Xin Y., Ferraro F. R., Lu P., Deng L., Lanzoni B., Dalessandro E., Beccari G., 2015, "The Binary Mass Transfer Origin of the Red Blue Straggler Sequence in M30" ApJ, 801, 67 (arXiv:1501.01358)

Yong D., Grundahl F., Johnson J. A., Asplund M., 2008, "Nitrogen Abundances in Giant Stars of the Globular Cluster NGC 6752" ApJ, 684, 1159 (arXiv:0806.0187)

de Mink S. E., Langer N., Izzard R. G., Sana H., de Koter A., 2013, "The Rotation Rates of Massive Stars: The Role of Binary Interaction through Tides, Mass Transfer, and Mergers" ApJ, 764, 166 (arXiv:1211.3742)

van Saders J. L., Pinsonneault M. H., 2013, "Fast Star, Slow Star; Old Star, Young Star: Subgiant Rotation as a Population and Stellar Physics Diagnostic" ApJ, 776, 67 (arXiv:1306.3701)